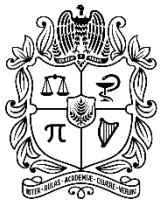

UNIVERSIDAD
NACIONAL
DE COLOMBIA

MODELO COMPUTACIONAL DE REMODELAMIENTO ÓSEO MEDIANTE ESTRUCTURAS DISCRETAS

Diego Alfredo Quexada Rodríguez

Universidad Nacional de Colombia

School of Medicine

Bogotá, D.C, Colombia

2021

Computational model of bone remodeling using discrete structures

Diego Alfredo Quexada Rodríguez

Research work presented as partial requirement for the degree of:

Master in Biomedical Engineering

Advisor: Diego Alexander Garzón Alvarado, Ph.D.

Co-advisor: Kalenia María Marquez, Ph.D.

Department of Mechanical Engineering and Mechatronics

Research line: Computational Mechanics

Research group: Mathematical Modelling and Numerical Methods (GNUM)

Universidad Nacional de Colombia

School of Medicine

Bogotá, D.C, Colombia

2021

Para Fanny Leonor Rodríguez y Alfredo Quexada

“Nunca me he sentido bueno, pero sí me he dado cuenta de que muchas veces, gracias a la benéfica influencia de -mi mamá- y papá, he podido ser un malo que no ejerce, un cobarde que se sobrepone con esfuerzo a su cobardía y un avaro que domina su avaricia.”

Héctor Abad Faciolince

Agradecimientos

Todo lo positivo que he logrado hasta el momento, ha sido en gran parte gracias a las enseñanzas, los consejos y el apoyo de amigos, familiares y también de aquellos en quienes he identificado algunas virtudes o me han mostrado el por qué las virtudes son importantes, ya sea por ejemplo o contraejemplo.

Agradezco al profesor Diego Alexander Garzón por su paciencia en sus explicaciones, por su amable disponibilidad para dirigir esta labor y especialmente por creer en mi trabajo. A Kalenia María Márquez, quien asesoró este trabajo, por sus gratas asesorías y charlas que me han motivado a ser cuidadoso en el detalle. Al profesor Ernesto Córdoba quien me enseñó mediante el ejemplo, la importancia de la ética del trabajo y a enfrentar con estoicismo el diario vivir. A mis compañeros y amigos de maestría quienes han hecho esta experiencia más amena. En mi familia, a mi mamá Fanny Leonor Rodríguez, a mi papá, Alfredo Quexada, a quienes espero retribuir todo lo que han hecho, porque todo lo positivo en mi empezó con ustedes.

Finalmente, agradezco a la Universidad Nacional de Colombia por acogerme en sus aulas un tiempo más durante esta maestría y por brindarme tantas experiencias, esenciales para mi formación.

Abstract

In-silico models applied to bone remodeling are widely used to investigate bone mechanics, bone diseases, bone-implant interactions, and also the effect of treatments in bone pathologies. This work proposes a new methodology to solve the bone remodeling problem using one-dimensional (1D) elements to discretize trabecular structures more efficiently. First a concept review on the bone remodelling process and mathematical approaches, such as homogenization for its modelling are revised along with famous previous works on this field, later, in chapter two, the discrete modelling approach is validated by comparing FE simulations with experimental results for a cellular like material created using additive manufacturing and following a tessellation algorithm, and later, applying an optimization scheme based on maximum stiffness for a given porosity. In chapter three, an Euler integration scheme for a bone remodelling problem is coupled with the momentum equations to obtain the evolution of material density at each step. For the simulations, the equations were solved by using the finite element method and a direct formulation, and two benchmark tests were solved varying mesh parameters in two dimensions, an additional three-dimensional benchmark was addressed with the same methodology. Proximal femur and calcaneus bone were selected as study cases given the vast research available on the topology of these bones, and compared with the anatomical features of trabecular bone reported in the literature, the study cases were examined mainly in two dimensions, but the main trabecular groups for the femur were also obtained in three dimensions. The presented methodology has proven to be efficient in optimizing topologies of lattice structures; It can predict the trend in formation patterns of the main trabecular groups from two different cancellous bones (femur and calcaneus) using domains set up by discrete elements as a starting point. Preliminary results confirm that the proposed approach is suitable and useful in bone remodeling problems in 2D and 3D leading to a considerable computational cost reduction. Characteristics similar to those encountered in topological optimization algorithms were identified in the benchmark tests as well, showing the viability of the proposed approach in other applications such as bio-inspired design. Finally, in the last part of this work, the discrete approach developed in chapter two and three is coupled with two classic bone remodelling models, forming a new model that takes into account a variety of biological

parameters such as paracrine and autocrine regulators and is able to predict different periodical responses in the bone remodelling process within a 2D domain with mechanical field variables.

Keywords: bone remodeling, trabecular bone, finite element analysis, bone architecture, topological optimization.

Content

Figure list

Table List

Symbol and abbreviations list

Symbol	Meaning
A	Area
B	Body forces
E	Elastic modulus
K	Evolution constant
L	Length of the element
I	Moment of inertia
M_i	Moment at node i
P_i	Longitudinal load at node
T	Twisting moment
U	Strain energy
u	Longitudinal displacement
v	Transversal displacement

Symbols with Greek letters

λ	Dimensionless density
σ	Stress
Y	Poisson coefficient

Subscripts

i	I-th Element
left	Referring to left node
right	Referring to right node

Abbreviations

Abbreviation	Meaning
TO	Topological optimization
BEM	Boundary element method
BMU	Basic multicellular unit
BMD	Bone mass density
FEM	Finite element method
GTM	Greater trochanter group (Spanish)
GSC	Secondary compressive group (Spanish)
GST	Secondary tensile group (Spanish)
GPT	Principal tensile group (Spanish)
GPC	Principal compression group (Spanish)

Introduction

In recent years, biology has gain importance for engineering as a source of inspiration for developments such as robot design, bio- inspired computation, structures, actuators, material design, and more (Braun, Manoonpong, and Xiong, n.d.). This search for inspiration had an early beginning when the anatomist G.H von Meyer made a publication in 1867 where he presented drawings of cancellous or "spongy" bone in the proximal femur (Meyer 1867); An acquittance of von Meyer, a swiss structural engineer named C. Culmann noted these patterns, and realized the similarities between one of his designs for a crane and the topology of the femur (Cowin 1986), but it was Wolff in 1872 the one that first published a paper where he stated that the main trabecular groups tend to align to the principal stress trajectories in the femur, this last statement laid the basics to study bone remodelling from a mechanical point of view and established a new field where engineers and medical doctors could teamwork in specific fields such as prosthesis design, pharmaceutical treatments, among others.

This collaboration between engineering and medicine to study bone remodelling has its main motivation in the research required to treat many diseases or conditions that affect bone remodelling. Osteoporosis, a disease found to affect bone mass density (BMD) has a prevalence estimated in 158 million advanced (high risk of osteoporotic facture) cases worldwide, and this prediction has been said to double by 2040 (Ström et al. 2011), this disease alone had a financial burden of $4.6 billion in 2016 in Canada (Hopkins et al. 2016). Another metabolic bone disease with a high incidence is osteopetrosis which is linked with a positive net bone turnover (increased BMD), which is a rare inherited condition with 1 in 20,000 to 250,000 depending on which type (Owen and Reilly 2018). There are other diseases such as Paget's disease or renal osteodystrophy that have an important prevalence and are investigated in the field of bone remodelling (Feng and McDonald 2011).

To address the need of research in this field , various collaborations have been made between medical professionals, engineers, physicists, mathematicians and other disciplines that try to contribute at the understanding on how the bone remodelling occurs and in helping prevent and treat imbalances in this process (Wippert et al. 2017), as a result of this collaboration in different disciplines, new fields such as mechanobiology have emerged and one of the main tools adopted

has been mathematical modelling. This approach in bone remodelling, provides a quantitative tool that helps in the understanding of existing correlations between a stimulus and biological variables such as strain energy and turnover rate (Raggatt and Partridge 2010).

There are various classical works on bone remodelling that use mathematical modelling as a research tool, for example (Weinans, Huiskes, and Grootenboer 1992) made a model that uses the finite element method (FEM) to calculate mechanical field variables such as energy strain and principal stresses and considers them as stimulus to the bone remodelling process, this model is able to predict the main trabecular groups in accordance to different loading conditions, such as normal gait and prosthesis implantation. There are more models that follow the same approach but use different type of stimulus, such as interstitial flows, strain energy densities, temperatures among others (Della Corte, Giorgio, and Scerrato 2020). Some important models will be briefly reviewed in the bibliographical revision. These models have been useful to study the dynamic in which a mechanical stimulus affects the remodelling process and evaluating its results in a spatial domain. There are other types of mathematical models that focus more on the dynamics of cell populations involved in the bone remodelling process, Komarova et al. 2003 proposes a set of differential equations that estimates the dynamic population of the principal cells and the bone mass density in a bone remodelling unit (BMU). This model takes into account the influence from different regulators that inhibit the cells proliferation in charge of bone formation and resorption, which is useful in the pharmaceutical treatment of bone disorders.

This work builds a new modelling methodology, based on discrete modelling using the Finite Element Method (FEM) by applying a direct formulation which is computationally faster than using variational methods or weighted residuals. These discrete elements correspond to Truss and Frame elements (Details on this formulation on the annexes). The main goal of this study is to provide a novel methodology to address the bone remodelling problem that may be used by bone remodelling researchers to gain insight on mechanical and biological aspects on this process. Furthermore, engineers working in the field of cellular materials, computational mechanics, and bio-inspired design can use some of the results in topology given by some of the algorithms presented as conceptual designs, especially those shown in chapter two relating tessellations and chapter three regarding structures with a topology created with a bone remodelling algorithm.

This thesis is divided into seven chapters where discrete based modelling will be explored as a tool to solve problems mainly regarding bone remodelling, but other applications will be addressed too, such as usefulness in additive manufacturing and mechanical analysis. First chapter will give a conceptual background where some of the main bibliographical sources will be presented. Second chapter will introduce the concept of discrete based modelling for an additive manufacturing study case, where different tessellations will be modelled and results will be compared experimentally. Third chapter uses the discrete based approach to solve a bone remodelling problem, where first its use will be validated on various classical benchmarks in bone remodelling and topological optimization problems, then a medical study case will be examined as a potential application of this approach, this implementation will be applied to 2D and 3D domains. In fourth chapter a new model that couples two classical bone remodelling models will be implemented using discrete based modelling as well, where the bone remodelling dynamics will be linked to the mechanical behavior in the domain. Finally, in chapter five general conclusions, future work and final remarks will be addressed. Finally, chapter six and seven correspond to references and annexes, respectively.

Objectives

- **General objective**

To build a discrete mathematical model that integrates mechanical field variables and cellular mechanics in the bone remodelling process

- **Specific objectives**

-To build a zero-dimensional bone remodeling model that takes into account the processes of cell biology.

-To propose a discrete domain finite element formulation with the constitutive equations that model the bone remodelling process, both biological and mechanical, and whose solution provides important information to establish optimal parameters.

-Validate the model with available experimental measurements on bone remodeling in trabecular bone.

1. Conceptual background

1.1. Bone biology

Bone is a connective tissue made up of cells embedded in a matrix that has a component of organic material containing type I collagen, lipids, proteoglycans, cytokines, and growth factors among other proteins, this amounts to the 40% of the matrix composition. The remaining 60% composition of inorganic material includes calcium hydroxyapatite and octacalcium phosphate (Gasser and Kneissel 2017). There can be found four cell types in bone: Cartilage-forming chondrocytes, bone-forming osteoblasts, bone-resorbing osteoclasts, and mechanotransduction regulatory osteocytes (Kenkre and Bassett 2018). The action of these cells along with the cellular matrix ensures the functioning of the skeletal system. In addition to the structural function of the skeleton and facilitator of locomotion, it also plays the role of main mineral reservoir, which is important to level pH in other organs and achieve homeostasis (Kenkre and Bassett 2018).

Bone can be classified as cortical or compact bone and trabecular or cancellous bone, the former has an increased density in comparison with the trabecular bone (between 5% and 10%), and it can be found mainly on the periphery of trabecular bone and on the shaft of long bones. It has been stated that over 80% of the total skeletal mass corresponds to cortical bone (Cowin, and Telega, 2003). The cancellous bone or trabecular, meaning “small beam” from Latin *trabēcula,* is made up of a rod or beam like random structure with plates, where there can be found trabecular groups organized accordingly to the stresses to which bone is subjected to, this is known as Wolff’s law, named after the anatomist and surgeon Julius Wolff who, in 1892, who first theorized the adaptations that bone undergoes concerning mechanical loads (Cowin 1986) .

1.2. Modelling

This process begins in the early skeletal formation and involves growth and shape change in bone. The net formation of bone is positive, whereas in bone remodelling there is an equilibrium between formation and resorption, and not net change in bone mass is appreciated, modelling occurs mainly on the uncomplete formed bone. This requires the uncoupling between formation and resorption of bone. An important example of bone modelling occurs in the radial growth of

the diaphysis in long bones as well as in linear growth e.g the metaphysis below the growth plate where there is osteoclastic resorption in bone surface and new formation on the endosteal surface (Seeman 2003).

1.3. Bone remodelling

The bone remodelling process is made up of a series of coupled dynamic interactions between various cell types and regulators such as signaling pathways and other factors that respond to different mechanical and biological conditions. The processes of bone formation and resorption are coupled to assure that there is no net loss of bone. The remodelling cycle takes place within the basic Multicellular Unit (BMU), and is divided into five different stages: activation, resorption, reversal, formation, and termination phase. Bone remodelling asynchronously occurs throughout the skeleton. The ultimate goal of bone remodelling is to repair the occurring damage in bone microstructure and maintain homeostasis of the necessary minerals. Fig. 1 shows in a comical manner the bone remodelling process, where the osteocytes are depicted as the orchestrators, allowing osteoclast and osteoblasts passage into the BMU to perform either resorption or formation, and the dendritic process from the osteocytes are shown.

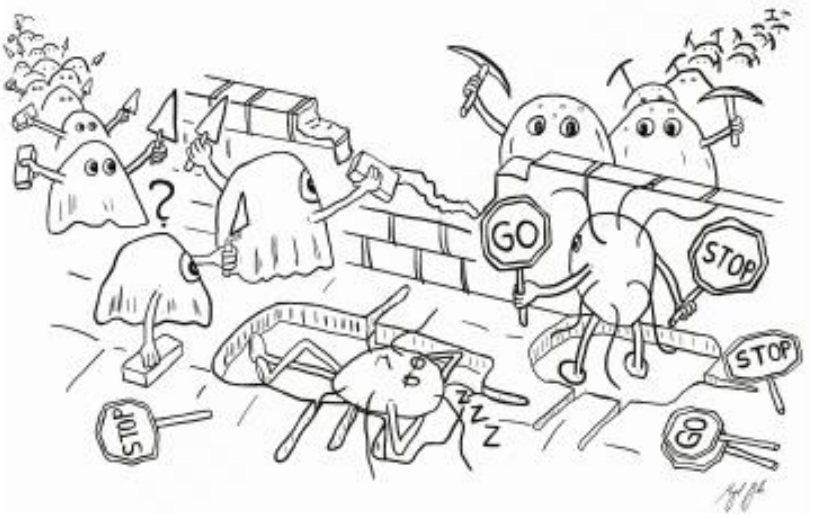

Fig. 1: Bone remodelling cartoon.
Cartoon of the bone remodelling process, adapted from (Bahia et al. 2020). Art: Miguel T. Bahia

1.3.1. Activation

In this stage osteoclast precursor cells from the marrow (hematopoietic cells) are recruited to the bone surface where lining cells have separated from the outer part of the bone and begin to form Howship's lacunae in trabecular bone or cutting cones as in cortical bone; in this zone, the BMU will undergo the bone remodelling process. The first signal that sets into motion the bone remodelling dynamic is originated in the dendritic processes from osteocytes that make up the mechanosensory system and is generated given a mechanical stimulus, this could be a certain strain energy density that results in structural microdamage in bone's architecture (Bullock, Pavalko, and Robling 2019). Another initiator may be a hormonal change due to a systemic adaptation to preserve homeostasis.

A direct consequence of damage to the bone matrix or limb immobilization is osteocyte apoptosis and an increase in osteoclasts formation (Raggatt and Partridge 2010). This occurs because osteocytes secrete transforming growth factor β (TGF- β) which inhibits osteoclast formation, so a negative correlation exists between the population of osteocytes and osteoclasts.

The main hormone in charge of the regulation of bone homeostasis is the calciotropic parathyroid hormone (PTH), secreted by parathyroid glands as a response to a decrease in serum calcium. PTH acts directly on kidneys and bone, and indirectly on the intestine. The binding of PTH to its receptors activates protein Kinases which make part of signaling pathways that induce transcriptional responses that regulate the secretion of molecules that recruit osteoclast precursors (Swarthout et al. 2002).

1.3.2. Resorption

In this phase that is approximately two weeks in duration, in humans, osteoblasts are activated similarly as in activation phase by osteocytes or by an endocrine or paracrine signal. When PTH induced remodelling occurs, osteoblast produces the chemoattractant MCP-1 (monocyte chemoattractant protein-1), a chemokine for osteoclast precursors. This also enhances the formation of osteoclasts due to the action of the receptor activator for nuclear factor k β (RankL).

In this phase a "sealed zone" is created by matrix metalloproteinases (MMPs) secreted by osteoblasts, these MMPS degrade the portion of the osteoid that lines the bone surface. Inside

this sealed zone, also known as Howship lacunae, Hydrogen ions are pumped, causing the dissolution of the mineralized matrix. The remaining organic portion of the bone matrix is degraded by collagenolytic enzymes (Okaji et al. 2003).

1.3.3. Reversal

After osteoclast resorption, a specific lineage of osteoblasts, osteomacs, remove the remaining demineralized collagen matrix of howships lacunae. Also, the reversal cells receive and produce coupling signals that finally give way to the formation stage within the BMU. After the organic material has been removed a cement-line composed of a non-collagenous mineralized matrix to increase adhesion in the next phase for osteoblastic cells. This phase has a duration of approximately four or five weeks in humans.

1.3.4. Formation

It has been stated that the EphB4 ephrin B2 signaling complex is responsible for bone formation activation and the inhibition of bone resorption (Raggatt and Partridge 2010). The osteocytes (the orchestrators) act as a mechanosensory system, in resting condition, they express sclerostin which binds to LRP5 (low-density lipoprotein receptor-related protein-5/6) and acts as a negative inhibitor of Wnt signaling, which is an inducer of bone formation (X. Li et al. 2005). When there is a mechanical strain on bone or PTH signaling takes place, the expression of sclerosing decreases allowing Wnt signaling to occur, conducing to bone formation (Raggatt and Partridge 2010).

The secreted substances by osteoblast that conform bone consist of collagen type I which is the main organic constituent of bone. Other proteins such as proteoglycans, glycosylated, small integrin-binding ligand proteins (SIBLING) conform to the non-collagenous proteins. This entire process takes about four months in duration. (Eriksen et al. 1984)

1.3.5. Termination phase

The bone remodelling cycle ends when the portion of bone resorbed has been rebuild. This occurs due to the gain of sclerostin expression after osteoblastic bone formation has begun. Next, osteoblasts can suffer different fates, e.g. revert to a bone lining phenotype, differentiate into osteocytes when they have been entombed in the new bone matrix, or undergo apoptosis.

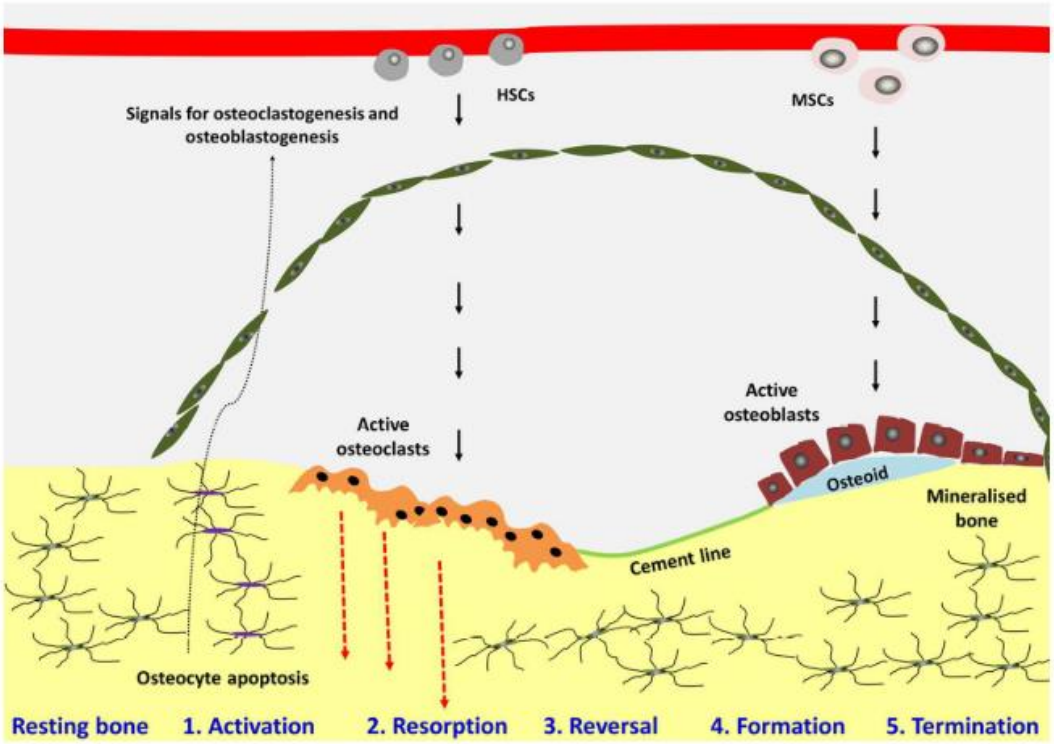

Fig. 2: Bone remodelling cycle, adapted from Kenkre and Bassett 2018

1.4. Regulation in bone remodelling

1.4.1. -Endocrine regulation

Endocrine regulation refers to that which occurs as part of the hormonal system, where there are various regulator agents of the bone remodelling process, such as the PTH, vitamin D, calcitonin, thyroid hormone, growth hormone, among others. These agents have as target cells the ones involved in bone formation and absorption, and produce a response not in the vicinity from the regulator was originated. The PTH has an effect on bone remodelling depending on the duration of exposure. It has been found that excess exposure to PTH in the BMU results in a net loss of bone during the remodelling cycle, this is common in hyperparathyroidism, this loss in bone density affects specially cortical bone (Stein et al. 2013). In case of osteoporosis an intermittent dosage of PTH is used as an anabolic agent.

Vitamin D is an important agent that is in charge of the phosphate and calcium absorption in the intestines which provides the necessary substrates for mineralization. It also affects skeletal cells

directly by binding to vitamin D receptors and the deletion of these receptors in osteoblast results in an increase of trabecular bone (Yamamoto et al. 2013). Another important agent is Calcitonin, which is a peptide hormone found to inhibit bone resorption and that decreases osteoclast population.

Growth hormone induces the expression of Insulin-like growth factor that results in an increased rate of bone formation and resorption, in its absence, bone resorption period takes longer in the bone remodelling cycle resulting in osteoporosis. The deficiency of Thyroid hormone lowers the turnover rate, resulting in an increased bone mass (Kenkre and Bassett 2018).

1.4.2. -Paracrine regulation

This kind of regulation occurs by the action of a molecule that targets the same type of tissue where is produced, therefore, acts in its vicinity. TGF- β as it has been stated before has an important role in signaling pathways inducing expression of the master osteoblast transcription. Prostaglandins are lipids that act amid G-protein (protein family that acts as signal transductor) receptors and regulate bone formation and resorption. Another important group of paracrine regulators are cytokines that can stimulate osteoclastogenesis. In menopause, these cytokines play an important role in the development of osteoporosis as their imbalance is associated with a decoupling between resorption and formation.

1.5. Imbalances in the bone remodelling process

Any affection in the balance between formation and resorption that occurs in bone remodelling is considered a metabolic bone disease, in Fig. 3 an overview with the main imbalances is shown with its primary cause and prevalence.

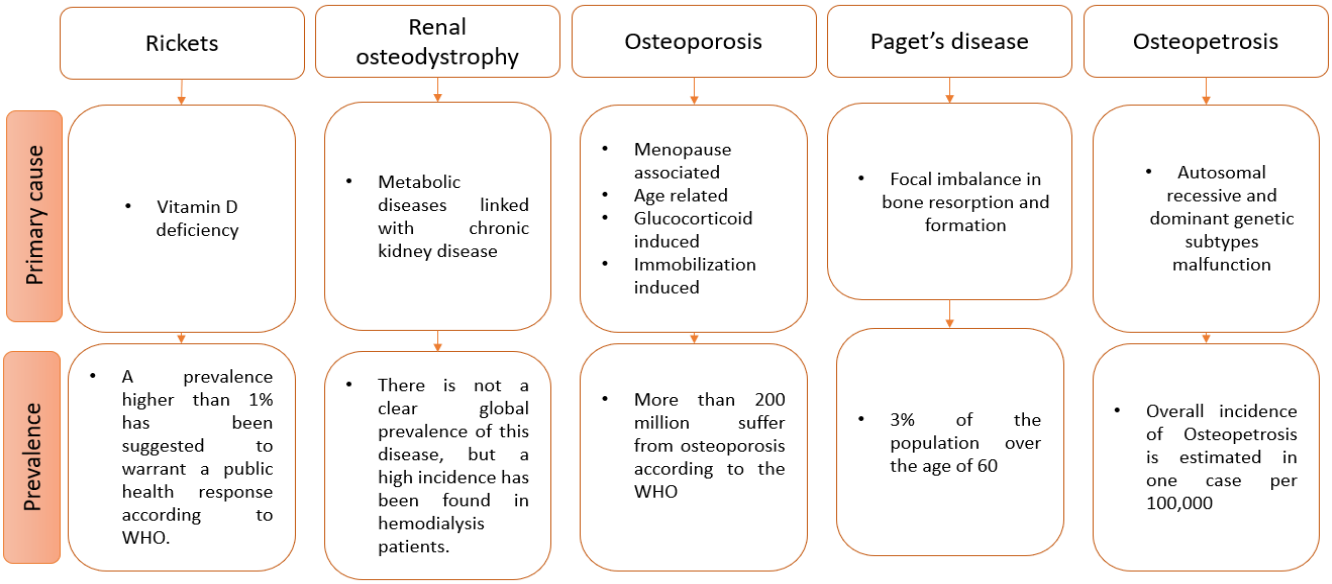

Fig. 3 Bone remodelling disorders overview.

1.6. Mathematical models

Numerous studies on bone remodelling have been made over the last decades. The principal focus in the first works was experimentation in vitro or in vivo to analyze bone biology, nonetheless, computer tools have gained great importance to model biological phenomena. One type of approach observed in bone mathematical modelling literature is to investigate cell population models that relate to formation and resorption in the BMU. Also, we can find models that use a mechanical stimulus as the main cause of bone remodelling, this stimulus can vary among different field variables such as strain energy density, hydrostatic pressure, temperature, interstitial flow, just to mention a few. Finally, multiphysical models that try to couple different approaches that may give insights on biological phenomenon e.g., analyzing osteoblast cell population given a mechanical stimulus, predicting bone formation patterns after changes in load condition. The main advantage of the employment of these mathematical models is that they provide quantitative data to help in the understanding of the existing correlations between different variables such as resorption and formation rate (Raggatt and Partridge 2010), which would be difficult to find with other kinds of experimentation, in Fig. 4(a) a schematic is shown on how bone remodelling literature is divided.

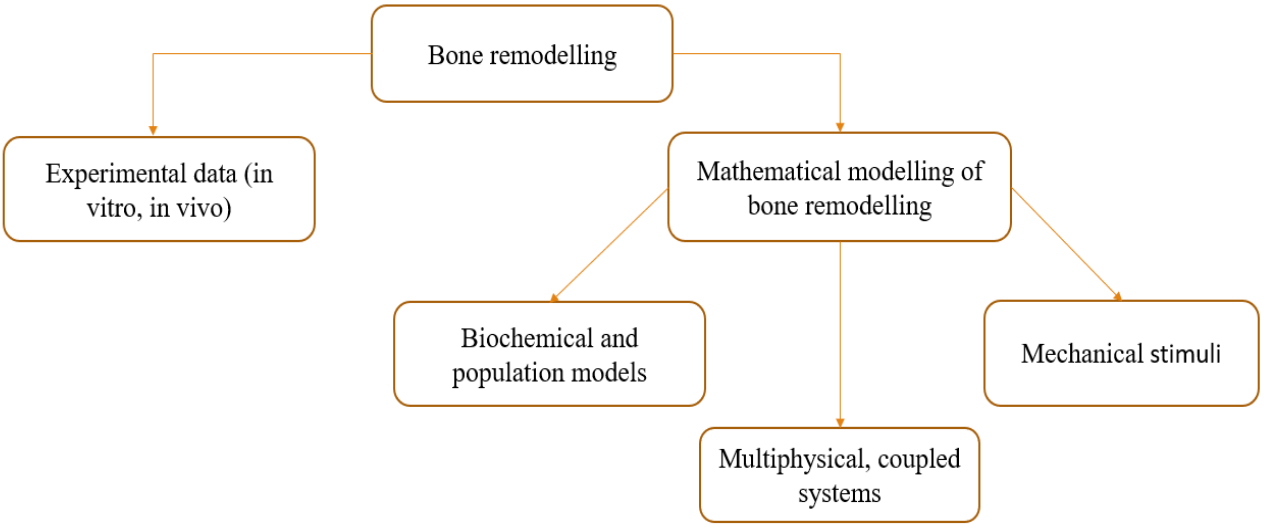

Fig. 4: Literature distribution on Bone remodelling

Cell population models have been used extensively to find how signaling pathways, regulators, and pharmaceuticals influence the dynamic process of bone remodelling. Among the classical works on bone cell population models, the one by (Komarova et al. 2003) features the influence of paracrine and autocrine regulators such as TGF- β in the dynamic behavior of osteoblast and osteoclast populations utilizing nonlinear differential equations, that also describes the bone mass in the BMU. This model can predict different types of response that correspond to normal bone remodelling function and different clinical cases such as Paget's disease and osteoporosis, in Fig. 5 the dynamical behavior is described accounting for the population of osteoblasts and osteoclasts in the normal bone remodelling cycle. Another cell population model considered to be classical is that of (Pivonka et al. 2008), this model proposes a set of differential equations that describe the dynamic behavior of bone cells, depending on the influence of the signaling pathway RANK-RANKL-OPG with the addition of TGF- β. These two last models have become a classic in the field of bone remodelling and are widely known for its robustness.

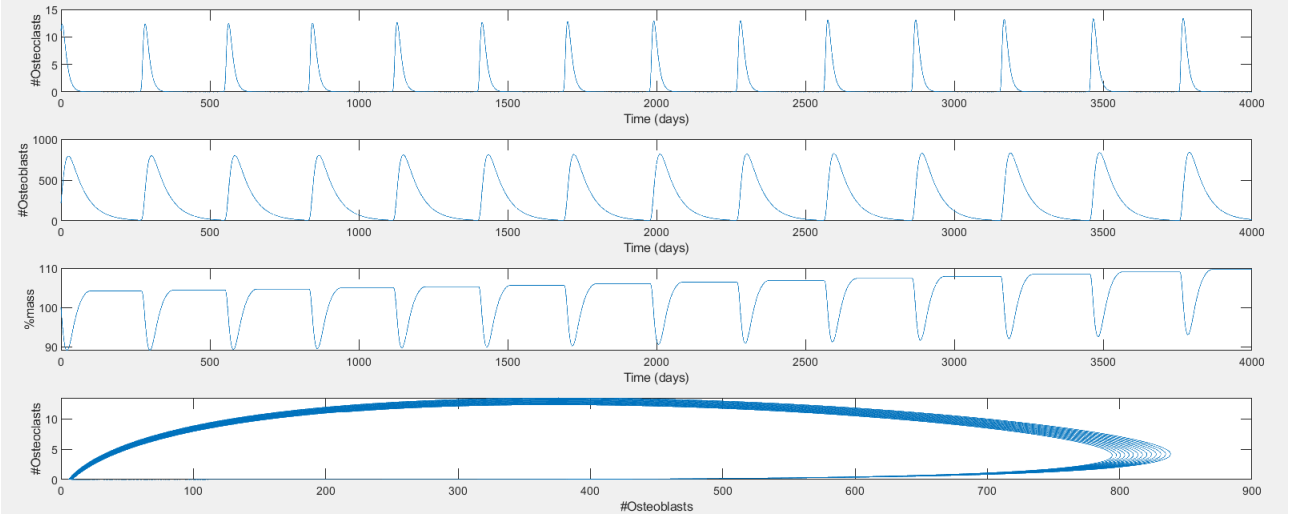

Fig. 5: Population dynamics for a normal remodelling cycle.

As stated above, other type of models calculate mechanical field variables that correlate to bone formation and resorption. The first model to use a mechanical stimulus and relate it in a quantitatively manner to bone remodelling was that of Wolff in 1892 (Cowin 1986). Among the classical works, (Nackenhorst 1997) proposed a model that uses the strain energy density as the mechanical stimuli to trigger bone remodelling, in this model, a bone density equation (Eq.1) depends of the energy strain at a given time step and a few constants that are found experimentally, in this case U_{ref} is the strain energy threshold at which remodelling occurs, and k is an experimental constant. It is worth noting that in each step the elastic modulus from each element changes accordingly to its strain energy density, conforming to an iterative process.

$$\frac{d\rho}{dt} = k\left(\frac{U_\rho}{U_{ref}} - 1\right) \qquad \text{Eq. 1}$$

Nackenhorst model can predict the main trabecular groups in the epiphysis, and this information is used to give insights on bone remodelling after a prosthesis has been implanted, and based on these insights, recommendations for improved prosthesis design and surgery are given (Nackenhorst 1997).

Weinans, Huiskes, and Grootenboer 1992 proposed a similar model that uses a bone density equation (2) that follows an objective function which achieves a preset energy strain density in the domain, here, B is the remodelling constant, and k the reference value that sets the threshold

at which remodelling occurs. This model is able to predict as well the trabecular groups and is tested in a plate model which has become a classical benchmark test where discontinuities are found, similar in topology to trabecular bone.

$$\frac{d\rho}{dt} = B\left(\frac{U_\rho}{\rho} - k\right) \qquad \text{Eq. 2}$$

In the last two decades, there have been authors that according to experimental observations on bone tissue have modeled the main mechanical stimulus as an interstitial flow in the mechanosensory system formed by osteocytes. (Kumar, Jasiuk, and Dantzig 2011) models a poroelastic flow using a Biot model where a Darcy dissipation triggers bone remodelling, also with the addition of the Willis and Skempton coefficients that relate to change in volume under drained conditions.

$$\left.\begin{array}{c} \Sigma_{ij} = 2\mu\varepsilon_{ij} + \delta_{ij}(\lambda tr(\varepsilon) - \alpha M\zeta) \\ p = -\alpha M tr(\varepsilon) + M\zeta \\ \dot{w} = -\frac{k}{\eta}\nabla p \end{array}\right\} \qquad \text{Eq. 3}$$

Here, Σ is the stress of the solid matrix, ε_{ij} the strain tensor, p the por pressure and $\lambda, k, \mu, \alpha, \eta, and\ M$ are coefficients.

The last advances in mathematical bone remodelling have had a more holistic approach, trying to model biological phenomenon using different variables, such as cell population and mechanical stimulus and its interaction at different scales and looking at the different interconnected phenomenon. (Rapisarda et al. 2019) proposes a set of differential equations to relate osteoblast, osteoclast, osteocyte population to a mechanical stimulus such as a function of porous flow.

$$\left.\begin{array}{c} \dot{x_b} = -\beta_b X_b - \gamma_{bk} x_b \mathrm{K}(\phi) + S\alpha_b x_k \\ \dot{x_k} = -\beta_k X_k - \gamma_{bk} x_b \mathrm{K}(\phi) \\ \dot{x_c} = -\beta_c X_c - \gamma_c x_c \mathrm{K}(\phi) + S\alpha_c x_c \\ \dot{\rho} = (a x_b - b x_c)\mathrm{H}(\phi) \end{array}\right\} \qquad \text{Eq. 4}$$

Here x_b, x_c, x_k are the change in population rate of osteoblasts, osteoclast, and osteocytes. $\dot{\rho}$ is the change in bone mass. H and k are functions of the porous flow. S is taken as a stimulus function. Finally, a, b, β_b, $\beta_k$and β_c are biological parameters.

According to the recent review of (Della Corte, Giorgio, and Scerrato 2020) on mathematical models in bone remodelling, the main advances in this field will be related to concepts such as damage theory and factor signaling in bone biology (Bullock, Pavalko, and Robling 2019). Once an experimental observation (in vivo or in vitro) has been stated, it is possible to model this observation and see how their variables are interconnected by means of an in-silico model, this could complement in-vivo and in-vitro experimentation and reduce the number of trials which require resourses.

1.7. Discrete based Modelling in FEA

The behavior of a cellular structure on a macroscopical scale is governed by the dynamics that occur at the microscopic scale, a process used to study this type of materials is that of homogenization, which consists in modelling the macro properties of a material using as a base the dynamics occurring at a microscopic scale. This process is also used to simplify the analysis by decreasing the degrees of freedom (DOFS) in the mechanical model to be analyzed with FEM (Daxner 2010). In the field of bone mechanics, the homogenization technique has been used before to analyze failure properties of trabecular bone which is of interest in the understanding of bone-implant interface mechanics, see for example (Ganghoffer and Goda 2018).

In additive manufacturing discretizing the infill of a part can be achieved using different tessellation algorithms, in the next chapter a few geometries obtained by different techniques are analyzed using a discrete approach, which may be useful to analyze parts as the one seen in Fig. 6.

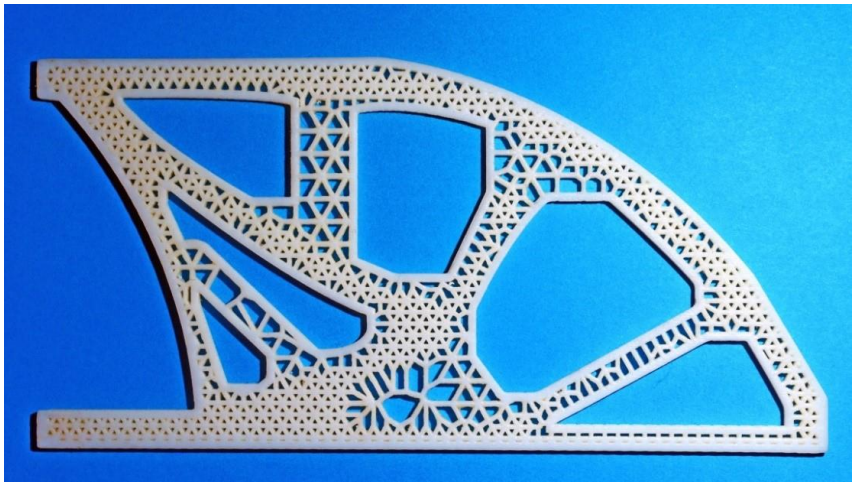

Fig. 6 Equilateral triangular tessellation

Tessellation applied to a topological optimized geometry for additive manufacturing, credits to (Fahir et al. 2020) and GNUM group, Universidad Nacional de Colombia.

When planning the design of cellular materials, there are different approaches to choose the most suitable unit cell depending on the requirements, a classical approach was developed by Clark Maxwell, who in 1864 published a paper proposing a simple equation (see Eqn. 5) that gives insight on the behavior of a unit cell, depending on the number of struts, *b*, and joints, *j*,(Maxwell, n.d.). Different configurations are shown in Fig. 7, the observations about the overall behavior of the structure are based on the topology of the unit cell, this is an important fact in the homogenization technique, and is useful to avoid the costly computational task of analyzing the full lattice geometry, and instead, focus on a single unit. Nonetheless, most recent designs of cellular materials use FEA to analyze more complex lattice structures in 2D and 3D, to further in the recent advances in lattice unit topology see (Chen, Zheng, and Liu 2018) and (Bhate et al. 2019).

$$M = b - 2j + 3 \qquad \text{(Eq. 5)}$$

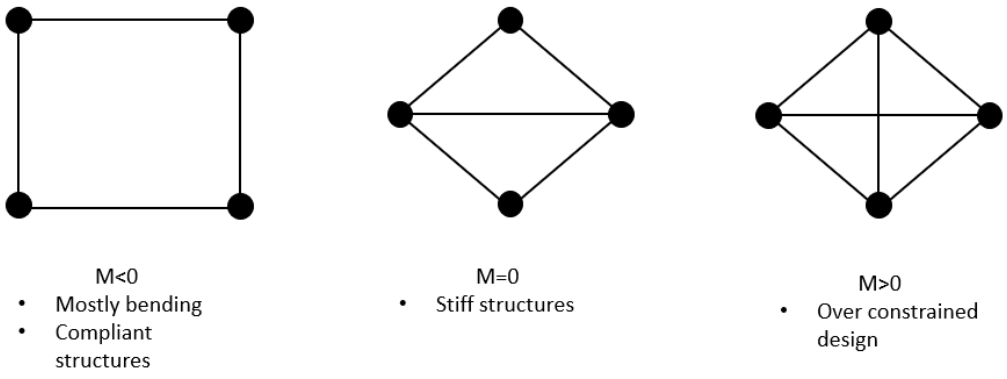

Fig. 7 Maxwell, stability criterion for different structures

There are many possibilities to discretize a domain and solve a problem with the finite element method, the use of the type of element may vary on the problem and computational resources available. In 2D simulations, the use of quadrilateral and triangular elements is widely used, depending on the desired accuracy in results these could be linear, quadratic, or higher-order elements. When homogenization is applied, other types of elements are used, such as 1D beams or surface elements. The models whose domain is composed of beam elements are often said to have a lattice structure, in this configuration of material, some design variables could be: length, cross-sectional shape or topology unit cell (Bhate et al. 2019). Surfaces such as shell finite elements are an alternative to beams in the formation of the unit cell lattice, in nature, some topologies are found to be “minimal surfaces” so shell elements are a good option to represent them in the sense that they can easily fit the mathematical requirements in shape to accomplish this energetically favorable topology (Bhate et al. 2019). A more detailed focus on cellular materials will be shown in chapter 2.

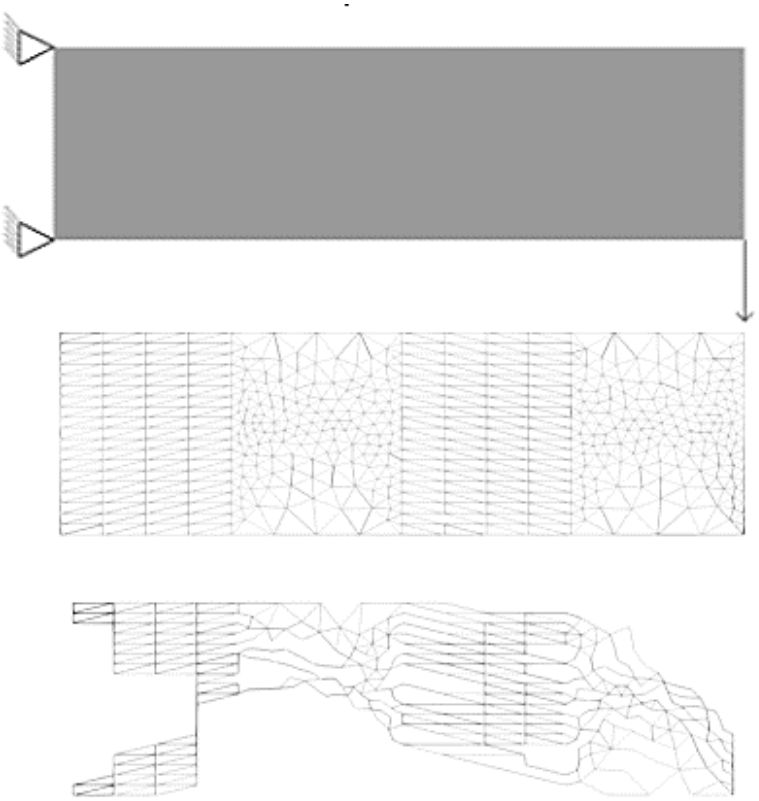

Fig. 8: Homogenization example
Results in topology of a bone remodelling algorithm using homogenization with a mesh composed by structured and unstructured sections.

In Fig. 8 a study case is shown where discretization is applied to a cantilever beam (top figure), and in the resulting discretized domain is applied a bone remodelling scheme that optimizes its topology. The lattice structure can be modeled by using truss or frame finite elements (see annexes to see mathematical formulation). This modelling technique has the advantage to reduce the computational cost, (Bhate et al. 2019) demonstrated that compared with a continuum-based solution (hexahedron elements), the beam-FE model achieved a 500-fold computational speed and a 250-fold memory gain. In addition, as will be seen in chapter 3, a comparison between the continuum approach and the discrete for a bone remodelling problem, will show how the use of finite elements such as trusses or frames (see the formulation of each one in the annexes) can result in easier implementations and faster simulation times.

2. Implementing discrete based modelling and the finite element method for structural and biological applications

2.1. Introduction

The field of cellular materials has benefited from recent advances in manufacturing, specially additive manufacturing (AM), the recent increase of importance of cellular materials is due to advantages in contrast with homogeneous materials, such as the possibility of local configuration and adding multiple functions at component parts (Schaedler and Carter 2016). Cellular materials may be defined as heterogenous arrangements that have two key characteristics: A unit cell that conforms a certain arrangement of material and space, and repetition which indicates that the unit cell is reproduced along one or more dimensions, resulting in a pattern that may not be regular and could include many different types of unit cells (Bhate et al. 2019). In mathematics, tessellation refers to the portioning of a domain into smaller cells or parts, this has applications in many fields, e.g., robotics, structural design, biology, architecture, machine learning, among others. In Fig. 9 some of the possible fields of application of cellular materials are depicted.

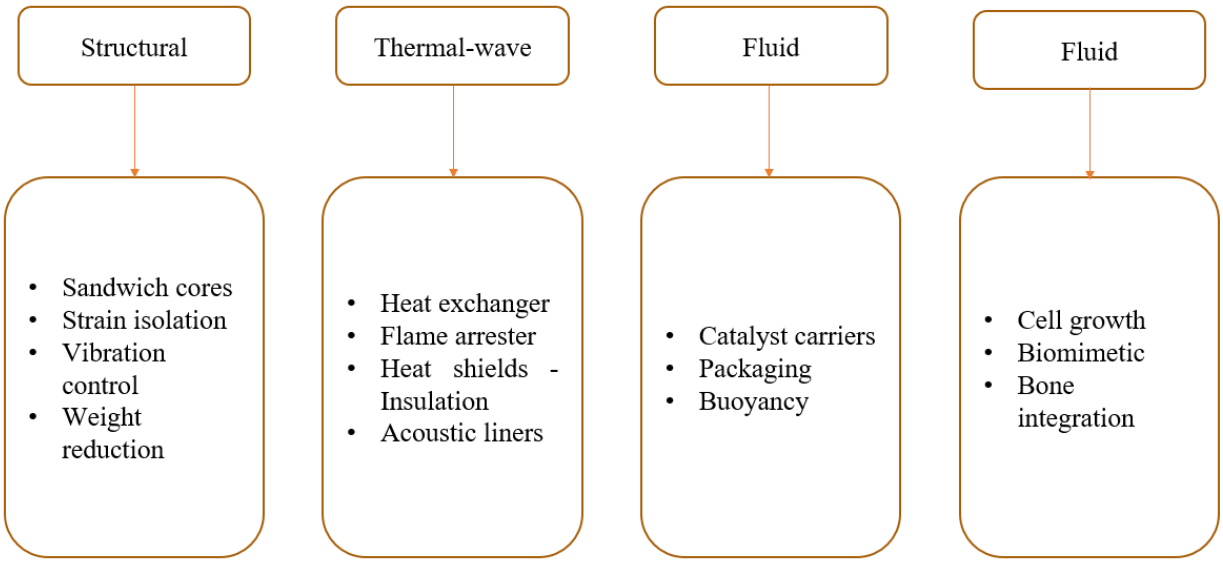

Fig. 9: Application for cellular structures adapted from (Bhate et al. 2019)

There are different types of tessellations, as seen in Fig. 10, each one has different features that make it more suitable for a specific application, the main focus on this study will be on Voronoi/Delaunay stochastic and triangular periodic tessellations. Voronoi tessellations are also called Dirichlet tessellations, thanks to the mathematician Gustav Dirichlet in 1850 who first proposed an algorithm to divide the Euclidean space in such a way that over a set of points distributed over a domain, each polygon resulting from the division is limited by a perimeter that is equidistant to any neighbor points. Alfred H Thiessen (1911) used this technique to make a prediction climate model, being the reason why, the resulting divisions are also known as Thiessen polygons. Georgy Voronoi (1907) made important contributions to this algorithm as well, and for this reason it is widely used the term Voronoi tessellation. Other type of widely used type of tessellations, correspond to Delaunay triangulations, named in honor to Boris Delaunay, a Russian mathematician that in 1934 derived the algorithm to obtain this partition. Delaunay and Voronoi tessellations are classified as dual tessellations because once either one of them is completed, obtaining the other results in a simple procedure.

In the field of cellular material design, the finite element method is a powerful tool to predict the mechanical behavior considering the homogenization principle, there are different approaches to model the unit cell of the lattice, in this chapter, a study on the implementation of Voronoi, Delaunay, and triangular tessellations on optimized topologies will be made, using the finite element method with a discrete based approach employing frame elements. This examination will also give insight on how the proposed tessellations will perform when used in additive manufacturing, to this purpose, various specimens with different porosities were created based on the tessellated geometries and printed using a stereo lithography (SLA) resin 3d printer, then, each specimen was subjected to a compression load until it reached failure and the results obtained with the discrete approach were compared to those found experimentally.

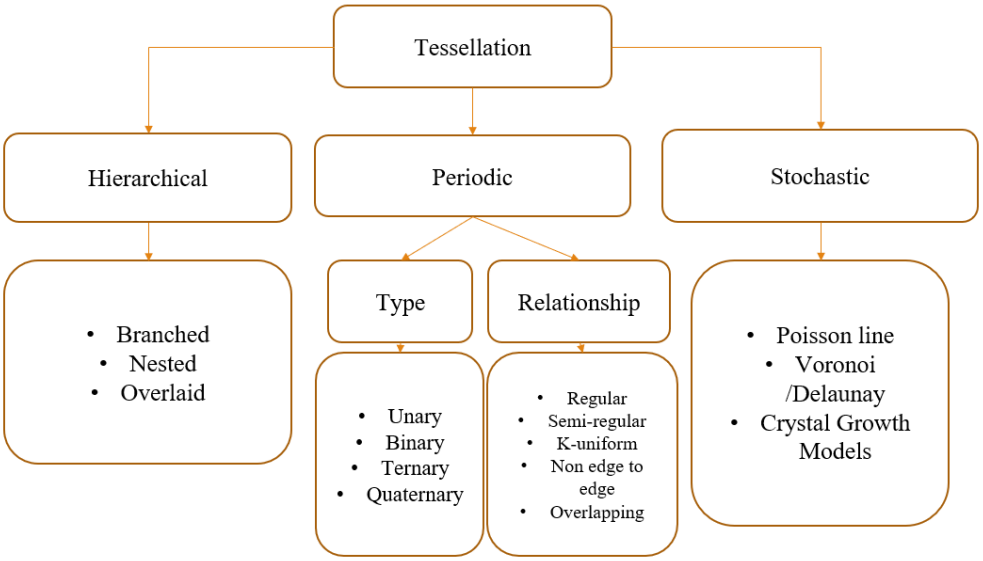

Fig. 10: Different type of tessellations

2.2. Methods

In Fig. 11 are shown some of the tessellations obtained with the methodology proposed by (Fahir et al. 2020) using an algorithm implemented in Grasshopper (McNeel, USA), in this case applied to the contour of a human femur. The seed points used by the algorithm correspond to different overlapped random point clouds to favor the highest densities from trabecular bone (KOCH 1993). The algorithm features the ability to approximate the number of pores which may help to obtain a desired porosity as seen in Fig. 11.

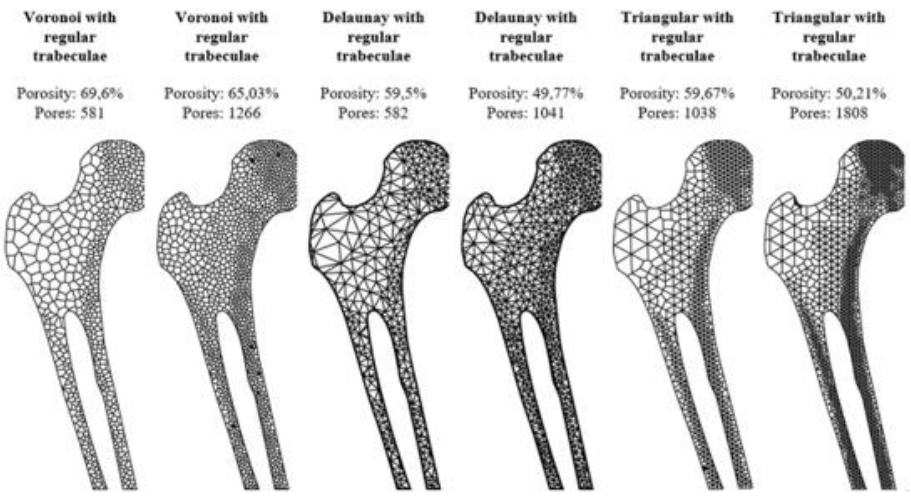

Fig. 11 : Delaunay and Voronoi tessellations with different porosities.

With the aim to test a discrete based modelling, each line from the resulting tessellation will be modelled as a frame finite element (formulation can be seen in the annexes). The corresponding 1D element mesh was exported from Grasshopper and the finite element formulation (direct formulation) was implemented and solved in ABAQUS (2017) employing the UEL solver. To better appreciate the reach of this methodology , it was applied to a famous optimization scheme proposed by (Andreassen et al. 2011) and implemented in MATLAB, so the tessellation will be performed on an optimal topology for stiffness as will be explained in the mathematical formulation from this particular optimization scheme.

A test specimen was designed as seen in a frontal view in Fig. 12, with a rectangular portion of 140 mm by 61.8 mm, with disk plates in the extremes with 15.6 mm in width and 140 mm in diameter. This geometry was optimized in a compressed loading condition by using an optimization scheme adapted from (Andreassen et al. 2011)which implements a power law approach. The boundary conditions correspond to those shown in Fig. 12 and the blue zones were set as a constraint to avoid optimization. These constraints correspond to the disks where the compressive load will be applied. This scheme is able to find optimal material distribution by minimizing compliance c(x), and taking as a constraint the porosity of the material f. In Eq. 6, U is the global displacement, K is the global stiffness matrix, u_e is the element displacement vector, k_0 is the element stiffness matrix, E_e is the elastic modulus in each element which dependents on x_e, the assigned density to element *e* between 0 and 1.

In mathematical terms the problem can be expressed as follows:

$$min_x : c(x) = U^T K U = \sum_{e=1}^{N} E_e(x_e) u_e^T k_0 u_e \qquad \text{Eq. 6}$$

$$\text{Subjected to: } \frac{V(x)}{V_0} = f \qquad \text{Eq. 7}$$

$$KU = F \qquad \text{Eq. 8}$$

$$0 \leq x \leq 1 \qquad \text{Eq. 9}$$

After each iteration the elastic modulus E_e is updated following a power law approach where E_0 is the stiffness of the material, E_{min} is a stiffness assigned to prevent singularities solving the system, p is the penalization factor, which was 3 in this case.

$$E_e = E_{min} + x_e^p (E_0 - E_{min}) \quad \text{Eq. 10}$$

To solve this problem, an optimality criteria method is used to find the optimum compliance (minimum) as a function of density (x_e). To this purpose, the sensibilities of the objective function are calculated as shown in Eq. 11 and Eq. 13, so the optimality condition is met with coefficient B_e where the lagrangian multiplier λ is set to satisfy the constraints.

$$\frac{\partial c}{\partial x_e} = -p x_e^{p-1} (E_0 - E_{min})\, u_e^T k_0 u_e \quad \text{Eq. 11}$$

$$\frac{\partial V}{\partial x_e} = 1 \quad \text{Eq. 12}$$

$$B_e = \frac{-\frac{\partial c}{\partial x_e}}{\lambda \frac{\partial V}{\partial x_e}} \quad \text{Eq. 13}$$

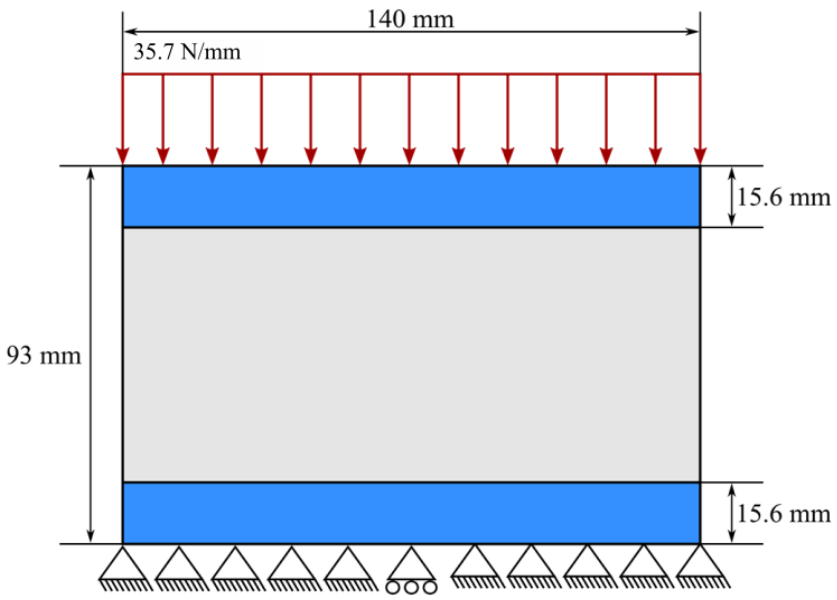

Fig. 12: Test specimen

The TO algorithm from (Andreassen et al. 2011) has the feature to set a given volume fraction as a stop criterion, so simulations with 40 %, 60% and 80% were chosen to be analyzed. The material properties in the simulation were those of the post cured resin used in the SLA 3d printing process (GREY FLGPGR04), this is, an elastic modulus of 2.8 Gpa and a Poisson ratio of 0.3. The resultant topology for different fraction volumes is seen in Fig. 13.

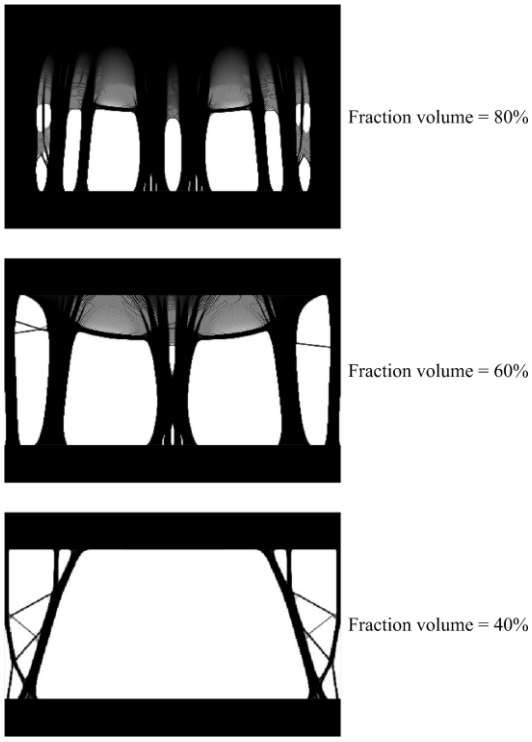

Fig. 13: Optimized topology.

After the geometry has been optimized and then tessellated for each case, the finite element problem with a discrete based approach is solved with the algorithm shown in figure Fig. 14. The information mesh for each tessellation (nodes coordinates and connectivity files) was exported using grasshopper and each element corresponding to a tessellation segment was considered as a frame element, this type of element was chosen given its capability to bear moments which would represent better the physical behavior of each trabeculae like structure in the specimens. On the other hand, truss elements were discarded due to this lack in rotational freedom at each node (see annexes to see mathematical formulation) although in the next chapters some test with this type of element will be presented to represent other study cases. The upper and bottom portions of the specimen corresponding to the support plates that transfer the load to the portion of interest are not considered in the FEM simulations, only the domain shown in Fig. 15.

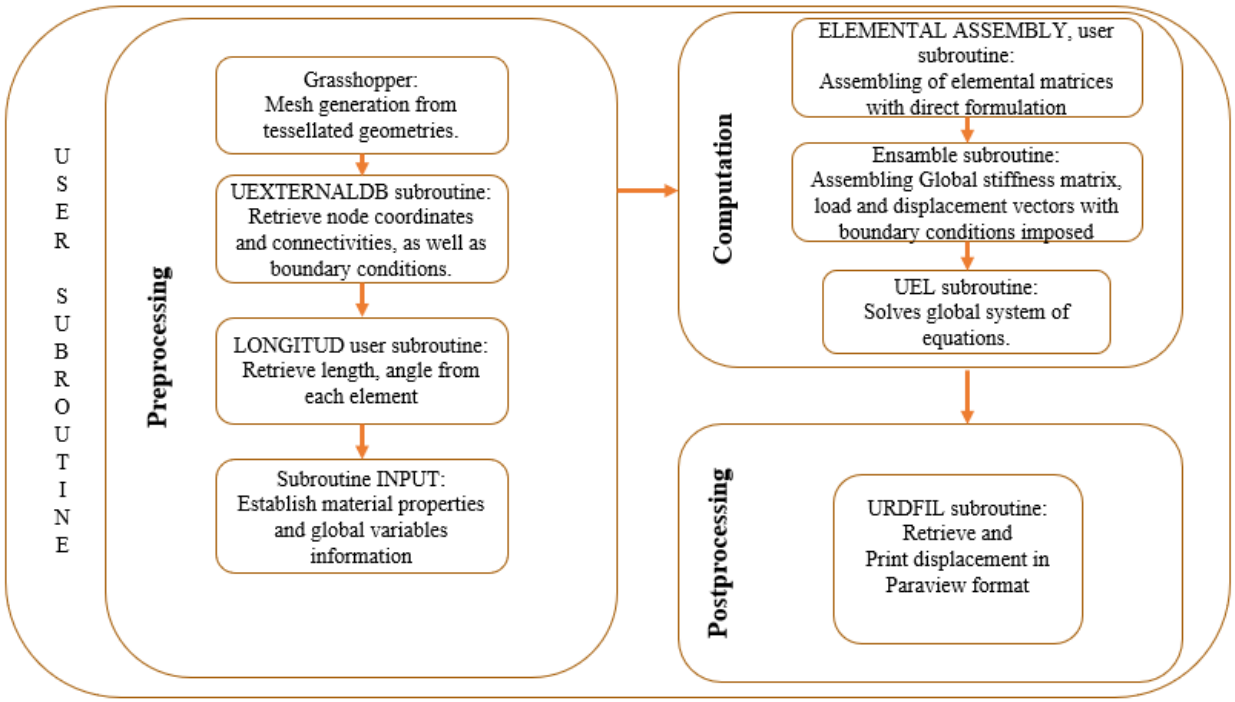

Fig. 14 Finite element algorithm implemented in user subroutine solved with ABAQUS (2017) UEL solver.

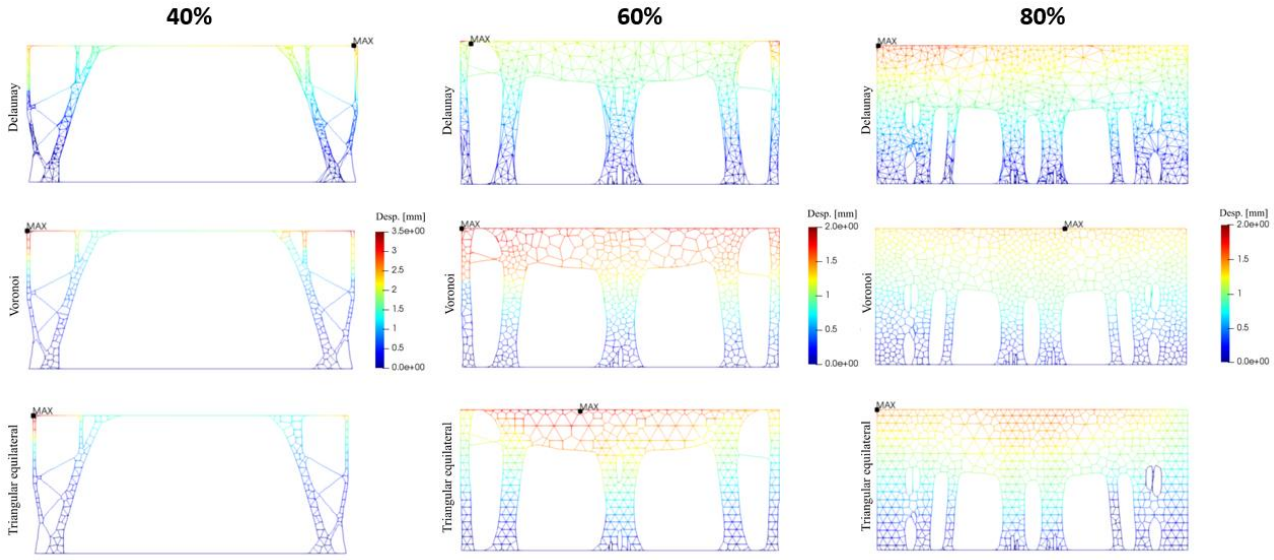

Fig. 15: Displacement fields in specimens using frame elements

In total 10 specimens tessellated with random Voronoi, random Delaunay, and equilateral triangles with a fraction volume of 40%, 60% and 80% were 3d printed (the percentage refers to

the volume fraction set as stop criterion with the TO algorithm), with the addition of a specimen with no tessellation and a 100% infill. The 3D printer used corresponds to a Formlabs-2 printing system (Formlabs, Somerville, Massachusetts), the thickness of each layer was set in 0.1 mm. Each specimen was subjected to a compressive load at a rate of 0.5mm/min, and each one was tested until failure by fracture. The machine used corresponds to the model AG-X plus by Shimadzu with a total capacity of 30 tons (300kN).

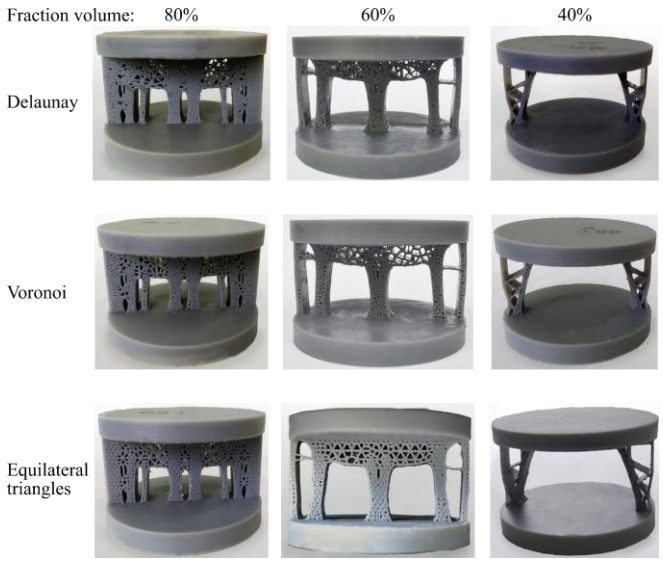

Fig. 16: Test specimen

Something to note is that because of the limit in resolution in the manufacturing process, some pores in each specimen resulted in full density zones, resulting in a porosity slightly greater than in the cad files used or the FE simulations.

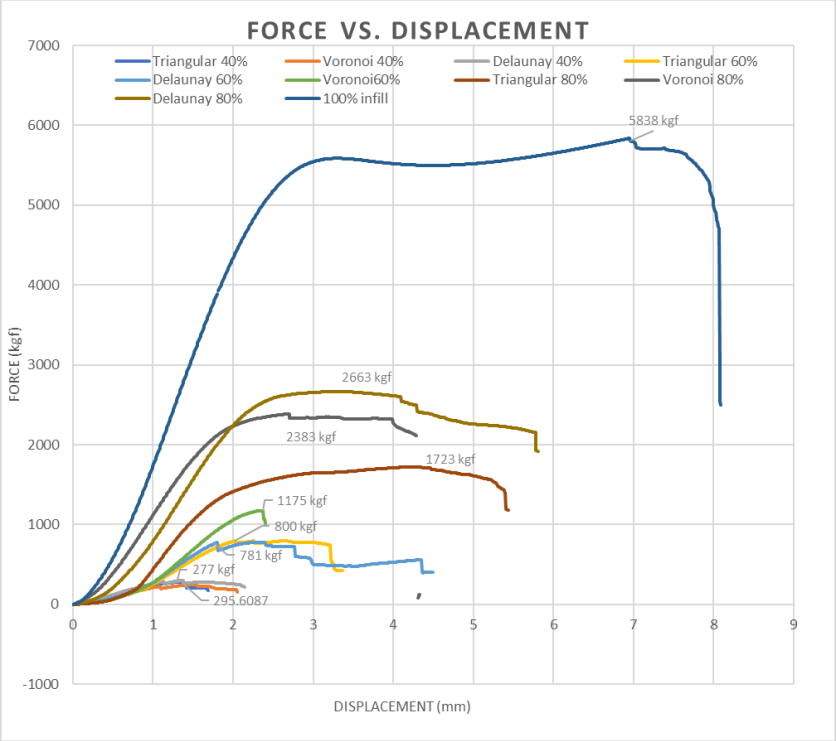

Fig. 17: Force (Kgf) vs displacement (mm) for every specimen

In Fig. 17 the failure trajectory is shown for each specimen and the maximum force is specified. An apparent plastic behavior is seen, but in each specimen when the elastic linear portion ends, cracks start to occur in various trabeculae like elements, resulting in a plastic behavior in the displacement curves showed above. In the discussion section a comparison between the experimental results and the discrete based modelling for displacements at a load of 500 Kgf will be shown.

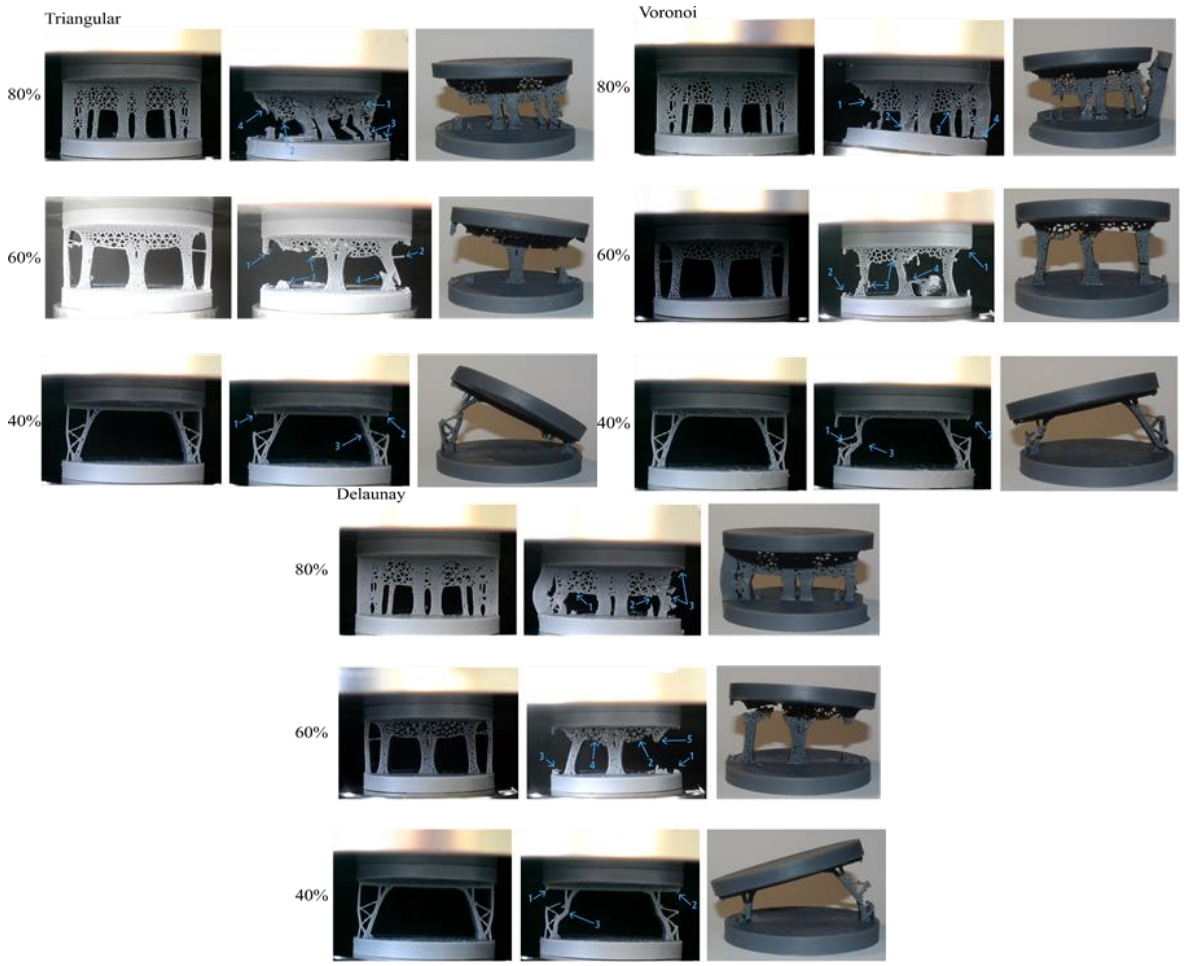

Fig. 18: Specimens before and after failure.

2.3. Discussion

There is an appreciable error regarding the displacements obtained in the FE simulations and those obtained experimentally for each specimen. This error can be attributed to different factors, first, the 3d printed models resulted with a lower porosity than intended because of pores that were too small and were clogged with resin. The added material would result in an increased stiffness of the specimen by increasing the surface area along critical loading paths occur, in addition, the added material could modify the cross-sectional area of some frame elements, as well as its corresponding inertia. These observations, would explain why all the experimental displacements were smaller than in the simulations by a maximum of 40% as seen in table 1.

Second, another possible explanation on the dissimilarities on the obtained displacements befalls in the type of formulation used for every discrete element, as it is seen in the annexes, for the

frame element, the degrees of freedom for a Bernoulli-Euler beam were superposed to those of a truss element (resulting in a frame element). It has been stated that Bernoulli-Euler beams are most adequate to model long beams with lean cross-sectional areas, and in some cases in the tessellations obtained, rather short elements can be seen at the base of the columns, although this might not suppose a problem to model this specimen structure since the length of the element is still greater than its cross sectional length; to clarify this hypothesis an implementation of the Timoshenko beam might be used to superpose to the frame element, instead of the used here to compare the resulting displacements.

Nevertheless, the theoretical findings have the same tendency as the experimental data, greater displacements for triangular, Delaunay, and Voronoi tessellations, respectively. This tendency and the fact that triangular tessellation had greater displacements may be because of the tessellation method, there are different number of elements even if the geometry has the same porosity, take as an example a pore in triangular tessellation and one with Voronoi, the first has 3 elements, while the pore with Voronoi has a variable number, ranging from three to six elements. This fact means that there is a slight difference in density between the simulations, product of difference in perimeter in pores depending on the tessellation method. Is worth emphasizing the fact that the percentage classification is based on the topological optimization algorithm, which changes once the domain has been tessellated.

	FE (mm)	Experimental (mm)	Error (%)
Delaunay 60%	1.48	1.33	15
Voronoi 60%	1.39	1.29	10
Triangular 60%	1.67	1.39	28
Delaunay 80%	1.16	0.78	38
Voronoi80%	1.09	0.69	40
Triangular 80%	1.21	1.04	17

Table 1: Displacement comparison

2.4. Conclusions

This chapter presented an introduction to the implementation of discrete based modelling with the aim of modelling a mechanical problem, which consisted in finding displacements in the elastic range using FEA with frame elements of tessellated geometry. Voronoi, Delaunay and triangular tessellation was used to obtain the topology present in each test specimen and in the simulations, after performing topological optimization at the initial domain (as seen in Fig. 13).

The results show how the method was able to predict the displacements with the error shown in table 1, and more importantly the trend of displacement among the different topologies, it predicted the same order of amplitude in displacements, allowing to infer that although this methodology might not be too precise in some cases, is able to describe correctly the overall mechanical behavior of a tessellated material.

As it was said in the discussion, using a Timoshenko beam might be a better alternative in cases where the element is not that lean, a future work could be to test this approach. In addition, a manufacturing method with higher resolution could be used to avoid the clogging of the smaller pores.

3. A simple and effective 1D-element discrete-based method for computational bone remodeling

3.1. Introduction

The bone remodeling process consists of multiple dynamic interactions between several cell types and signaling pathways that respond to different mechanical and biological conditions to repair bone damage and preserve homeostasis of needed minerals while preserving bone integrity. The main cells involved in the process are osteoclasts, osteoblasts, and osteocytes. Insights in the understanding of bone remodeling, involving the mechanisms that couple bone formation and resorption, specifically in pathological cases such as osteoporosis which affects more than 200 million people (Sozen, Ozisik, and Calik Basaran 2017), have led to the development of mathematical models. This provides a quantitative tool to help the understanding of existing correlations between mechanical loads applied to a bone's portion and biological variables in the remodeling process, such as resorption and formation rate (Raggatt and Partridge 2010).

Five phases set up the bone remodeling process: activation, resorption, reversal, formation, and quiescence. These processes occur continually, being key aspects in understanding bone remodeling. The most relevant works found in the literature address partially or totally each one of these phases. One of the first models to relate mechanical loads to bone remodeling was Wolff's model, published in 1807. Wolff states that bone remodeling occurs in response to changes in the stress distribution in bone; this leads to a reorientation of the trabeculae. This new configuration has a topology determined by the stress field, following the principal stress trajectories (Cowin 1986). This first research established the foundations of the mechanics of modern bone remodeling, allowing for deeper research on how calcium homeostasis works, how local micro-damage repair occurs, and which biological factors are most important in this process (see for instance van Lenthe and Müller 2006 and Pivonka et al. 2008). During the mid-20th century several cell population models were developed; (Lemaire et al. 2004) relates the activation of osteoblasts and osteoclasts which depends on the RANK-RANKL-OPG signaling pathway; the model uses the mature and immature portion of the osteoblast population to control the degree of osteoclast activity. (Geris, Sloten, and Oosterwyck 2010) proposed a model

using partial differential equations to describe bone formation; this approach uses a time-space scheme that varies according to cell densities and concentrations of growth factors. (Sun et al. 2013) postulated a growth-factor diffusion model in which ordinary differential equations describe signaling pathways activity. Also, this model includes agents that simulate the action of various cell types involved in vascularized bone regeneration within a CaP scaffold loaded with growth factors. (Vanegas-Acosta et al. 2011) also used diffusion models to reproduce the patterns found in different healing processes occurring in the osseointegration of a dental implant; this model helps to predict the degree of acceptance and anchoring of the implant.(Komarova et al. 2003) proposed a set of differential equations for populations of osteoclasts, osteoblasts. The model implements regulating factors to produce periodic solutions that adequately represent the biophysical process which correlates the phases of activation and resorption. The model stated by (Nackenhorst 1997) is based on strain energy as the main determinant of localized bone density in trabecular structures. This model proposed a set of bone remodeling differential equations integrated with the finite element method using 2D elements. The solution obtained resembles density distribution showing the formation of the main trabecular groups. It has been found that using the finite element analysis to find field variables such as energy strain or stress and considering them as biological stimuli is useful in modeling other phenomena besides bone remodeling, as is the case of bone growth; see (Guevara et al. 2015). Boundary-based strategies for bone remodeling can also be found; one of the main advantages of this approach is the simplicity of the discretization since only the boundary is meshed. The use of boundary integral methods such as the Boundary Element Method (BEM) has been proposed by (Martínez and Cerrolaza 2006) and (González, Cerrolaza, and González 2009). Their results show that BEM, used together with damage mechanics, is a powerful tool in bone remodeling and adaptation. Modeling techniques such as B-spline were used in BEM-based approaches to investigate biomedical applications (Annicchiarico, Martinez, and Cerrolaza 2007). More recently, the effects of piezoelectricity in bone remodeling have been modeled using BEM as reported by (González, Cerrolaza, and González 2009), while the behavior of vertebral discs under dynamic loading was also reported by (Cerrolaza, Nieto, and González 2018).

Up to this point, bone architecture has been mainly addressed by modelling the bone trabeculae obtained from CT scans as 2D or 3D continuum elements or even 1D-beam elements arranged

with different distributions (e.g. periodic honeycombs or a more random distribution). This implementation of 1D elements to represent bone architecture can reduce the model complexity thus leading to advantage from a computational point of view (Ruff1. Ruffoni, D. & Van Lenthe, G. H. 3.10 Finite element analysis in bone research: A computational method relating structure to mechanical function. Comprehensive Biomaterials II vol. 3 (Elsevier Ltd., 2017).oni and Van Lenthe 2017). Using this approach, a decrease in orders of magnitude of the number of nodes has been found, allowing a 1000-fold reduction in CPUs time in the modelling of trabecular bone mechanical properties (van Lenthe and Müller 2006). For this reason, we propose a 1D-element discrete method for the bone remodeling problem, being its main attractiveness the use of elements that resemble trabecular bone and its low computational cost. This procedure enables researchers to increase the sample size and the complexity of trabecular bone. Until now, there are no models using this 1D approach to solve the bone remodeling problem. Therefore, we present a methodology based on the approach used by (Garzón-Alvarado and Linero 2012a) which employs a dimensionless density that depends on the energy strain (see Eqn. 1) and uses different integration schemes like Heun, Euler and Runge-Kutta to solve this equation, where the use of one scheme or another did not lead to any appreciable difference. The change over time in density λ depends on variables k_1 and n which are found experimentally, the energy strain U in each step is divided by a reference strain energy value U_{ref} that determines the limit at which remodeling occurs. The work of (Garzón-Alvarado and Linero 2012a) is of great importance for the proposed methodology since it is able to correctly model the behavior of trabecular bone using 2D continuous elements.

The implemented remodeling methodology has one additional feature in comparison with the (Garzón-Alvarado and Linero 2012a). This chapter proposes a new approach to model the bone remodeling problem based on previous works with a low computational cost compared with methodologies using continuum domain elements (van Lenthe and Müller 2006), allowing the implementation of more complex structures and sample sizes in the simulation of bone remodeling dynamics and bio-inspired conceptual designs.

3.2. Methods

In this section, the bone remodeling model is presented as well as the developed algorithm. In addition, two benchmark tests (Valdez et al. 2017) are analyzed for validation purposes.

3.2.1. Model description

The proposed remodeling algorithm is shown in Fig. 19, where the constitutive elements of the domain correspond to either frame or truss finite elements. To create this model the coupling of the moment equation (Eq. 15) with the density equation (Eq. 14) is required in order to relate the strain energy to the element density, thus setting the bone remodeling dynamic. This modifies the modulus of elasticity as observed in equation (Eq. 16), where $E(\lambda)$ is the elastic modulus, λ is the dimensionless density, and n is an exponent found experimentally. In equation (Eq. 15) σ is the stress tensor and b the body forces vector.

$$\frac{d\lambda}{dt} = k_1 \left[\lambda^{n-1} \frac{U}{U_{ref}} - 1 \right] \qquad \text{Eq. 14}$$

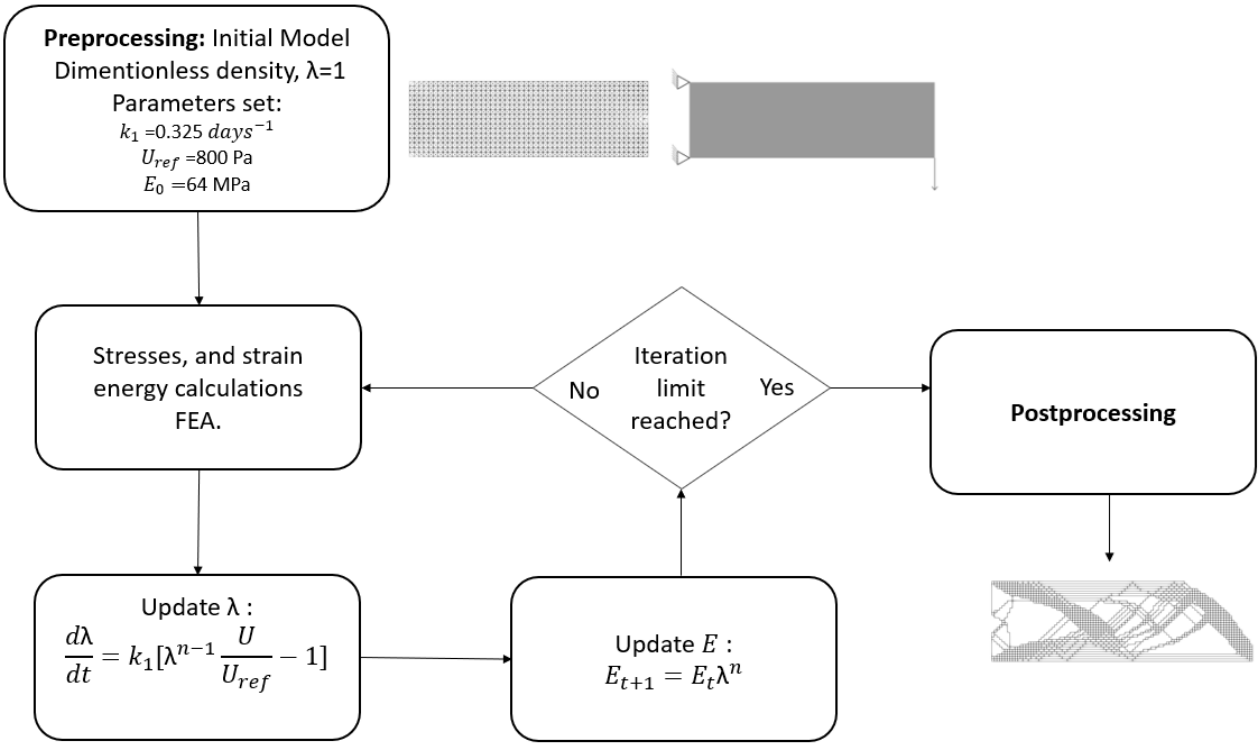

Fig. 19: Proposed algorithm

$$\nabla^T \sigma + b = 0 \quad \text{Eq. 15}$$

$$E(\lambda) = E_0 \lambda^n \quad \text{Eq. 16}$$

To find the maximum stress, superposition was used in a fiber of an element by adding both the stresses due to the axial load P and the stresses due to the maximum bending moment M_{max} (see Eq. 19). It should be remarked that the loads and moments are applied at the corresponding nodes. Each element is assumed to have a circular cross-section area *A*, moment of inertia *I* and a vertical distance away from the neutral axis *C* (Eq. 17). M_i^{left} and M_i^{right} are the concentrated moments at both ends of the element (Eq. 19).

$$\sigma = \frac{P}{A} + \frac{M_{max} C}{I} \quad \text{Eq. 17}$$

Similarly, deformation energy due to axial load and bending moments is expressed as:

$$U_{strain} = \frac{1}{2} \int_0^L \frac{{P_i}^2}{EA} dx + \frac{1}{2} \int_0^L \frac{M^2(x)}{EI} dx \quad \text{Eq. 18}$$

Solving these integrals yields the strain energy, as stated by (Makris, Provatidis, and Rellakis 2006), (derivation can be seen in the annexes):

$$U_{strain} = \frac{1}{2} \sum_{i=1}^{N} \left[\frac{{P_i}^2 L_i}{E_i A} + \frac{1}{3} \cdot \frac{(M_i^{left})^2 + (M_i^{right})^2 + M_i^{left} \cdot M_i^{right}}{E_i I} \cdot L_i \right] \quad \text{Eq. 19}$$

3.2.2. Numerical implementation

To solve the finite element equations for frame and truss elements, a user subroutine was programmed and attached to ABAQUS (2017). Euler's method was used to solve equation (Eq. 14) as shown in equation (Eq. 20)

$$\lambda_{t+1} = \lambda_t + k_1 \left[\lambda_t^{n-1} \frac{U}{U_{ref}} - 1 \right] \Delta t \quad \text{Eq. 20}$$

A time step Δt = 0.1 days was used. Constant k_1 was 0.325 days $^{-1}$ and n was 2.0. The reference energy constant U_{ref}, which determines the threshold at which remodeling occurs was set to 800 Pa, these constants are based on the previous works of (Garzón-Alvarado and Linero 2012a) . It is worth mentioning that the algorithm stop condition was set to 100 days of simulation time, since at this time cell population dynamics have reached a quasi-steady-state (Buenzli, Pivonka, and Smith 2011). A general description of the algorithm in terms of the programmed subroutines can be seen in Fig. 20.

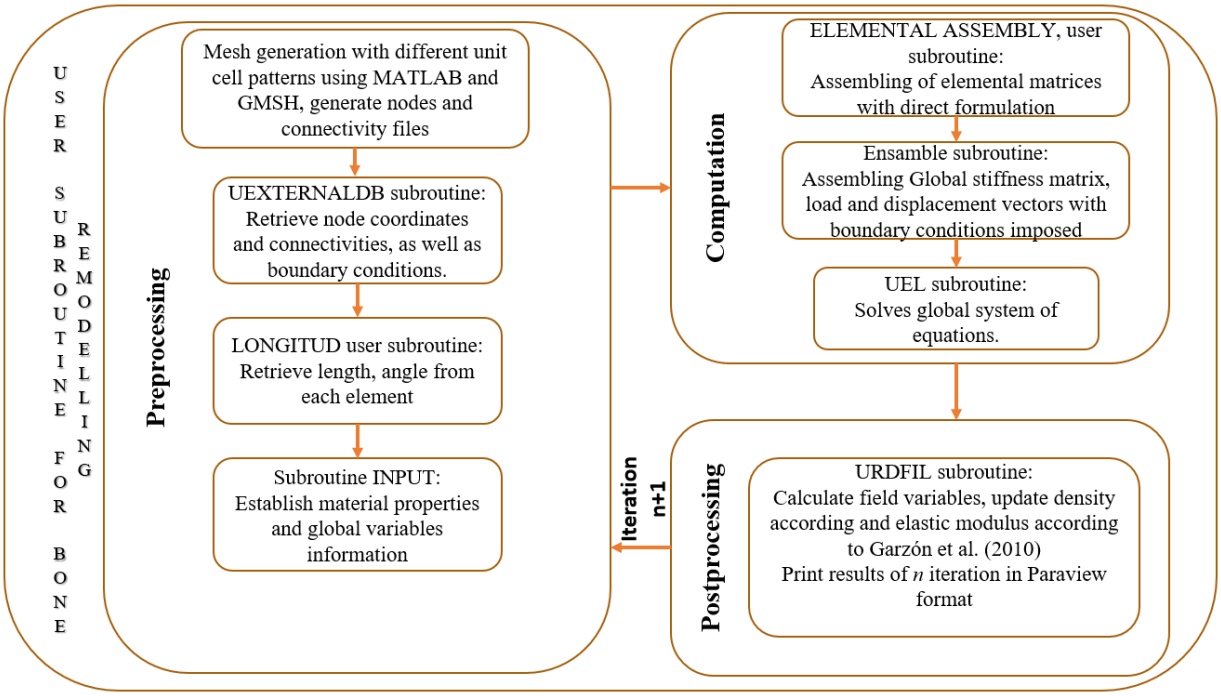

Fig. 20 :FE algorithm implemented in ABAQUS (2017).

3.2.3. Unit cell topology

Unit cells of different shapes (hexagons, squares, and triangles as shown in Fig. 21) were tested in two benchmark tests: the cantilever beam displayed in Fig. 22(a), and the square plate subjected to a distributed load shown in Fig. 22(b). According to (Luxner et al. 2009) it is expected that unstructured meshes resemble better the mechanical behavior of trabecular bone since a more disordered cellular structure prevents early crack formation, once a load has been applied. Finally, it was tested which formulation (truss or frame) was most suitable for the remodeling

algorithm based on the resulting topology, and then its results compared with previous works on topology optimization and with the benchmark tests described in the next section.

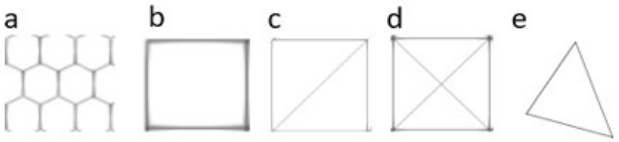

Fig. 21: Different unit cells
Different unit cells tested: (a) Hexagonal or honeycomb. (b) Square cells. (c) Triangular cells. (d) Square Cells with two diagonals. (e) Triangle.

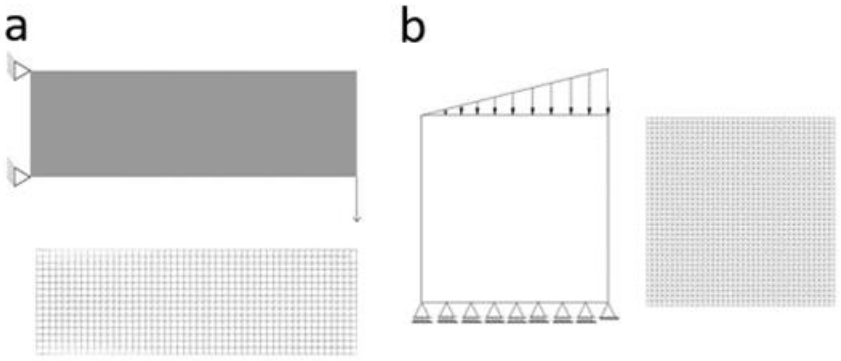

Fig. 22: (a) Cantilever beam, (b) Square plate with distributed load

3.2.4. Benchmark tests and model validation

In order to test the computational model, two benchmark tests were performed. First, a cantilever beam was used as the initial domain that was discretized using frame and truss elements. The meshes reproduced were made with different aspect ratios and distributions. Several element lengths (h) ranging from 2.4m to 0.15m were used to see the effectiveness of the method in each mesh. Only elements with a density higher than one (1) unit are shown in Fig. 24 to Fig. 28 to better appreciate some of the resultant topologies, whereas in Fig. 23 the continuous field of density (lambda) is shown; as the benchmark results are not the main focus, only a few cases are enough to evidence viability, a few more examples are shown in the annexes section.

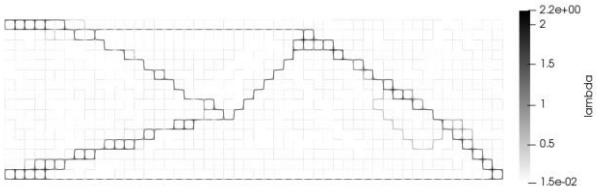

Fig. 23: Density for the cantilever beam at 100 days, element length 0.3m.

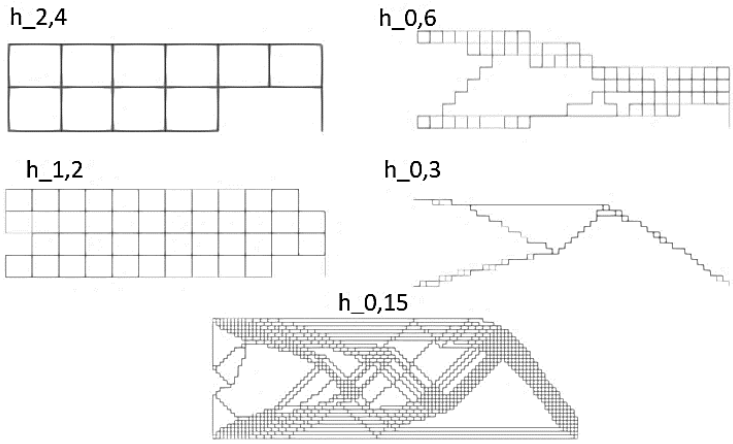

Fig. 24: Square frame cell unit structure remodeling.

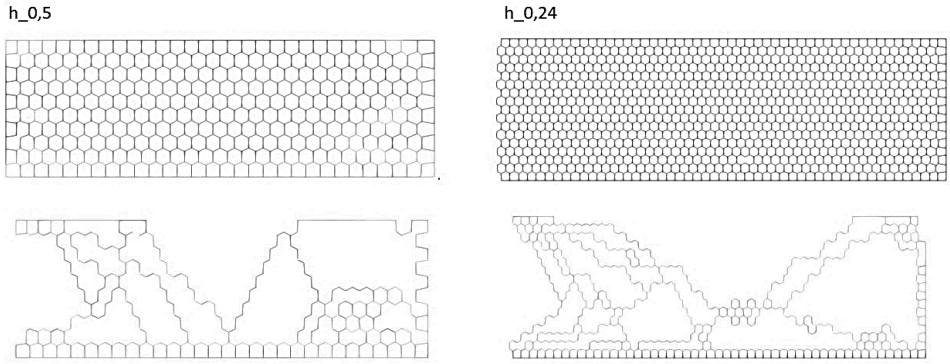

Fig. 25: Polygon cell unit structure remodeling; frame elements.

In Fig. 24 and Fig. 25 the resultant topologies of the discrete bone remodeling algorithm are shown with different element sizes and types of unit cells, while Fig. 26 depicts a triangular unstructured mesh. The results obtained with this methodology resemble those of a topological optimization algorithm for this benchmark test (Fig. 29). Examining the benchmark results, it can

be noted that the method shows a high sensibility to the type of unit cell that sets up the initial domain. This can be seen in Fig. 24 and in Fig. 27 where the meshes only differ in that the square configuration has an extra diagonal element in their unit cell, yet the final topology is different since the stress distribution changes at a unit cell level.

Finer meshes produce results that seem to be more similar to those of TO algorithms, so a rather fine mesh will be used in the study cases.

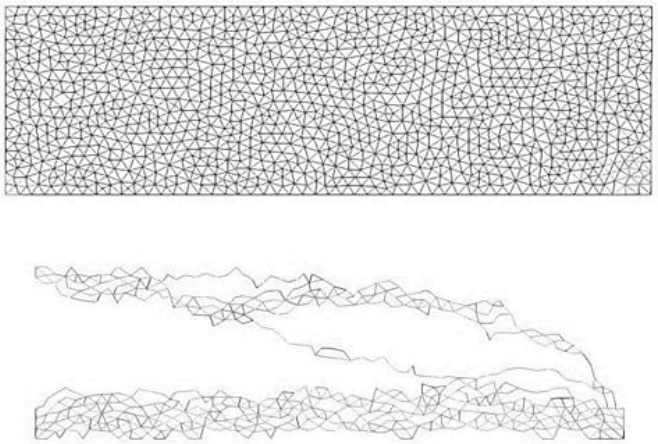

Fig. 26: Unstructured mesh remodeling with triangular unit cells.

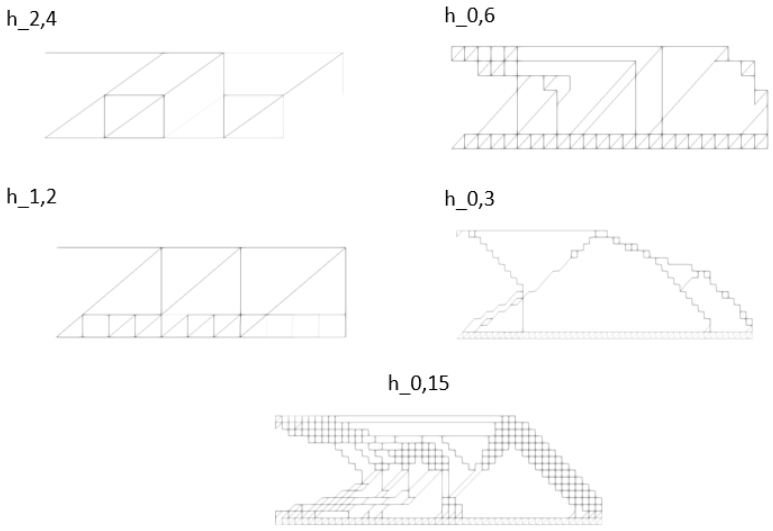

Fig. 27: Remodeling in structured meshes, triangular unit cell.

Fig. 28 displays a comparison between frame (three degrees of freedom: horizontal, vertical, and rotational displacement) and truss elements (two degrees of freedom: horizontal and vertical displacement). In this case, the capacity to bear moments is noted in the frame topology, since

the final result shows a structure with longer horizontal supports, whereas in the truss case a structure with long diagonal supports at an angle of 45° is seen along the structure. Both results are structurally consistent and serve as a conceptual basis for design. It is worth noting that although there are different results in the topologies obtained, the strain energy found in the structure stays the same but concentrated along the remaining trabeculae. With the aim in mind to address bone remodelling problems, frame elements will be used in further cases, since they can bear moments, similar to trabeculae structures.

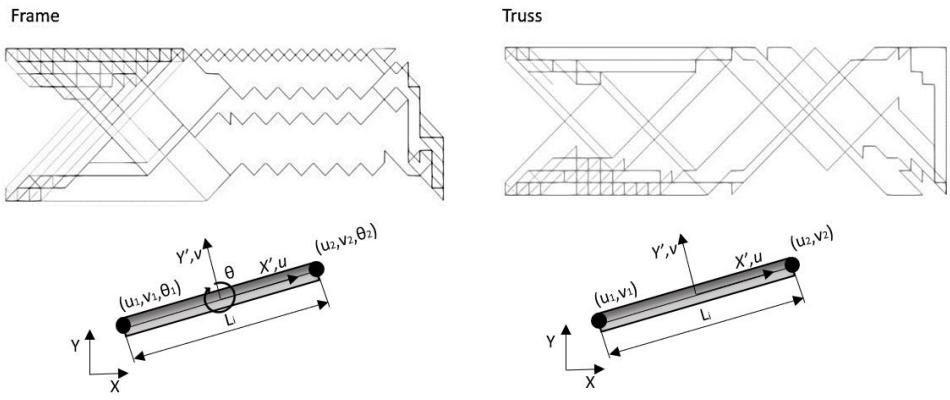

Fig. 28: Comparison between results of the bone remodeling problem using frame and truss formulation with a mesh setup by diagonal elements.

Fig. 29: Initial (left) and optimized (right) structure of a cantilever beam using a topological optimization algorithm (Chen et al., 2018)

Next, a test based on the implementation proposed by (Garzón-Alvarado and Linero 2012b)is discussed herein to compare similarities in the resultant topology. A triangular distributed load is applied on a square plate with the boundary conditions shown in Fig. 30(a) a comparison was made between Garzón's results using an element-based remodeling approach (using continuous, triangular elements) and the discrete remodeling algorithm proposed herein with frame elements. In this case, an increase in speed of more than 20% was found with the proposed methodology for meshes with 10000 nodes. The computer used had an AMD Ryzen processor (2.30GHZ) with 7 cores and 16GB RAM. With the continuum approach a simulation time of 100

days was achieved in 310 (sec) whereas with the new methodology the simulation reached that same span in 245 (sec) wall-clock time; in this case, the proposed methodology used the unit cell shown in Fig. 21(b).

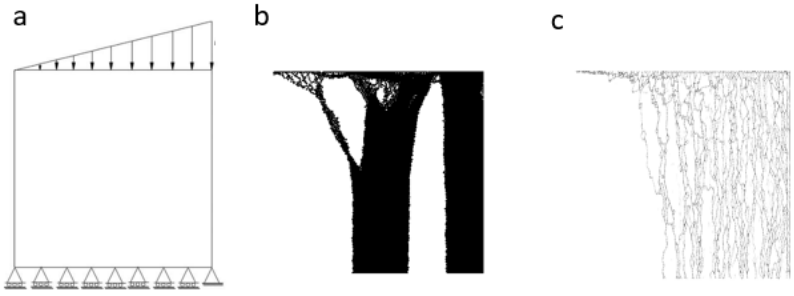

Fig. 30: Bone remodelling benchmarks
(a) Boundary conditions. (b) Result for bone remodeling problem using an element-based approach (Garzón-Alvarado and Linero 2012a)(c) Result of bone remodeling problem using discrete frame elements.

To this point, two benchmark cases have been tested with the proposed methodology showing results similar to those obtained in previous works with continuum elements. In the plate model a serious of column structures are formed at the base and have ramifications at the top part. In the cantilever benchmark test a serious of diagonal structures are formed as seen in Fig. 28. This is expected in this case since the methodology follows an objective function with the purpose of obtaining a preset specific energy strain value per unit bone mass. Regarding the square plate, there are differences in the topologies obtained, but the formation of structural columns with branches are seen in both cases Fig. 30(b) and Fig. 30(c); in the discrete case, the difference in column density might be due to lack of contact between the elements that hold the highest energy density.

Given that these benchmarks showed very good agreement with previous works, two study cases will be examined to further study the reach of this methodology. For the following medical cases the geometrical properties from trabeculae were adopted from studies from (Cesar et al. 2013) on skeletal microarchitecture, for each bone.

3.3. Results

3.3.1. Implementation in 2D

In this work two medical cases were subjected to our bone remodeling algorithm in an attempt to study the formation of the main trabecular groups. The first case, proximal femur, and the second, calcaneus cancellous bone, were considered in a specific stage of the walking gait according to previous studies. The resultant topologies in both cases resemble anatomical features found in the literature reviewed.

In the first medical case, proximal femur, the boundary conditions try to mimic the loading history of this bone where the main forces correspond to both the hip reaction force and the action of the abductor muscle during the gait cycle. The loading cases are based on the works of (Beaupre and Orr 1990). The boundary conditions of the initial mesh corresponding to an unstructured lattice with a triangular unit cell are shown in Fig. 31(left). The resultant topology with the formation of the main trabecular groups (in the density field) and relevant anatomical features are seen as well in Fig. 31(right). The results show the formation of groups of trabeculae that undergo compression or tension.

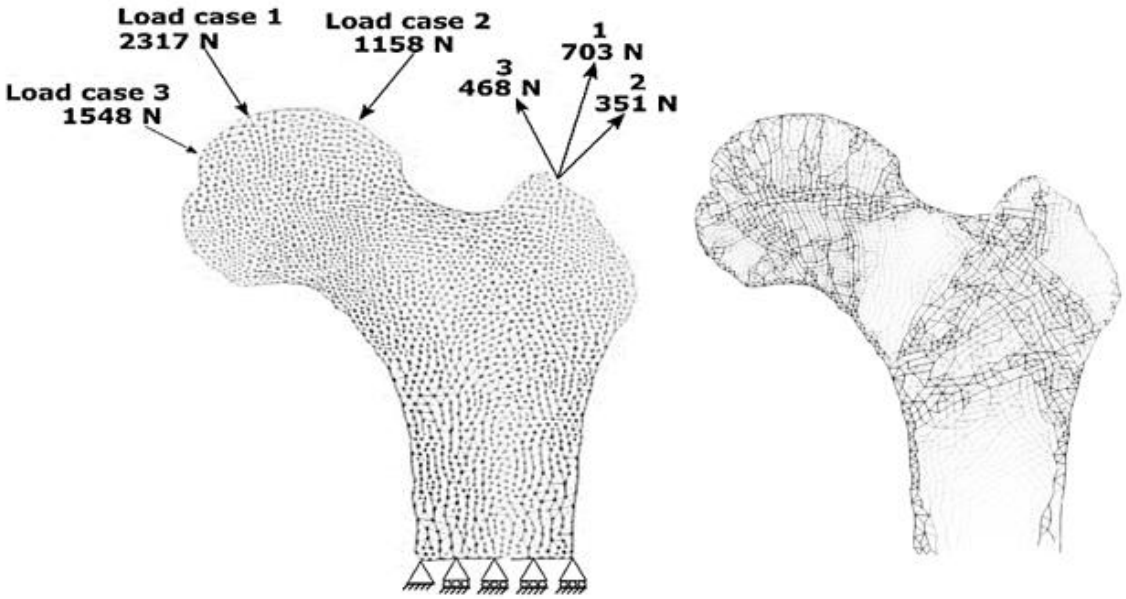

Fig. 31: Boundary conditions and topology obtained at t=100 days mass fraction, with periosteum set as a constraint.

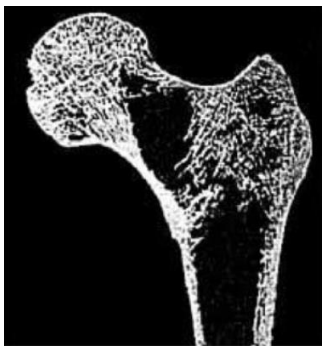

Fig. 32: Femur with low bone mass density (Osteoporosis) from ("Computer-Assisted Femoral Augmentation for Osteoporotic Hip Fracture Prevention" 2013)

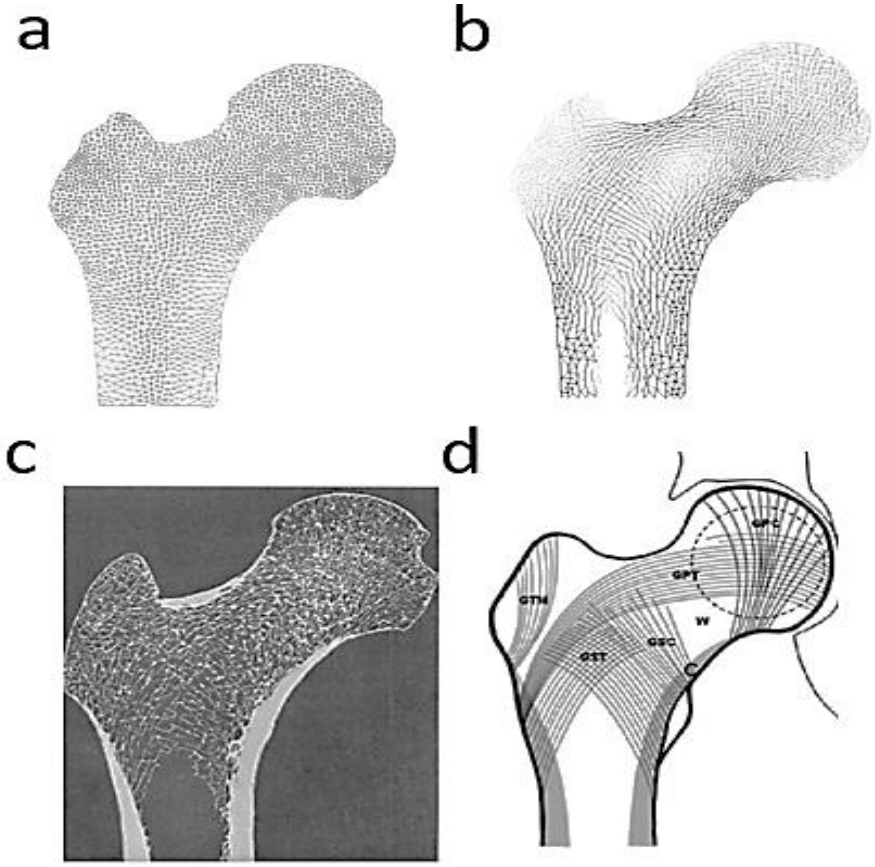

Fig. 33: Similarities in topologies obtained with bone remodelling
Bone topology (a) Study case: femur contour with initial triangular mesh and frame elements. (b) Topology obtained without restriction on the periosteum at 100 days. (c) Femoral frontal section through neutral axis, showing trabecular topology from (KOCH 1993). (d) Principal trabecular groups (Martín and Kochen 2011)

An additional condition was needed to solve these medical cases since the contour corresponding to the periosteum seemed to be affected by the remodeling algorithm. This issue was fixed by applying a constraint on each element belonging to the periosteum corresponding to a constant elastic modulus. For comparison sake, results of the femur case restrained with this condition, in figure Fig. 31 can be seen, whereas in Fig. 33(b) the density field is shown without the restriction. Something that called our attention is that the result in Fig. 31 seemed very similar to a bone with osteoporosis (as the one in Fig. 32), this could result from a low energy strain reference value in the algorithm. In case of the topology obtained in Fig. 33(b) an increase bone mass density was achieved. This change in density could result due to the fact that the restriction on the periosteum lowers the energy density distribution within the femur, so in this case some trabeculae won't reach the energy strain reference to achieve formation. The decrease in energy density is in part to the higher elastic modulus set on the periosteum, looking at Eq. 19 we can see that a greater elastic modulus means a lower strain energy for that element.

In the second medical case, calcaneus cancellous bone, the boundary conditions were suggested by (Belinha, Natal Jorge, and Dinis 2012) which represent a series of stages of the gait cycle. The different force values at each stage are collected in Table 1, while all boundary conditions are shown in Fig. 35(a). The boundary conditions in the second stage of this cycle are detailed in Fig. 34 along with the initial mesh; results show that trabecular groups undergo, mainly, compression stresses. In the calcaneus case the element size was set from the low end of the spectra of the characteristics reported by (Cesar et al. 2013), i.e. 55 micrometers. The restriction on the periosteum was set in these simulations as well.

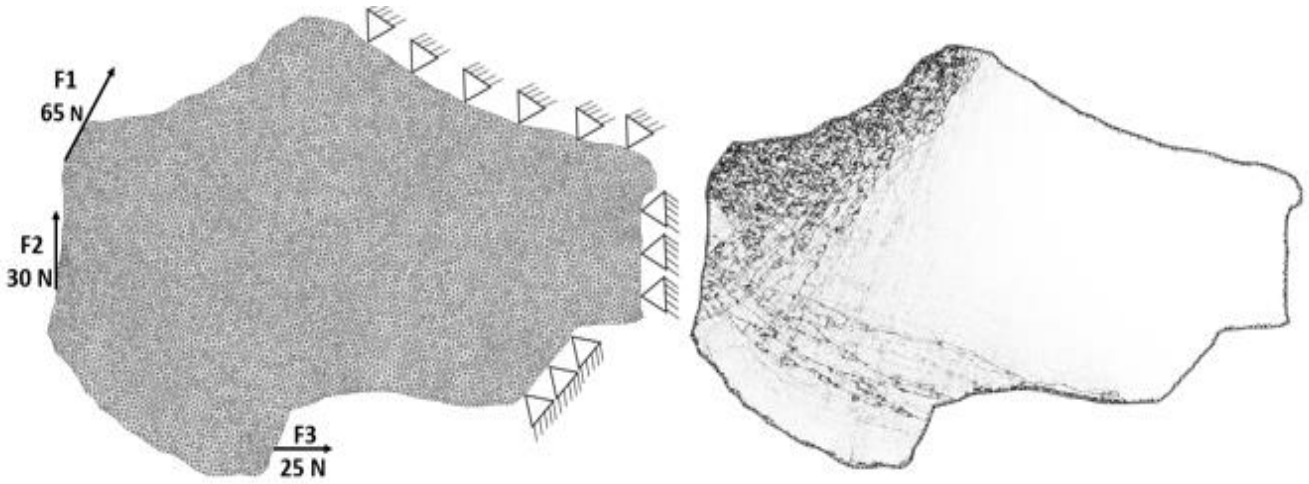

Fig. 34: Boundary conditions and topology obtained at 100 days, second load case, initial mesh is shown.

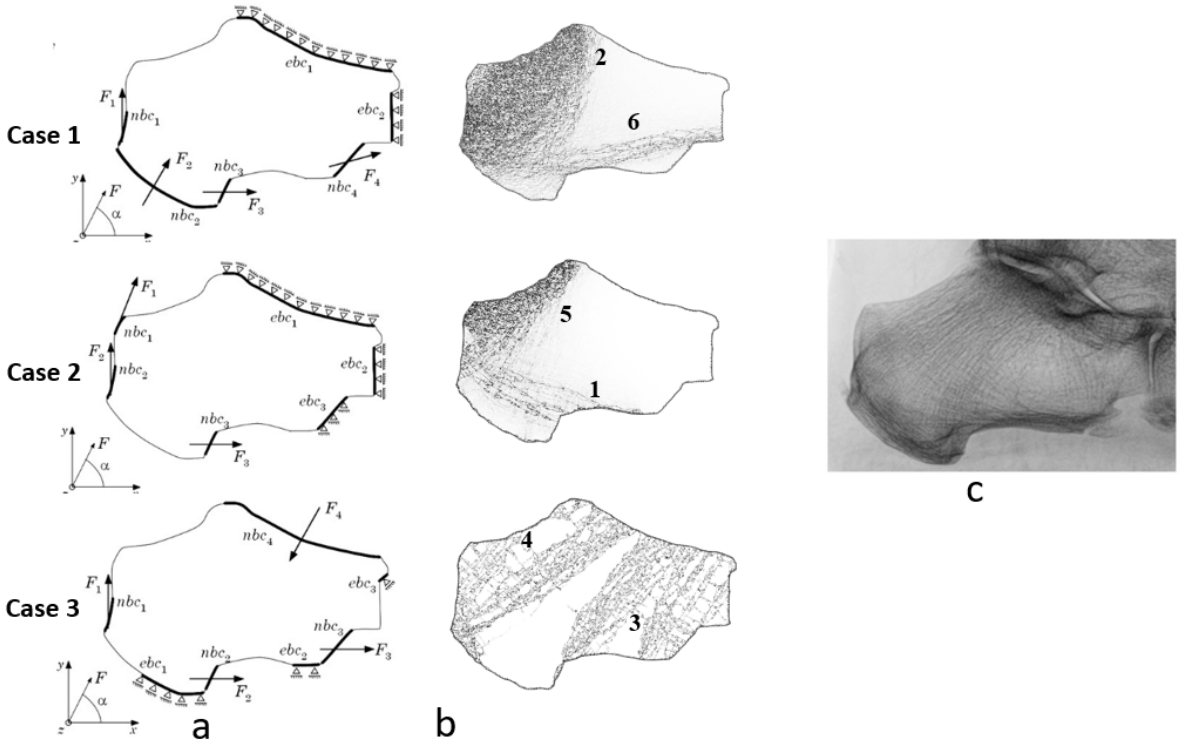

Fig. 35: Results of calcaneus cancellous bone remodeling at 100 days.
(a) boundary conditions used by (Belinha, Natal Jorge, and Dinis 2012). (b) Trabecular patterns obtained with frame elements (c) calcaneus x-ray detail.

Second medical case				
First load case	**F1**	**F2**	**F3**	**F4**
Force magnitude (N)	65	100	20	10
Direction	90°	Normal to surface	0°	5°
Second load case	**F1**	**F2**	**F3**	**F4**
Force magnitude (N)	65	30	25	--
Direction	70°	90°	0°	--
Third load case	**F1**	**F2**	**F3**	**F4**
Force magnitude (N)	65	15	15	100
Direction	90°	0°	0°	Normal to surface

Table 2. Gait cycle, boundary conditions as proposed by (Belinha, Natal Jorge, and Dinis 2012).

3.3.2. Implementation in 3D

As a final part in this chapter, the bone remodelling algorithm was implemented in a 3D domain, following the same general methodology as in the 2D cases, first the algorithm was tested with benchmark tests corresponding to topological optimization classical cases as the cantilever beam shown in Fig. 22 and bone remodelling cases as the one presented in Fig. 30. In the first benchmark test, the distributed load in a cube (Fig. 36), the formation of four columns is appreciated with an increased density, with arcs forming in each face, these results are similar in topology to those obtained by (Walton and Moztarzadeh 2017), allowing to infer as we did in the 2D cases that this methodology can be applied to a medical case in which the bone density equation proposed first by (Nackenhorst 1997) can yield important information on the trabecular patterns formed for a particular set of boundary condition.

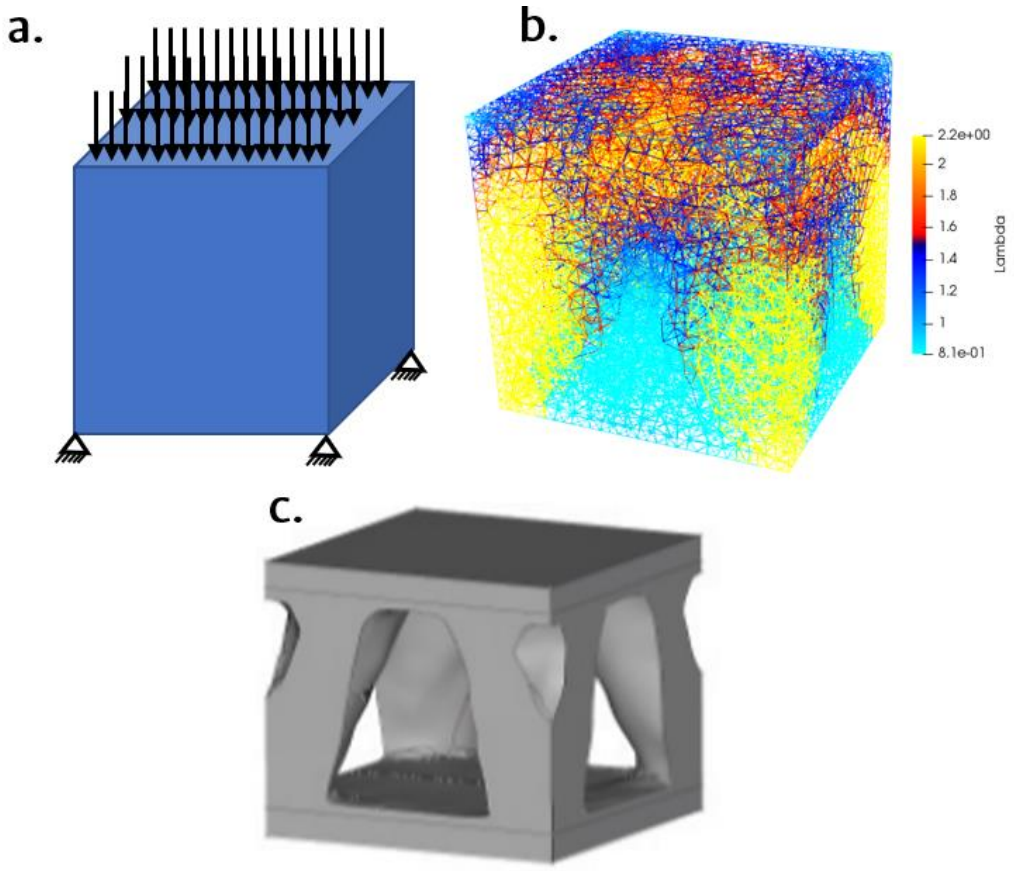

Fig. 36: a. Boundary conditions for the 3D domain. (b) Results in topology optimization for a domain composed of frame elements.(c) Topological optimization results from (Walton and Moztarzadeh 2017)

For this implementation the frame element formulation has twelve degrees of freedom since each node can have three translational displacements (Along the x,y and z axes) and three rotational displacements around each axe (six degrees of freedom per node). The methodology flow chart shown in Fig. 19 was applied to the 3D case as well, the direct formulation and same remodelling equation is used, yet, it is worth mentioning that in this case the strain energy per element takes into account terms due to torsional and additional bending moments because of the three dimensional nature of the problem, for this reason inertia along the Y and Z axis is considered, as well as the polar moment of inertia *J* and torsional modulus *G* as shown in the next equation.

$$U_{strain} = \frac{1}{2}\int_0^L \frac{P_i{}^2}{EA}dx + \frac{1}{2}\int_0^L \frac{M_z{}^2(x)}{EI_y}dx + \frac{1}{2}\int_0^L \frac{M_y{}^2(x)}{EI_z}dx + \frac{1}{2}\int_0^L \frac{T(x)}{GJ}dx \quad \text{Eq. 21}$$

In Fig. 37 the degrees of freedom for the 3D frame element are appreciated, where the superscript corresponds to each node, *u,v, w* are translational displacements along the axis shown, and θ_{xy}, θ_{yz}, and θ_{xz} are the rotational displacements in the specified planes in the subscript.

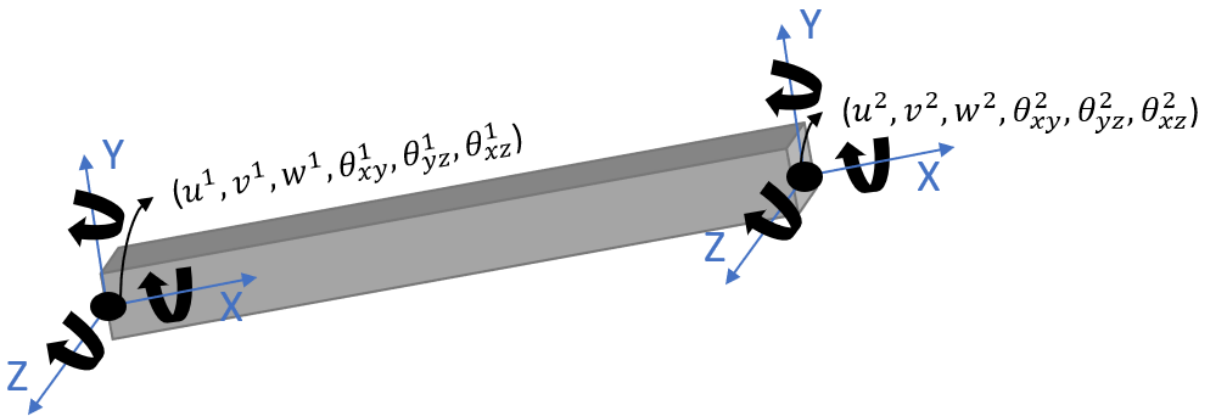

Fig. 37: 3D frame DOFS (degree of freedom)

For the medical case, a 3d model of the femur was discretized into frame elements and subjected to the boundary conditions suggested by (Beaupre and Orr 1990), where an approximated pattern of the main trabecular groups was found. The stl model was meshed in Ansys and the process of discretization used a code in MATLAB to obtain the 1D frame elements. In Fig. 38 the 3D initial bone density is shown along with the bone remodelling results after 100 days, as in the 2D simulations for this medical case. The mesh composed of tetrahedral structures (i.e., the unit cell is a tetrahedron). The properties of each element are the same as in the case of the previous 2D simulations, inertias, area, and average length per element. For these simulations a restriction in density was set for the elements corresponding to the periosteum as in the case of Fig. 31.

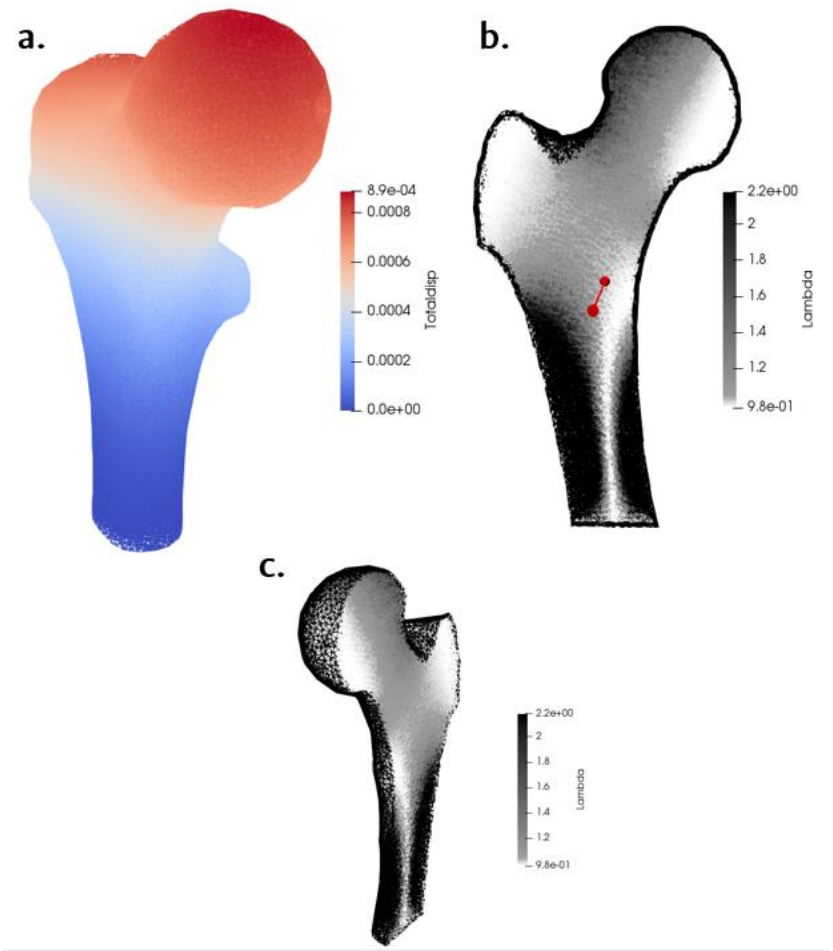

Fig. 38:(a) Total displacement for the loading history proposed by (Beaupre and Orr 1990), . (b) Coronal section of the femur (c) Isometric view with a cut showing coronal section.

Although the distribution obtained for the trabecular groups resembles the patterns found in anatomical samples, there is still a lack in formation of the secondary groups, which may be due to the fact that the loads of (Beaupre and Orr 1990) model better the 2D domain.

3.4. Discussion

In this work, a bone remodeling algorithm, based on the works of (Nackenhorst 1997; Garzón-Alvarado and Linero 2012a) is proposed with a discrete element approach to address the bone remodeling problem. In addition, different aspects such as mesh quality, mesh size and mesh distribution were tested qualitatively to see the influence on the resultant topology.

In the first medical case, a zone with less density called Ward's triangle (in honor to Ward, who first described the internal structure of the proximal femur in 1938) can be seen between the ogival system of the trochanteric plateau and the cervicocephalic support system. This is an important region because cervicotrochanteric fractures originate here in people of advanced age (Martín and Kochen 2011). The calcar, which extends from the posteromedial cortex in the femoral neck to the distal part of the lesser trochanter, is identified with a high bone density in the final topologies. This is an important fact since this region helps to support stems from implants, which need a dense cancellous bone for a proper anchorage; for this reason, numerous fixation methods have been proposed on this zone, see (Cha et al. 2019) and (Peng et al. 2020).

Among the obtained trabecular groups, it is noted that the greater trochanter group (GTM) appears as a less dense zone compared with the other groups. The secondary compressive (GSC) and secondary tensile (GST) groups are visible too: They begin to form in the lateral portion of the shaft and go upward forming an arch that ends in the vicinity of the greater trochanter. As seen in Fig. 33(c) the secondary groups meet at right angles, starting in the proximal section of the shaft, becoming gradually thinner as they approach the surface of the femoral head. These last observations agree well with our simulations as seen in Fig. 33(b). Another key feature found in the simulation is that a high bone density is predominant in zones where there is a greater cortical thickness as seen in Fig. 33(c) and Fig. 31; this helps to maintain the strength and rigidity of the femur as stated by (Marco et al. 2019).

The calcaneus bone is the largest tarsal bone and it is characterized by a cortex containing trabecular bone (Metcalf et al. 2018). Due to the mechanical stresses acting on the calcaneus, a set of trabecular groups are formed and play a crucial role in the biomechanics of this bone. These are important in orthopedic procedures and pathology treatments that compromise bone integrity such as in osteoarthritis therapy. The loading conditions were addressed as bone remodeling problems with the methodology proposed herein. The resulting trabecular groups resemble those seen in the calcaneus bone illustrated in Fig. 35(c). As in the previous medical case, a set of main trabecular groups have been identified as displayed in Fig. 35(b). These are in good agreement with anatomical studies regarding the biomechanics of calcaneus bone (Abboud 2018). The following trabecular motifs can be identified individually for the boundary

conditions of (Belinha, Natal Jorge, and Dinis 2012): thalamic group (1); inferior plantar group (2); anterior apophyseal group (3); anterior plantar group (4); posterior achillean group (5); and central triangular area of refracted bone (6). An aspect that calls attention in some of these groups is the appearance of single lines corresponding to long trabecular groups such as the anterior apophyseal group or the central triangular area of refracted bone; this "thinning" could mean that the particular group does not play a vital structural role for that specific case load.

Having discussed the medical cases, it can be stated that this method may be used as an alternative to continuous domains due to its inexpensive computational cost as stated by (van Lenthe and Müller 2006) where even a 1000-fold reduction in processing time can be achieved by using frame elements, thus allowing to increase both the sample size and the complexity of the trabecular structure to analyze multiple loading configurations (Ruff1. Ruffoni, D. & Van Lenthe, G. H. 3.10 Finite element analysis in bone research: A computational method relating structure to mechanical function. Comprehensive Biomaterials II vol. 3 (Elsevier Ltd., 2017).oni and Van Lenthe 2017). A comparison in speed of the continuum and the proposed discrete methodology was briefly addressed as seen in Fig. 30(b) and Fig. 30(c): an improvement of more than 20% wall-clock time was achieved. Furthermore, it was found that the new bone remodeling approach using discrete structures have shown great potential.

A high level of mesh structuration leads to results quite similar to those obtained in TO. However, the simulations obtained with the medical cases which resemble the most to trabecular bone were those with non-structured meshes. This can be in part due to the fact that trabecular bone has been more accurately modeled with non-structured meshes (Luxner et al. 2009). This also agrees with the hypothesis given by (Weinans, Huiskes, and Grootenboer 1992) that trabecular bone is chaotically ordered and can be considered as a fractal since the best results were obtained with a triangular non-structured mesh.

Looking at the bone remodeling algorithm proposed, it is seen that the rule applied to each element is an objective function for an optimization process, relative to an external load. This function follows a preset value for the energy strain density; thus, it is expected that the energy strain, as well as the stresses, are more uniformly distributed as the steps increase. In this sense it can be said that this method uses a bio-inspired topology optimization.

3.5. Additional applications

As a proof of concept, some results from the bone remodelling algorithm were manufactured using a digital light processing (DLP) 3d printer. In Fig. 39(a) and Fig. 39(b) the trabeculae groups obtained are shown, whereas in Fig. 39(c) the topology obtained by the bone remodelling algorithm for the cantilever beam shown in Fig. 28 (Frame elements) is demonstrated. This shows that the bone remodelling algorithm may be used to optimize infill patterns to be used in additive manufacturing. (Wu, Wang, and Gao 2019) presented a method to design lattice structures that are optimized to the principal stresses, and also uses an algorithm to ensure geometrical consistency so the lattice model can be 3d printed. A bone remodelling algorithm that optimizes a lattice structure and allowing to be printed like those in figure Fig. 39 may have the advantage of reduced computational cost, given the use of 1D finite elements and a direct formulation in the finite element method.

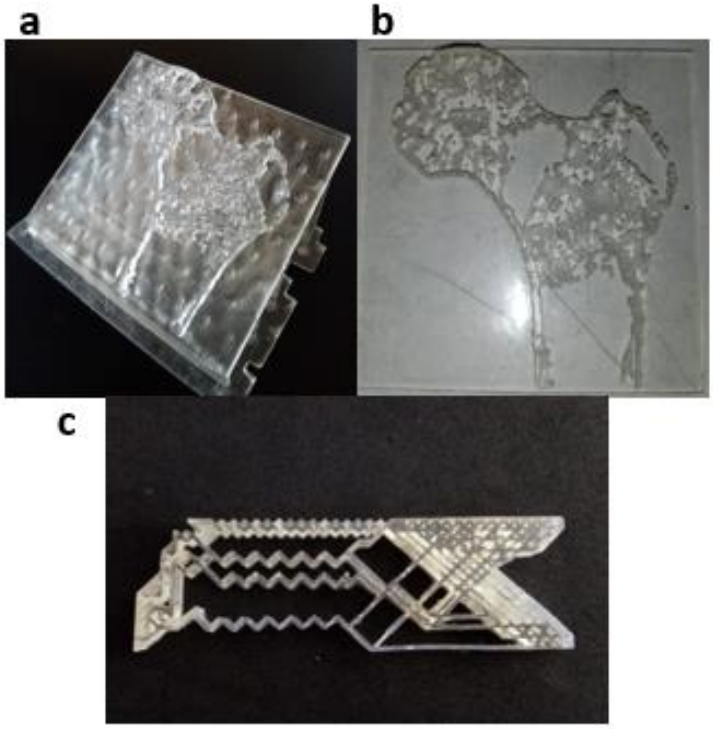

Fig. 39: Additional application for the bone remodelling algorithm using discrete structures, bio-inspired infill pattern, resin 3d prints.

The prints were obtained by converting the images from the bone remodelling results to gray scale, then by converting this data to vector image and extruding high contrast zones, using the

software 2D Image to STL Converter (Windows) featured in thingiverse by the user BloodBight. Then as slicer, the software CHITUBOX © was used.

3.6. Conclusions

The results show the self-enhancing process in which denser bone attracts more strain energy after each iteration, resulting in an even denser bone. This methodology when applied to the medical cases has proven to be a valid approach given the similarity with previous works (Garzón-Alvarado and Linero 2012b; Valdez et al. 2017) and the anatomical features found in literature (Martín and Kochen 2011; Marco et al. 2019).

As first stated by (van Lenthe and Müller 2006) the use of beam-like elements properly predicts the anatomical distribution of trabecular groups. A modelling approach using both beam elements for rod-like trabeculae and shell elements for plate-like structures, characteristic in cancellous bone, may be used to improve this methodology. Regarding the limitations of the proposed methodology, one is that frame-based models alone fail to represent the plate-like networks, especially in certain areas where plate structures are predominant in cancellous bone; so, this approach is applicable only to model mechanics of trabecular bone. In cortical bone, a precise model would need to be coupled with continuous elements to improve representation. This loss in precision to represent bone architecture is compensated with a gain in model simplification and solution time that could be used to look into nonlinear problems, typical in bone remodeling, or with several spatial scales. Another shortcoming of this approach, when dealing with medical cases, is that the initial domains are generated randomly in a manner that attempts to mimic cancellous bone, but not with a specific-patient domain. In further works, a more clinical accurate domain may be obtained from a specific portion of cancellous bone retrieved from a CT scan to evaluate bone remodeling in a specific loading case, this 3D simulation will benefit from the improvements in speed and simplicity from this methodology.

The work in chapters two and three may be used by design engineers as a method to generate a concept design for biomaterial engineering applications since trabecular bone is a natural material that excels for its low weight and high mechanical performance (Ruff1. Ruffoni, D. & Van

Lenthe, G. H. 3.10 Finite element analysis in bone research: A computational method relating structure to mechanical function. Comprehensive Biomaterials II vol. 3). It could also be used too by medical researchers who are interested in the bone remodeling dynamics and the mechanical properties of cancellous bone with applications in bone grafts and implants. Furthermore, by understanding the topological optimization of bone remodeling, engineers should be inspired by these natural smart designs for developing sustainable and useful technologies.

Finally, in the last part of this thesis, based on the model of (Komarova et al. 2003) and (Nackenhorst 1997), both being relevant works in the field of bone remodelling, the coupling of mechanical field variables and biological variables will be explored by means of the discrete modelling approach in order to relate variables such as strain energy in the BMU and the dynamic variations in cell populations of osteoblasts and osteoclasts by the incidence of different paracrine and autocrine factors that are inhibited by the mechanical stimulus perceived in the osteocyte mechanosensory system. This final chapter can be used as a base for researchers to look into the relation between two type of models that not up until recently have been integrated, but this time using the discrete modelling approach.

4. Unified framework of cell population dynamics and mechanical stimulus using a discrete approach in bone remodelling

4.1. Introduction

Among the different approaches to study bone remodelling from a mathematical point of view, the use of bone cell population models has its main application in the study of different biological factors at play in the biophysical activities of osteoblasts and osteoclast (Hambli 2014). Some of these models have already been reviewed in chapter one under the section of mathematical models. This modeling endeavor has its motivation in the need for more insight on the imbalances in biological factors in diseases like osteoporosis, osteopetrosis, among others, where a quantitative understanding in biological cell dynamics could be used to better design pharmaceutical and physiotherapeutic treatments.

There are various classical works on bone population dynamics, one of the most famous is the one of (Komarova et al. 2003), which is important in this chapter. This model relates the population of osteoblast and osteoclast with bone mass density (BMD) at the basic multicellular unit (BMU) in accordance to histomorphometry data of bone sections (Parfitt 1994). This model became of interest to the scientific community because it takes into account paracrine and autocrine regulators of the bone remodelling process such as TGF- β, RANKL, and others, that are important in treatments where there are imbalances between formation and resorption rate. Furthermore, the dynamic behavior accurately predicts the remodelling cycles for different pathological cases in good agreement with clinical literature. All this is achieved by the coupling of three non-linear differential equations that relate the population of osteoblasts (x_2), osteoclasts (x_1) and bone density. These populations follow a power law approximation for the growth rates of osteoblast and osteoclast as it is seen in Eq. 22 and Eq. 23 .The effects of the different factors influencing the bone remodelling process (PTH, TGF- β, RANKL, among others) are taken into account by the constants g_{ii}. Finally, these cell populations determine the amount of bone mass density in percentage (z in Eq. 25), being 100% the steady state level of bone density which is in average 0.98 g/cm^2 in young adults (Key 2020) for the femoral head.

The type of influence on the principal regulating factors of the bone remodelling process is shown in Table 3, where the first subscript corresponds where the regulating factor is originated, 1 for osteoclast and 2 for osteoblasts.

$$\frac{dx_1}{dt} = \alpha_1 x_1^{g_{11}} x_2^{g_{21}} - \beta_1 x_1 \quad \text{Eq. 22}$$

$$\frac{dx_2}{dt} = \alpha_2 x_1^{g_{12}} x_2^{g_{22}} - \beta_2 x_2 \quad \text{Eq. 23}$$

$$y_i = \begin{cases} x_i - \overline{x_i} & ssi\ x_i > \overline{x_i} \\ 0 & ssi\ x_i \leq \overline{x_i} \end{cases} \quad \text{Eq. 24}$$

$$\frac{dz}{dt} = -k_1 y_1 + k_2 y_2 \quad \text{Eq. 25}$$

Signaling type	**Regulating factors**	g_{ij}
Autocrine (Osteoclasts)	RANKL, TGF- β,	g_{11}
Paracrine (osteoclast to Osteoblast)	TGF- β, IGF	g_{12}
Paracrine (osteoblast to Osteoclast)	PTH, OPG, RANKL, vitamin D3	g_{21}
Autocrine (osteoblast)	IGF	g_{22}

Table 3: Factors g_{ij} influence on (Komarova et al. 2003) models.

Previous stability and sensitivity analysis have been made on the model of (Komarova et al. 2003) e.g. (Jerez and Chen 2015) and (Fonseca-vel 2009). These works show that stability is assured for a rather narrow set of initial conditions and parameters, the non-linear analysis yields various type of responses, stable regulated oscillatory, single response, and unstable oscillations. The sensibility analysis can be performed varying each parameter and revising the time response using functional blocks as in the case of (Fonseca-vel 2009) or analytically .

Another famous model is that of (Pivonka et al. 2008) which in addition to the cell populations addressed by (Komarova et al. 2003), includes the population of precursors of osteoblasts and osteoclasts and incorporates the RANK-RANKL-OPG signaling pathway with the influence of TGF-

β on bone cells. This work is built up on the model of (Lemaire et al. 2004) with a few additional features, it adds a rate equation for the change in bone volume depending on time, in addition, a rate release equation for TGF- β in the bone matrix with the inclusion of the expression of OPG and Rankl on osteoblastic cell lines.

More recently, models with increased complexity have been proposed, elaborating on classical works such as the one of Komarova, for example (Jerez and Chen 2015) added a term functioning as external regulator of the bone remodelling process, furthermore conditions for the existence of positive periodic simulations according to those found experimentally are derived analytically. (Hambli et al. 2016) developed a model which links pharmacokinetic and mechanical dynamics to predict the action of denosumab (monoclonal antibody) in bone remodelling by coupling the model of (Komarova et al. 2003) with a mechanic model which takes into account fatigue damage (J. Li et al. 2007), this model is able to predict bone formation as well the influence of denosumab in the bone mass density over time.

In this chapter we present a model which relates a classical population model such as the one proposed by (Komarova et al. 2003) and the one by (Nackenhorst 1997) which has a mechanical focus, both classical papers in the field. This new model, could help researchers visualize how the bone remodelling process periodicity response relates to a mechanical stimulus in trabecular bone and how it affects the formation of the main trabecular groups, to this purpose the femur medical case that was previously addressed in chapter three will be analyzed. The model also has the novelty of coupling two robust models and the additional benefits of using the discrete modelling approach, improving on computational speed as it was seen as well in the previous chapter.

4.2. Methods

In this section, the model of (Komarova et al. 2003) will be described with a few additions proposed in order to couple it with the model of (Nackenhorst 1997) that will also be revised, the methodology is presented as a flow chart in Fig. 40.

4.2.1. Model description

The proposed model in this chapter is shown in Fig. 40, for this new model, a discretized modelling approach is followed as in the previous chapter. In this case, frame elements will be used as well (displacement and rotations at each node) to model each trabeculae mechanical behavior and the cell population variation at each bone multicellular unit (BMU).The same boundary conditions as before will be applied to the femur of (Beaupre and Orr 1990) as well as the trabeculae properties such as inertia, length, and area (Cesar et al. 2013). In Eq. 26, the term added to (Nackenhorst 1997) changes the elastic modulus accordingly to the relation between osteoblasts and osteoclast at the BMU following a power law as in the unchanged model with *m* =2 . k_3 is a normalization constant that scales the density obtained by Nackenhorst to be added at the bone mass density proposed by Komarova. Constant k_4 is also a normalization factor for the relation between osteoblasts and osteoclasts. These constants were selected to fit the behavior from the bone remodelling response at different cases, such as stable bone periodic response, unstable formation (osteopetrosis), unstable absorption (osteoporosis) and simulating the action of a pharmaceutical agent, affecting bone formation.

$$E_{t+1} = E_t(\lambda^n + k_5\left(\frac{X_2}{X_1}\right)^m) \quad \text{Eq. 26}$$

$$\gamma_1 = 0{,}99 + \lambda \,/\, 21{,}55 \quad \text{Eq. 27}$$

$$\gamma_2 = 0{,}89 + \lambda \,/\, 21{,}55 \quad \text{Eq. 28}$$

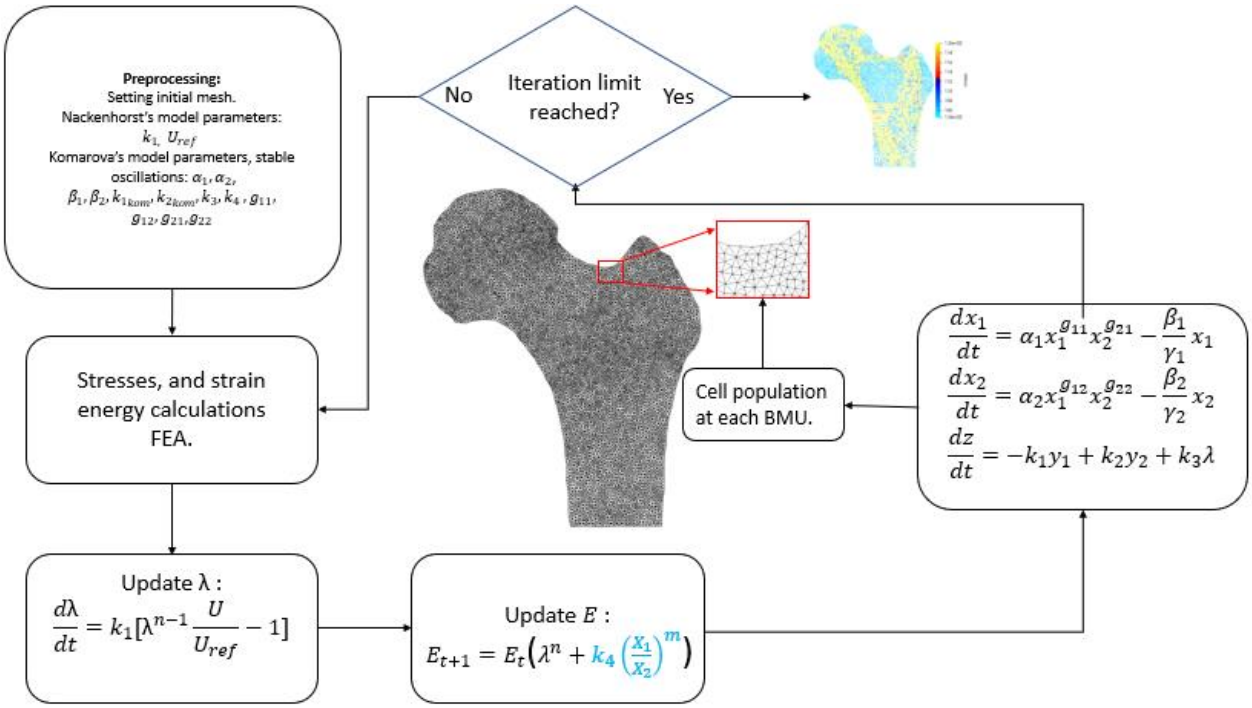

Fig. 40 Flow chart of new model coupling bone remodelling model from (Komarova et al. 2003) and (Nackenhorst 1997) with the addition of coupling terms.

In Fig. 41 a comparison between the two models coupled is shown with the additional terms proposed in this work, the linking terms correspond to the dimensionless bone mass density lambda $(\lambda), \gamma_1, \gamma_2$ and the term $\left(\frac{X_2}{X_1}\right)^m$ in the equation which updates the elastic modulus (see Eq. 26)

Komarova (2003)	Nackenhorst (1997)
$\frac{dx_1}{dt} = \alpha_1 x_1^{g_{11}} x_2^{g_{21}} - \frac{\beta_1}{\gamma_1} x_1$ $\frac{dx_2}{dt} = \alpha_2 x_1^{g_{12}} x_2^{g_{22}} - \frac{\beta_2}{\gamma_2} x_2$ $y_i = \begin{cases} x_i - \bar{x_i} & ssi\ x_i > \bar{x_i} \\ 0 & ssi\ x_i \leq \bar{x_i} \end{cases}$ $\frac{dz}{dt} = -k_1 y_1 + k_2 y_2 + k_3 \lambda$ $\gamma_1 = 0{,}99 + \lambda\ /\ 21{,}55$ $\gamma_2 = 0{,}89 + \lambda\ /\ 21{,}55$	$\frac{d\lambda}{dt} = k_1 \left[\lambda^{n-1} \frac{U}{U_{ref}} - 1\right]$ $E_{t+1} = E_t(\lambda^n + k_5 (\frac{X_1}{X_2})^m)$

Fig. 41: Equations from the models from (Komarova et al. 2003) and (Nackenhorst 1997) with terms added in this new model.

The terms γ_1 and $\gamma_2$were fitted in order to maintain a stable response in the system of ordinary differential equations and depend on the dimensionless density calculated following the Nackenhorst model, these terms modify the rate at which the population of osteoblast and osteoclast changes without taking the system out of equilibrium.

4.2.2. Numerical implementation

As stated before, we coupled two classical bone remodelling models into one. As seen in Fig. 41, the new model is described by two groups of differential equations. The system of differential equations from the model of Komarova was solved using the Runge-Kutta fourth-order (RK4) which is based on a Taylor's series expansion. For each differential equation (osteoclasts, the following scheme was followed:

$$x_i{}^{t+1} = x_i{}^{t} + \frac{\Delta t}{6}[f_1 + 2f_2 + 2f_3 + f_4] \qquad \text{Eq. 29}$$

$$f_1 = f(x, t_k, x_i{}^{t})$$

$$f_2 = f(x, t_k + \tfrac{\Delta t}{2}, \lambda_k + \tfrac{\Delta t}{2} f_1)$$

$$f_3 = f(x, t_k + \tfrac{\Delta t}{2}, \lambda_k + \tfrac{\Delta t}{2} f_2)$$

$$f_4 = f(x, t_k + \frac{\Delta t}{2}, \lambda_k + \frac{\Delta t}{2} f_3)$$

So, the population of osteoclasts (x_1), osteoblasts (x_2) and mass percentage (z) is determined at each step Δt ,in addition with the energy strain at each element and dimensionless density λ for each element. To solve the finite element equations for the frame elements and the system of ODES a user subroutine was programmed and attached to ABAQUS, the UEL solver was used. As stated before Euler method was used to solve the bone density evolution (λ) whereas Runge-Kutta fourth-order was programmed to solve the system of ODES corresponding to cell populations (see Eq. 22). A time step of 0.1 days was set as in the previous chapter.

4.3. Results

In this section some conditions for bone remodelling are considered to test the model proposed, among them, we consider the normal bone remodelling cycle (no net gain or loss in bone turnover) with the time evolution given some initial conditions (see Table 4),pathologies like osteoporosis where there is a decrease in bone mass density, osteopetrosis, where an increased density is found in trabecular bone, finally, a case where a pharmaceutical agent has been administered, affecting bone remodelling regulators like IGF.

4.3.1. Normal bone remodelling cycle

In figure Fig. 42 the variation in cell population for osteoblasts and osteoclasts can be seen according to the model of (Komarova et al. 2003), there is an equilibrium between formation and absorption, resulting in no net bone mass addition in the BMU. In Fig. 43 the bone mass density variation is shown for the same case, in addition, the system stability can be seen in the phase portrait where only one orbital is seen. The parameters from the model in this particular case are shown in Table 4.

Parameters	Stable oscillations
x_1(at time 0)	11.0607
x_2 (at time 0)	212.1320
α_1	3 cells day^{-1}
α_2	4 day^{-1}
β_1	0.2 day^{-1}
β_2	0.02 day^{-1}
k_1	0.093 % cell^{-1} day^{-1}
k_2	0.008% cell^{-1} day^{-1}
k_3	0.001% cell^{-1} day^{-1}
k_4	4.439e-4
g_{11}	1.1
g_{12}	1.0
g_{21}	-0.5
g_{22}	0.0

Table 4: Parameters used in the normal bone remodelling cycle.

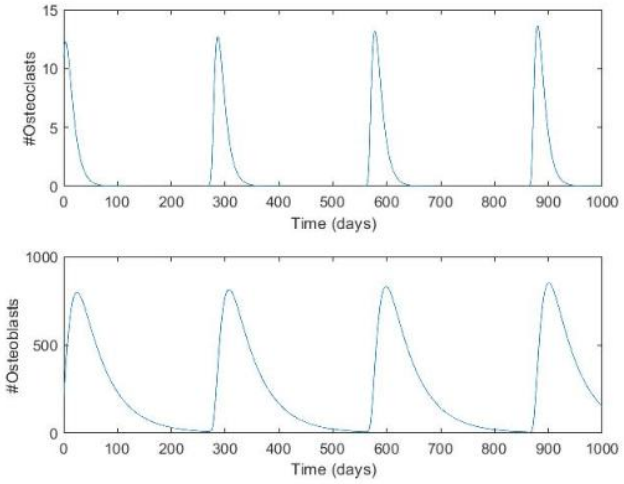

Fig. 42: Osteoclast and osteoblast population at the BMU

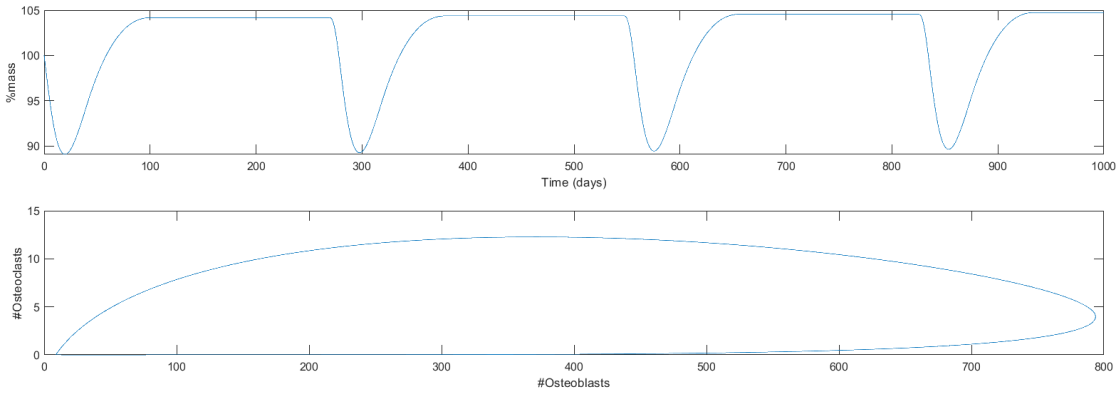

Fig. 43: Bone mass percentage at the BMU (top) and phase portrait (bottom) of osteoblast and osteoclast dynamic.

The bone remodelling cycle with periodical stable oscillations is shown in Fig. 44, this process starts asynchronously thorough the domain, as can be seen in day 1, only few elements start the remodelling process. After day one, more elements initiate the process, and at day ten, there is a heterogenous bone density due to the fact that each element is at a different stage of the bone remodelling cycle, but even though each BMU follows a different part of the cycle, a noted increment along the main trabecular groups starts to notice in the following weeks. After day 50, these patterns are quite visible. When the trabecular groups have been formed, the overall bone mass density distribution fluctuates due to the periodic oscillations, yet, these patterns conserve an increased density in comparison with its surroundings. It is worth noting that the main trabecular groups still have a periodic response but the average value is greater than elements

with a lower energy strain. The higher density is found at 300 days with a percentage of 140% which would be about 1.372 g/cm^2.

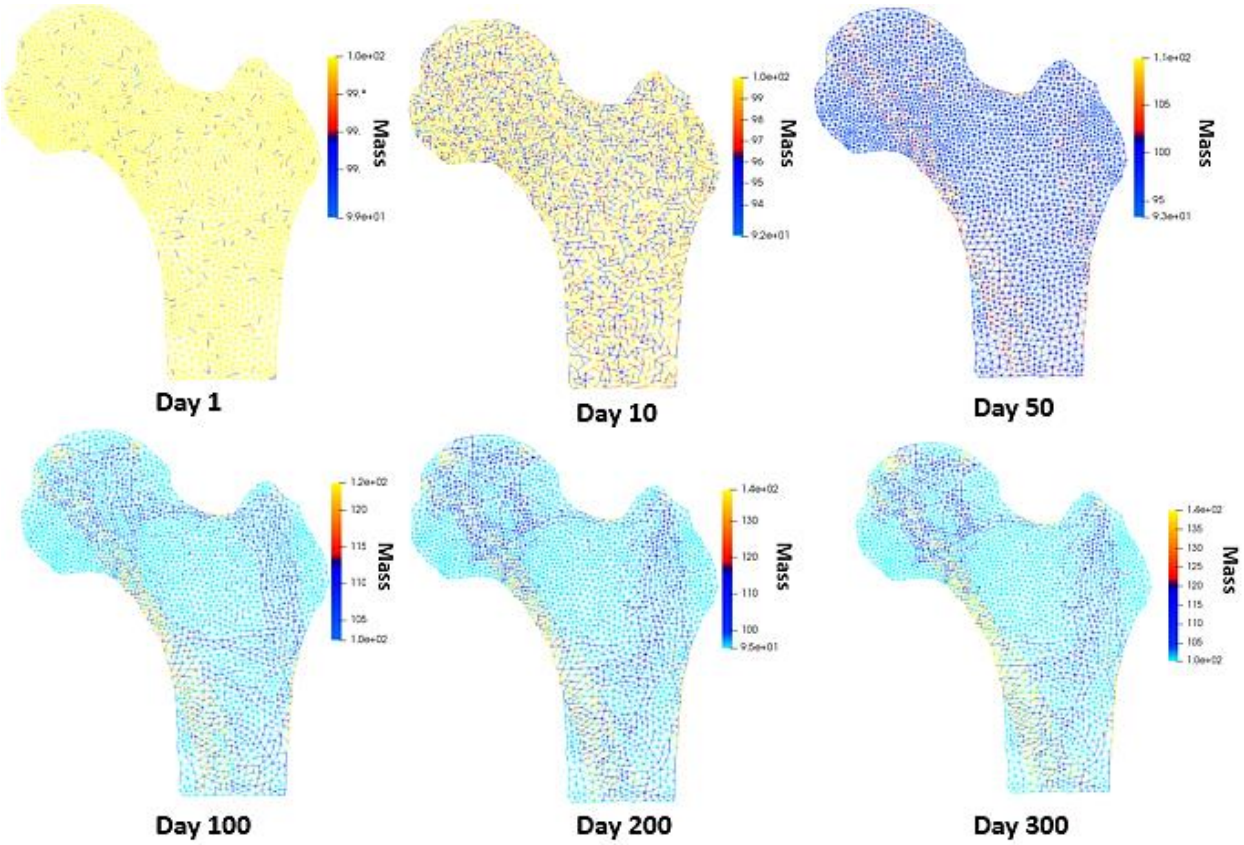

Fig. 44: Bone mass density evolution, asynchronous bone remodelling occurring at each BMU and conserving mass along main trabecular paths (normal bone remodelling).

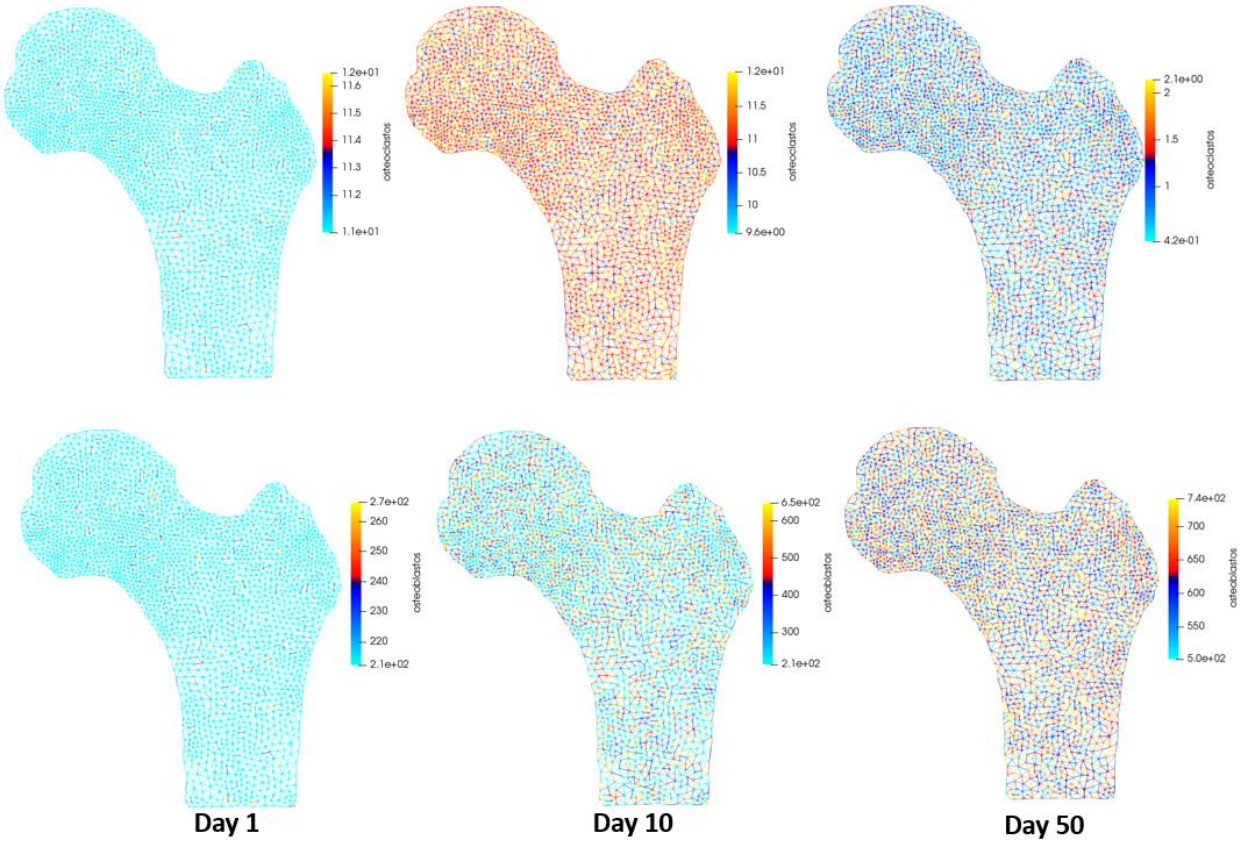

Fig. 45: Bone remodelling asynchronous variation in each element for osteoclast (top) and osteoblast (bottom).

4.3.2. Osteoporosis

In this pathology an overall loss in bone mass density is suffered in trabecular bone, as seen in Fig. 46, the bone loss reaches 90% in the low energy strain zones, at 50 days there is a loss of more than 30% in density compared to the normal case. This simulation was carried out with the factor $g_{12} = 0.9$ (10% less than in the normal case). The remodelling cycle has the same period as in the previous case but the oscillations are not stable anymore, as shown in Fig. 46.

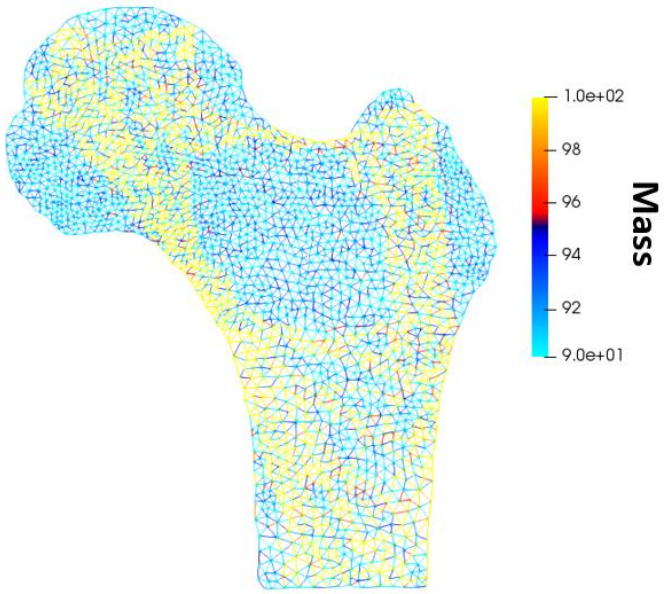

Fig. 46: Decreased overall density due to the action of IGF (decreased factor g_{12}) at 50 days.

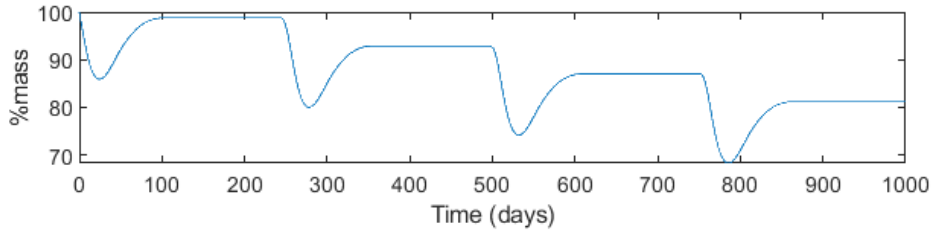

Fig. 47: Unstable oscillations, example of osteoporosis.

For an average BMU in the domain there is an ongoing loss in density as depicted in Fig. 47, in 1000 days the density suffers a loss of almost 20%. It is worth noting, that although the main trabecular groups remain visible and attract denser bone, these groups possess a density lower when compared with the previous case.

4.3.3. Osteopetrosis

Fig. 48 shows an increased density all over the domain that goes up to three times the normal density of bone (3.117 g/cm^2) at 100 days. In this particular case factor g_{22} was set to 0.1, meaning that the autocrine regulation of IGF was considered within the BMU.

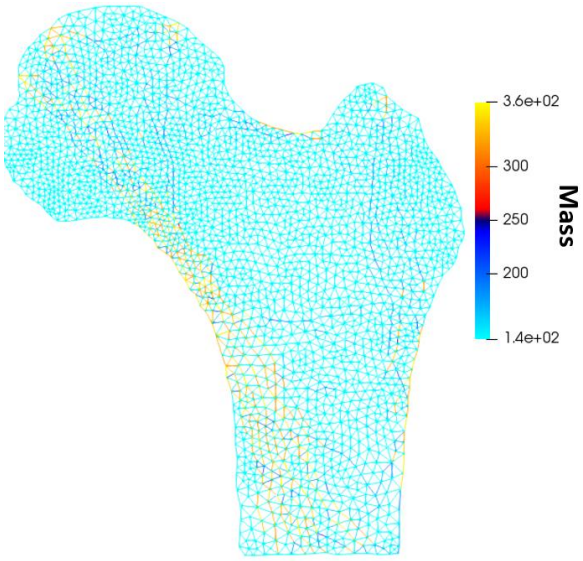

Fig. 48: Increased overall density due to the action of IGF (increased factor g_{22}) at 100 days.

4.3.4. Pharmaceutical agent action

For this particular case we simulated a pharmaceutical agent that increases the factor g_{11} which affects the action of RANKL and TGF- β. In this simulation, g_{11} was increased by 1.8% at 700 days over a period of 50 days resulting in the populations seen in Fig. 49. An increase in the population of osteoblasts and osteoclasts is appreciated, which is reflected in the bone mass density as seen in Fig. 50 with the presence of unstable oscillations that tend to increase the mark of 100% mass.

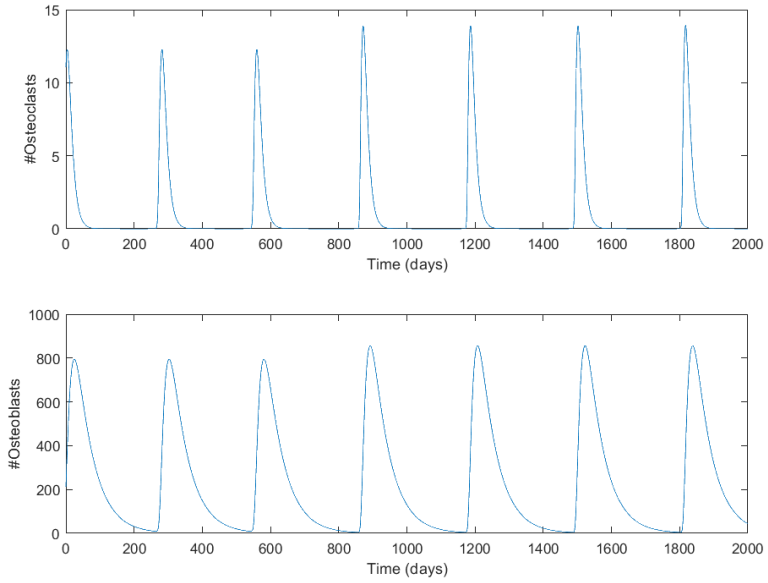

Fig. 49: Osteoclast and osteoblast population at the BMU with the action of a pharmaceutical agent influencing RANKL or TGF- β at 700 days.

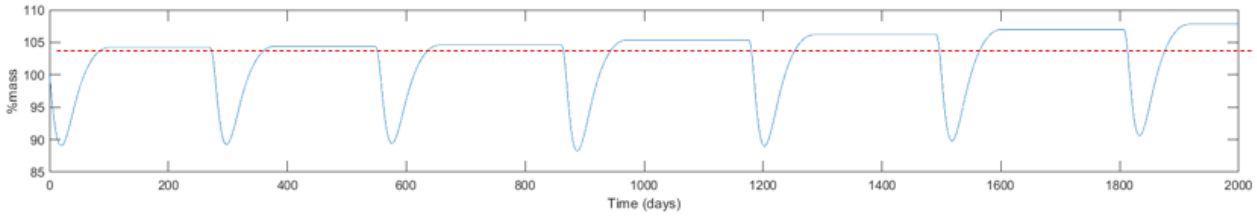

Fig. 50: Bone mass percentage at the BMU with the action of a pharmaceutical agent influencing RANKL or TGF- β.

Additionally, a simulation with the factor $\beta_1 = 0.23$ was carried out to test a case shown in the paper of (Komarova et al. 2003) that yields an increase in bone formation, in this case the highest density value was 150%, which is 1.47g/cm^2 according to (Cesar et al. 2013).

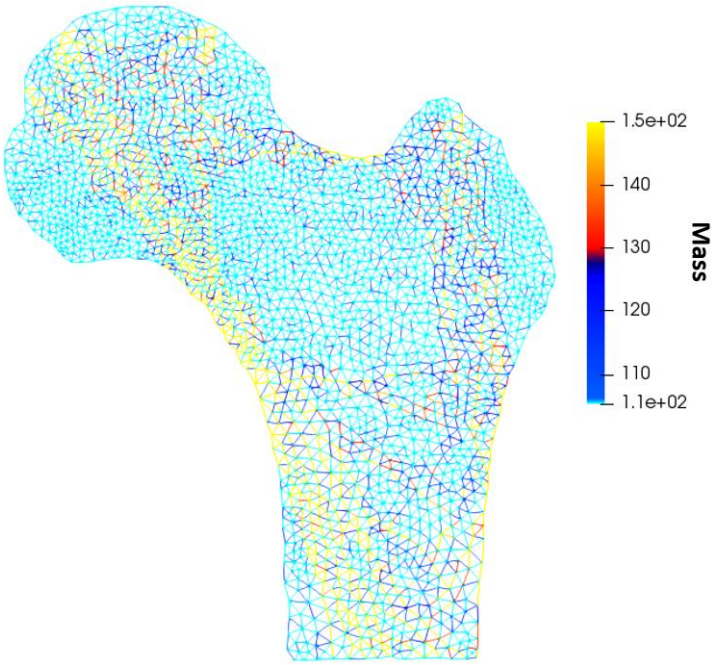

Fig. 51: Increased density due to pharmaceutical agent, $\beta_1 = 0.23$.

4.4. Discussion and conclusions

In this paper, a bone remodelling model based on the works of (Nackenhorst 1997; Garzón-Alvarado and Linero 2012a) and (Komarova et al. 2003) is proposed using the discrete element

approach to address the bone remodelling problem in such a way that mechanical and biological factors are taken into account. Some cases of bone remodelling are addressed, such as normal bone remodelling with no change in bone turnover and other scenarios such as pathologies like osteoporosis and osteopetrosis. Finally, the action of some pharmaceutical agents is investigated based on the model proposed.

In Fig. 44 the normal bone remodeling case results show great similarity with others works in bone remodelling, see for example (Hambli et al. 2016) and (Peyroteo et al. 2019) after the system has reached a steady state (marginally stable due to the oscillations from Komarova's model) , this oscillations are asynchronous as seen in Fig. 45.Furthermore the main trabecular groups and low density zones such as the ward's triangle can be seen to some extent. In both pathological cases these structural patterns are identified as well. Overall, the structural patterns have great similarity with those found in the previous chapter.

In the pathological cases, a good correlation with literature on the role of different regulating factors was achieved. For the osteoporotic case, factor g_{12} was reduced to 0.9, resulting in a decrement for the overall bone mass density in the domain, yet the trabecular groups still are notable, for lower values the density drops drastically and the periodic response becomes unstable. In case of osteopetrosis, an increased in g_{22} corresponds to the action of IGF as autocrine regulator for osteoblasts, which ends up in a higher bone mass density as stated by (Niu and Rosen 2005), the increased proportion was triple along the trabecular groups.

As a final study case, the action of a pharmaceutical agent was simulated with an increase in factor g_{11} of 1.8%, meaning a positive inhibition in RANKL and TGF- β. This results in increased populations of osteoblasts and osteoclasts with an increase in formation as seen in Fig. 50. This impulse was maintained over an interval of 50 days, then g_{11} returned to the value of normal bone remodelling oscillations stated in Table 4. It is worth noting that over a period of 2000 days the system did not returned to the previous state, the higher peaks remained over 14 cells in case of osteoclasts and 850 cells for osteoblasts, whereas in the normal case were of 12 osteoclasts and 800 osteoblasts. Next simulation addressed a case where osteoclast recruiting is inhibited, in order to model this inhibition factor β_1 was set to 0.23 and the simulations show an increase in BMD which is expected since osteoclast activity is reduced.

Regarding some of the limitations of this new model we can see that each BMU has been approximated to a full element or trabeculae, we know that in reality a basic multicellular unit has a diameter of roughly 200μm, so we have simplified the BMU into one element that has a length in average of 800μm and 254μm as in the previous chapter according to (Cesar et al. 2013), this approximation should still capture the mechanical response that occurs in trabecular bone. Another simplification which comes from the model proposed by Komarova is that each BMU is independent from each other, so the regulating factors act only within the same BMU. In addition, the parameters set for the normal bone remodelling cycle were adapted from (Komarova et al. 2003) and correspond to those a young adult.

Despite the simplifications addressed, this bone remodelling model is able to replicate the trabecular structures accordingly with anatomical literature and the behavior in the system after tweaking some factors representing regulators in bone remodelling, which end up in pathological cases such as osteoporosis or osteopetrosis.

The results show the new model can relate the mechanical field variables such as energy strain with the bone mass density at a specific location in the domain, and the cell population dynamics in various cases: Normal bone remodelling with periodic stable oscillations, osteoporosis, osteopetrosis and the action of a pharmaceutical agent. This work sets the ground for a future work, where more complex cases can be addressed, such as load frequency, dose frequency of a pharmaceutical agent and pathological cases in which regulating factors vary.

Furthermore, the discrete modelling approach has proven to be effective in more complex models and corroborated on the fact that topology of bone can be approximated to discrete structures in order to simplify some bone remodeling problems yielding promising results. In the future, a more complex model can be implemented that uses both discrete and continuum elements to better model the mechanical behavior of trabecular and compact bone.

Finally, some general conclusions from this thesis are presented in the next chapter with additional recommendations and future work.

5. General conclusions and recommendations

5.1. General conclusions

In this work, a new, discrete based methodology has been proposed, in order to model different aspects of the bone remodelling phenomenon, such as the mechanics involved (mechanical stimulus, such as strain energy) and how they affect the turnover rate at a discrete site in a domain.

In the first chapter of this work, various biological aspects of the bone remodelling process are reviewed and the concept of discrete modelling is introduced as a possible approach to different problems in cellular materials and in fields such as additive manufacturing, various mathematical models are introduced to show an overview of the current state the art of mathematical moedelling of bone remodelling. In the second chapter, the discrete FE modelling approach is applied to an optimized cellular like material obtained employing additive manufacturing. The results obtained in the simulations for the displacement fields show error around 30% in comparison to those obtained experimentally, nonetheless the FE simulations showed the overall trend in behavior for the maximum displacement in all tessellations (maximum displacements magnitude from the largest to the smallest: Triangular, Delaunay, Voronoi), which could imply that the source of error lies in 3d printed defects such as clogged pores. As a future work, the implementation of the Timoshenko beam is proposed to check if this would yield better results, especially for short trabeculae.

In third chapter, the discrete modelling approach was implemented specially for the solution of a bone remodelling problem, where first, it was validated on different benchmark tests taken from previous topology optimization and bone remodelling works, then this methodology was applied in two study cases. This new approach allows for the correlation of mechanical and biological variables in a simpler and more efficient way, as it was found, given certain load condition in a cancellous bone, the algorithm predicts the formation of trabecular groups depending on the energy strain field in the particular cancellous bone, using as biological input the strain energy threshold at which remodelling occurs.

This accomplishes the initial objective of building a discrete mathematical model that couples constituent laws of both mechanical and biological nature in order to gain insight on possible correlations, in this particular case, the correlation between energy density and bone formation.

5.2. Products

As part of this work, there is one paper in process of publication (GCMB-2021-0082) in the journal of Computer Methods in Biomechanics and Biomedical Engineering titled: a simple and effective 1D-element discrete-based method for computational bone remodeling, which proposes a new method for addressing bone remodelling phenomenon, with the advantages that have been previously mentioned, this paper corresponds to chapter 3.

Chapter four is in its first round of peer review as well with a paper titled: Unified framework of cell population dynamics and mechanical stimulus using a discrete approach in bone remodelling.

5.3. Future work

The different chapters presented in this work, give a conceptual base and understanding for diving deeper into certain applications and further research such as:

- Test whether a direct formulation using Timoshenko's beam theory is useful to model cellular materials, such as bone.
- Applying the bone remodelling discrete approach to a more complex bone remodelling model, such as the model of(Pivonka et al. 2008), examining as well, aspects such as load frequency, and pharmacokinetics, allowing for a multi-scale model of the bone remodelling process.
- Examine as conceptual designs, the different results in topology for engineering applications, given different unit cells in the domain, for different applications, such as topological optimization in structural design.
- The resultant topologies obtained with the bone remodelling algorithm in chapter 3 could be used in the field of additive manufacturing as infill for a part, where the resultant topology is obtained specifically for the part mechanical needs. A specific software could be developed for this purpose, this will streamline the process of design optimization in

industry. The bone density equation proposed in chapter three with the discrete approach shows great application given its low computational cost.

6. REFERENCES

Abboud, Fraser Harrold;Rami. 2018. “Biomechanics of the Foot and Ankle.” *Orthopaedic Knowledge Update: Foot and Ankle 5*, 3–12.

Andreassen, Erik, Anders Clausen, Mattias Schevenels, Boyan S. Lazarov, and Ole Sigmund. 2011. “Efficient Topology Optimization in MATLAB Using 88 Lines of Code.” *Structural and Multidisciplinary Optimization* 43 (1): 1–16. https://doi.org/10.1007/s00158-010-0594-7.

Annicchiarico, W., G. Martinez, and M. Cerrolaza. 2007. “Boundary Elements and β-Spline Surface Modeling for Medical Applications.” *Applied Mathematical Modelling* 31 (2): 194–208. https://doi.org/10.1016/j.apm.2005.08.021.

Bahia, M. T., M. B. Hecke, E. G.F. Mercuri, and M. M. Pinheiro. 2020. “A Bone Remodeling Model Governed by Cellular Micromechanics and Physiologically Based Pharmacokinetics.” *Journal of the Mechanical Behavior of Biomedical Materials* 104: 103657. https://doi.org/10.1016/j.jmbbm.2020.103657.

Beaupre, G S, and T E Orr. 1990. “An Approach for Time-Dependent Bone Modeling and Remodeling—Application: A Preliminary Remodeling Simulation - Beaupré - 2005 - Journal of Orthopaedic Research - Wiley Online Library.” *Journal of Orthopaedic …*, 662–70. http://onlinelibrary.wiley.com/doi/10.1002/jor.1100080507/abstract%5Cnpapers2://publication/uuid/9D5C378F-EDD8-4736-B052-510B4EFC85B9.

Belinha, J., R. M. Natal Jorge, and L. M.J.S. Dinis. 2012. “Bone Tissue Remodelling Analysis Considering a Radial Point Interpolator Meshless Method.” *Engineering Analysis with Boundary Elements* 36 (11): 1660–70. https://doi.org/10.1016/j.enganabound.2012.05.009.

Bhate, Dhruv, Clint A. Penick, Lara A. Ferry, and Christine Lee. 2019. “Classification and Selection of Cellular Materials in Mechanical Design: Engineering and Biomimetic Approaches.” *Designs* 3 (1): 1–31. https://doi.org/10.3390/designs3010019.

Braun, Jan-matthias, Poramate Manoonpong, and Xiaofeng Xiong. n.d. *BIOLOGY-INSPIRED ENGINEERING AND ENGINEERING-INSPIRED BIOLOGY*. https://doi.org/10.3389/978-2-

88966-340-8.

Buenzli, P. R., P. Pivonka, and D. W. Smith. 2011. “Spatio-Temporal Structure of Cell Distribution in Cortical Bone Multicellular Units: A Mathematical Model.” *Bone* 48 (4): 918–26. https://doi.org/10.1016/j.bone.2010.12.009.

Bullock, Whitney A., Frederick M. Pavalko, and Alexander G. Robling. 2019. “Osteocytes and Mechanical Loading: The Wnt Connection.” *Orthodontics and Craniofacial Research* 22 (S1): 175–79. https://doi.org/10.1111/ocr.12282.

Cerrolaza, M., F. Nieto, and Y. González. 2018. “Computation of the Dynamic Compression Effects in Spine Discs Using Integral Methods.” *Journal of Mechanics in Medicine and Biology* 18 (5): 1–16. https://doi.org/10.1142/S0219519417501032.

Cesar, R., R. S. Boffa, L. T. Fachine, T. P. Leivas, A. M.H. Silva, C. A.M. Pereira, R. B.M. Reiff, and J. M.D.A. Rollo. 2013. “Evaluation of Trabecular Microarchitecture of Normal Osteoporotic and Osteopenic Human Vertebrae.” *Procedia Engineering* 59: 6–15. https://doi.org/10.1016/j.proeng.2013.05.087.

Cha, Yong Han, Jun Il Yoo, Seok Young Hwang, Kap Jung Kim, Ha Yong Kim, Won Sik Choy, and Sun Chul Hwang. 2019. “Biomechanical Evaluation of Internal Fixation of Pauwels Type III Femoral Neck Fractures: A Systematic Review of Various Fixation Methods.” *CiOS Clinics in Orthopedic Surgery* 11 (1): 1–14. https://doi.org/10.4055/cios.2019.11.1.1.

Chen, Wenjiong, Xiaonan Zheng, and Shutian Liu. 2018. “Finite-Element-Mesh Based Method for Modeling and Optimization of Lattice Structures for Additive Manufacturing.” *Materials* 11 (11). https://doi.org/10.3390/ma11112073.

“Computer-Assisted Femoral Augmentation for Osteoporotic Hip Fracture Prevention.” 2013.

Corte, Alessandro Della, Ivan Giorgio, and Daria Scerrato. 2020. “A Review of Recent Developments in Mathematical Modeling of Bone Remodeling.” *Proceedings of the Institution of Mechanical Engineers, Part H: Journal of Engineering in Medicine* 234 (3): 273–81. https://doi.org/10.1177/0954411919857599.

Cowin, SC, and JJ Telega,. 2003. *Bone Mechanics Handbook, 2nd Edition. -. Applied Mechanics Reviews*. Vol. 56. https://doi.org/10.1115/1.1579463.

Cowin, S. C. 1986. “Wolff’s Law of Trabecular Architecture at Remodeling Equilibrium.” *Journal of Biomechanical Engineering* 108 (1): 83–88. https://doi.org/10.1115/1.3138584.

Daxner, Thomas. 2010. “Finite Element Modeling of Cellular Materials. In: Altenbach H., Öchsner A. (Eds) Cellular and Porous Materials in Structures and Processes. CISM International Centre for Mechanical Sciences, Vol 521. Springer, Vienna. Https://Doi.Org/10.1007/978-3-7091-0.” In , 634.

Eriksen, E. F., H. J.G. Gundersen, F. Melsen, and L. Mosekilde. 1984. “Reconstruction of the Formative Site in Iliac Trabecular Bone in 20 Normal Individuals Employing a Kinetic Model for Matrix and Mineral Apposition.” *Metabolic Bone Disease and Related Research* 5 (5): 243–52. https://doi.org/10.1016/0221-8747(84)90066-3.

Feng, Xu, and Jay M. McDonald. 2011. “Disorders of Bone Remodeling.” *Annual Review of Pathology: Mechanisms of Disease* 6 (1): 121–45. https://doi.org/10.1146/annurev-pathol-011110-130203.

Fonseca-vel, Aldemar. 2009. “Implementaci ´ on Del Modelo de Remodelaci ´ on ´ Osea de Komarova Para El Estudio de La Sensibilidad Del Proceso de Remodelamiento ´ Oseo Ante Cambios En Factores Locales,” 107–32.

Gabriel García-Acosta, Fahir D. Castañeda, Diego A. Garzón-Alvarado, Kalenia Márquez-Flórez, Diego A. Quexada-Rodriguez, Armando Salgado, Marco A. Velasco. 2020. “Design for the Additive Manufacturing of Structural Elements with Cellular Materials Using Voronoi Diagrams and Delaunay Triangulations: Biological and Structural Applications.” *Unpublished Manuscript*, 33.

Ganghoffer, Jean François, and Ibrahim Goda. 2018. “Prediction of Size Effects in Bone Brittle and Plastic Collapse.” *Multiscale Biomechanics*, 345–88. https://doi.org/10.1016/B978-1-78548-208-3.50008-3.

Garzón-Alvarado, D. A., and D. Linero. 2012a. “Comparative Analysis of Numerical Integration

Schemes of Density Equation for a Computational Model of Bone Remodelling." *Computer Methods in Biomechanics and Biomedical Engineering* 15 (11): 1189–96. https://doi.org/10.1080/10255842.2011.585972.

———. 2012b. "Comparative Analysis of Numerical Integration Schemes of Density Equation for a Computational Model of Bone Remodelling." *Computer Methods in Biomechanics and Biomedical Engineering* 15 (11): 1189–96. https://doi.org/10.1080/10255842.2011.585972.

Gasser, Jürg Andreas, and Michaela Kneissel. 2017. *Bone Toxicology*. *Bone Toxicology*. https://doi.org/10.1007/978-3-319-56192-9.

Geris, L., J. Vander Sloten, and H. Van Oosterwyck. 2010. "Connecting Biology and Mechanics in Fracture Healing: An Integrated Mathematical Modeling Framework for the Study of Nonunions." *Biomechanics and Modeling in Mechanobiology* 9 (6): 713–24. https://doi.org/10.1007/s10237-010-0208-8.

González, Y., M. Cerrolaza, and C. González. 2009. "Poroelastic Analysis of Bone Tissue Differentiation by Using the Boundary Element Method." *Engineering Analysis with Boundary Elements* 33 (5): 731–40. https://doi.org/10.1016/j.enganabound.2008.09.008.

Guevara, J. M., M. A. Moncayo, J. J. Vaca-González, M. L. Gutiérrez, L. A. Barrera, and D. A. Garzón-Alvarado. 2015. "Growth Plate Stress Distribution Implications during Bone Development: A Simple Framework Computational Approach." *Computer Methods and Programs in Biomedicine* 118 (1): 59–68. https://doi.org/10.1016/j.cmpb.2014.10.007.

Hambli, Ridha. 2014. "Connecting Mechanics and Bone Cell Activities in the Bone Remodeling Process: An Integrated Finite Element Modeling." *Frontiers in Bioengineering and Biotechnology* 2 (APR): 1–12. https://doi.org/10.3389/fbioe.2014.00006.

Hambli, Ridha, Mohamed Hafedh Boughattas, Jean Luc Daniel, and Azeddine Kourta. 2016. "Prediction of Denosumab Effects on Bone Remodeling: A Combined Pharmacokinetics and Finite Element Modeling." *Journal of the Mechanical Behavior of Biomedical Materials* 60 (January 2016): 492–504. https://doi.org/10.1016/j.jmbbm.2016.03.010.

Hopkins, R. B., N. Burke, C. Von Keyserlingk, W. D. Leslie, S. N. Morin, J. D. Adachi, A. Papaioannou,

et al. 2016. “The Current Economic Burden of Illness of Osteoporosis in Canada.” *Osteoporosis International* 27 (10): 3023–32. https://doi.org/10.1007/s00198-016-3631-6.

Jerez, S., and B. Chen. 2015. “Stability Analysis of a Komarova Type Model for the Interactions of Osteoblast and Osteoclast Cells during Bone Remodeling.” *Mathematical Biosciences* 264 (1): 29–37. https://doi.org/10.1016/j.mbs.2015.03.003.

Kenkre, J. S., and J. H.D. Bassett. 2018. *The Bone Remodelling Cycle*. *Annals of Clinical Biochemistry*. Vol. 55. https://doi.org/10.1177/0004563218759371.

Key, Radiolology. 2020. “Bone Mineral Density and Quantitative Imaging.” 12 de Junio. 2020. https://radiologykey.com/bone-mineral-density-and-quantitative-imaging/.

KOCH, JOHN C. 1993. “THE LAWS OF BONE ARCHITECTURE.” *From the Department of Anatomy, Johns Hopkins Medical School, Baltimore, Md.* 2 (6): 444–54.

Komarova, Svetlana V., Robert J. Smith, S. Jeffrey Dixon, Stephen M. Sims, and Lindi M. Wahl. 2003. “Mathematical Model Predicts a Critical Role for Osteoclast Autocrine Regulation in the Control of Bone Remodeling.” *Bone* 33 (2): 206–15. https://doi.org/10.1016/S8756-3282(03)00157-1.

Kumar, Natarajan Chennimalai, Iwona Jasiuk, and Jonathan Dantzig. 2011. “Dissipation Energy as a Stimulus for Cortical Bone Adaptation.” *Journal of Mechanics of Materials and Structures* 6 (1–4): 303–19. https://doi.org/10.2140/jomms.2011.6.303.

Lemaire, Vincent, Frank L. Tobin, Larry D. Greller, Carolyn R. Cho, and Larry J. Suva. 2004. “Modeling the Interactions between Osteoblast and Osteoclast Activities in Bone Remodeling.” *Journal of Theoretical Biology* 229 (3): 293–309. https://doi.org/10.1016/j.jtbi.2004.03.023.

Lenthe, G. Harry van, and Ralph Müller. 2006. “Prediction of Failure Load Using Micro-Finite Element Analysis Models: Toward in Vivo Strength Assessment.” *Drug Discovery Today: Technologies* 3 (2): 221–29. https://doi.org/10.1016/j.ddtec.2006.06.001.

Li, Jianying, Haiyan Li, Li Shi, Alex S.L. Fok, Cemal Ucer, Hugh Devlin, Keith Horner, and Nick Silikas.

2007. “A Mathematical Model for Simulating the Bone Remodeling Process under Mechanical Stimulus.” *Dental Materials* 23 (9): 1073–78. https://doi.org/10.1016/j.dental.2006.10.004.

Li, Xiaofeng, Yazhou Zhang, Heeseog Kang, Wenzhong Liu, Peng Liu, Jianghong Zhang, Stephen E. Harris, and Dianqing Wu. 2005. “Sclerostin Binds to LRP5/6 and Antagonizes Canonical Wnt Signaling.” *Journal of Biological Chemistry* 280 (20): 19883–87. https://doi.org/10.1074/jbc.M413274200.

Luxner, Mathias H., Alexander Woesz, Juergen Stampfl, Peter Fratzl, and Heinz E. Pettermann. 2009. “A Finite Element Study on the Effects of Disorder in Cellular Structures.” *Acta Biomaterialia* 5 (1): 381–90. https://doi.org/10.1016/j.actbio.2008.07.025.

Makris, Panagiotis A., Christopher G. Provatidis, and Demetrios A. Rellakis. 2006. “Discrete Variable Optimization of Frames Using a Strain Energy Criterion.” *Structural and Multidisciplinary Optimization* 31 (5): 410–17. https://doi.org/10.1007/s00158-005-0588-z.

Marco, Miguel, Eugenio Giner, José Ramón Caeiro-Rey, M. Henar Miguélez, and Ricardo Larraínzar-Garijo. 2019. “Numerical Modelling of Hip Fracture Patterns in Human Femur.” *Computer Methods and Programs in Biomedicine* 173: 67–75. https://doi.org/10.1016/j.cmpb.2019.03.010.

Martín, Raúl Álvarez San, and José Antonio Velutini Kochen. 2011. “Anatomía de La Cabeza Femoral Humana: Consideraciones En Ortopedia, Parte II. Biomecánica y Morfología Microscópica.” *International Journal of Morphology* 29 (2): 371–76.

Martínez, G., and M. Cerrolaza. 2006. “A Bone Adaptation Integrated Approach Using BEM.” *Engineering Analysis with Boundary Elements* 30 (2): 107–15. https://doi.org/10.1016/j.enganabound.2005.08.010.

Maxwell, Clerk. n.d. “Prof . Maxwell on Reciprocal Figures XLV . On Reciprocal Figures and Diagrams of Forces . JBy J . CLERK MAXWELL , F . R . S ., Professor of Natural Philosophy in King ’ s College , London ~ . and Diagrams of Forces . On Reciprocal Plane Figures . Definiti” xxv: 250–61.

Metcalf, Louis M., Enrico Dall'Ara, Margaret A. Paggiosi, John R. Rochester, Nicolas Vilayphiou, Graham J. Kemp, and Eugene V. McCloskey. 2018. "Validation of Calcaneus Trabecular Microstructure Measurements by HR-PQCT." *Bone* 106: 69–77. https://doi.org/10.1016/j.bone.2017.09.013.

Meyer, G. H. 1867. "'Die Architektur Der Spongiosa,' Archiv Fur Anatomie, Physiologie Und Wissenschaftliche Medizin, Reichert Und DuBois-Reymonds Archiv."

Nackenhorst, Udo. 1997. "Numerical Simulation of Stress Stimulated Bone Remodeling." *Technische Mechanik* 17 (1): 31–40. http://www.uni-magdeburg.de/ifme/zeitschrift_tm/1997_Heft1/Nackenhorst.pdf.

Niu, Tianhua, and Clifford J. Rosen. 2005. "The Insulin-like Growth Factor-I Gene and Osteoporosis: A Critical Appraisal." *Gene* 361 (1–2): 38–56. https://doi.org/10.1016/j.gene.2005.07.016.

Okaji, Masayo, Hideaki Sakai, Eiko Sakai, Mitsue Shibata, Fumio Hashimoto, Yasuhiro Kobayashi, Noriaki Yoshida, Kuniaki Okamoto, Kenji Yamamoto, and Yuzo Kato. 2003. "The Regulation of Bone Resorption in Tooth Formation and Eruption Processes in Mouse Alveolar Crest Devoid of Cathepsin K." *Journal Pharmacological Sciences* 91 (4): 285–94. https://doi.org/10.1254/jphs.91.285.

Owen, Robert, and Gwendolen C. Reilly. 2018. "In Vitro Models of Bone Remodelling and Associated Disorders." *Frontiers in Bioengineering and Biotechnology* 6 (OCT): 1–22. https://doi.org/10.3389/fbioe.2018.00134.

Parfitt, A. M. 1994. "Osteonal and Hemi-osteonal Remodeling: The Spatial and Temporal Framework for Signal Traffic in Adult Human Bone." *Journal of Cellular Biochemistry* 55 (3): 273–86. https://doi.org/10.1002/jcb.240550303.

Peng, Matthew Jian Qiao, Hong Wen Xu, Hai Yan Chen, Ze Lin, Xin Xu Li, Chu Long Shen, Yong Qiang Lau, Er Xing He, and Yue Ming Guo. 2020. "Biomechanical Analysis for Five Fixation Techniques of Pauwels-III Fracture by Finite Element Modeling." *Computer Methods and Programs in Biomedicine* 193: 105491. https://doi.org/10.1016/j.cmpb.2020.105491.

Peyroteo, M. M.A., J. Belinha, S. Vinga, L. M.J.S. Dinis, and R. M. Natal Jorge. 2019. "Mechanical Bone Remodelling: Comparative Study of Distinct Numerical Approaches." *Engineering Analysis with Boundary Elements* 100 (January 2018): 125–39. https://doi.org/10.1016/j.enganabound.2018.01.011.

Pivonka, Peter, Jan Zimak, David W. Smith, Bruce S. Gardiner, Colin R. Dunstan, Natalie A. Sims, T. John Martin, and Gregory R. Mundy. 2008. "Model Structure and Control of Bone Remodeling: A Theoretical Study." *Bone* 43 (2): 249–63. https://doi.org/10.1016/j.bone.2008.03.025.

Raggatt, Liza J., and Nicola C. Partridge. 2010. "Cellular and Molecular Mechanisms of Bone Remodeling." *Journal of Biological Chemistry* 285 (33): 25103–8. https://doi.org/10.1074/jbc.R109.041087.

Rapisarda, Alessio Ciro, Alessandro Della Corte, Rafał Drobnicki, Fabio Di Cosmo, and Luigi Rosa. 2019. "A Model for Bone Mechanics and Remodeling Including Cell Populations Dynamics." *Zeitschrift Fur Angewandte Mathematik Und Physik* 70 (1): 1–17. https://doi.org/10.1007/s00033-018-1055-1.

Ruff1. Ruffoni, D. & Van Lenthe, G. H. 3.10 Finite element analysis in bone research: A computational method relating structure to mechanical function. Comprehensive Biomaterials II vol. 3 (Elsevier Ltd., 2017).oni, D., and G. H. Van Lenthe. 2017. *3.10 Finite Element Analysis in Bone Research: A Computational Method Relating Structure to Mechanical Function*. *Comprehensive Biomaterials II*. Vol. 3. Elsevier Ltd. https://doi.org/10.1016/B978-0-12-803581-8.09798-8.

Schaedler, Tobias A., and William B. Carter. 2016. "Architected Cellular Materials." *Annual Review of Materials Research* 46 (April): 187–210. https://doi.org/10.1146/annurev-matsci-070115-031624.

Seeman, Ego. 2003. "The Structural and Biomechanical Basis of the Gain and Loss of Bone Strength in Women and Men." *Endocrinology and Metabolism Clinics of North America* 32 (1): 25–38. https://doi.org/10.1016/S0889-8529(02)00078-6.

Sozen, Tumay, Lale Ozisik, and Nursel Calik Basaran. 2017. “An Overview and Management of Osteoporosis.” *European Journal of Rheumatology* 4 (1): 46–56. https://doi.org/10.5152/eurjrheum.2016.048.

Stein, Emily M., Barbara C. Silva, Stephanie Boutroy, Bin Zhou, Ji Wang, Julia Udesky, Chiyuan Zhang, et al. 2013. “Primary Hyperparathyroidism Is Associated with Abnormal Cortical and Trabecular Microstructure and Reduced Bone Stiffness in Postmenopausal Women.” *Journal of Bone and Mineral Research* 28 (5): 1029–40. https://doi.org/10.1002/jbmr.1841.

Ström, O., F. Borgström, John A. Kanis, Juliet Compston, Cyrus Cooper, Eugene V. McCloskey, and Bengt Jönsson. 2011. “Osteoporosis: Burden, Health Care Provision and Opportunities in the EU.” *Archives of Osteoporosis* 6 (1–2): 59–155. https://doi.org/10.1007/s11657-011-0060-1.

Sun, Xiaoqiang, Yunqing Kang, Jiguang Bao, Yuanyuan Zhang, Yunzhi Yang, and Xiaobo Zhou. 2013. “Modeling Vascularized Bone Regeneration within a Porous Biodegradable CaP Scaffold Loaded with Growth Factors.” *Biomaterials* 34 (21): 4971–81. https://doi.org/10.1016/j.biomaterials.2013.03.015.

Swarthout, John T., Richard C. D’Alonzo, Nagarajan Selvamurugan, and Nicola C. Partridge. 2002. “Parathyroid Hormone-Dependent Signaling Pathways Regulating Genes in Bone Cells.” *Gene* 282 (1–2): 1–17. https://doi.org/10.1016/S0378-1119(01)00798-3.

Valdez, S. Ivvan, Salvador Botello, Miguel A. Ochoa, José L. Marroquín, and Victor Cardoso. 2017. “Topology Optimization Benchmarks in 2D: Results for Minimum Compliance and Minimum Volume in Planar Stress Problems.” *Archives of Computational Methods in Engineering* 24 (4): 803–39. https://doi.org/10.1007/s11831-016-9190-3.

Vanegas-Acosta, J. C., N. S. Landinez P., D. A. Garzón-Alvarado, and M. C. Casale R. 2011. “A Finite Element Method Approach for the Mechanobiological Modeling of the Osseointegration of a Dental Implant.” *Computer Methods and Programs in Biomedicine* 101 (3): 297–314. https://doi.org/10.1016/j.cmpb.2010.11.007.

Walton, Dan, and Hadi Moztarzadeh. 2017. “Design and Development of an Additive Manufactured Component by Topology Optimisation.” *Procedia CIRP* 60: 205–10.

https://doi.org/10.1016/j.procir.2017.03.027.

Weinans, H., R. Huiskes, and H. J. Grootenboer. 1992. “The Behavior of Adaptive Bone-Remodeling Simulation Models.” *Journal of Biomechanics* 25 (12): 1425–41. https://doi.org/10.1016/0021-9290(92)90056-7.

Wippert, Pia Maria, Michael Rector, Gisela Kuhn, and Karin Wuertz-Kozak. 2017. “Stress and Alterations in Bones: An Interdisciplinary Perspective.” *Frontiers in Endocrinology* 8 (MAY): 1–7. https://doi.org/10.3389/fendo.2017.00096.

Wu, Jun, Weiming Wang, and Xifeng Gao. 2019. “Design and Optimization of Conforming Lattice Structures.” *IEEE Transactions on Visualization and Computer Graphics*, 1–1. https://doi.org/10.1109/tvcg.2019.2938946.

Yamamoto, Yoko, Tatsuya Yoshizawa, Toru Fukuda, Yuko Shirode-Fukuda, Taiyong Yu, Keisuke Sekine, Takashi Sato, et al. 2013. “Vitamin D Receptor in Osteoblasts Is a Negative Regulator of Bone Mass Control.” *Endocrinology* 154 (3): 1008–20. https://doi.org/10.1210/en.2012-1542.

7. ANNEXES

Strain energy

$$W_{density} = 0.5 \cdot \underline{\sigma} \cdot \underline{\epsilon^T} = 0.5 \frac{\sigma_{xx}^2}{E}$$

$$U_{strain} = \iiint W_{density}\, dx\, dy\, dz = \int \int W_{density}\, dA dx = \frac{1}{2E} \int_A^{\cdot} \int_0^L \left(\left(\frac{P_i}{A} \right)^2 + \left(\frac{M_{(x)} z}{I} \right)^2 \right) dx\, dA$$

Fig. 52: Neutral axis in discrete element.

$$= \frac{1}{2E} \int_0^L \int_A^{\cdot} \left(\left(\frac{P_i}{A} \right)^2 + \left(\frac{M_{(x)} z}{I} \right)^2 \right) dA dx$$

$$\frac{1}{2E} \int_0^L \frac{P^2}{A} dx + \frac{1}{2E} \int_0^L \frac{M_x}{I^2} ds \int_A^{\cdot} z^2 dA$$

$$= \frac{1}{2} \int_0^L \frac{{P_i}^2}{EA} dx + \frac{1}{2} \int_0^L \frac{M^2(x)}{EI} dx$$

Solving the integral of the energy term due to the function moment M(x):

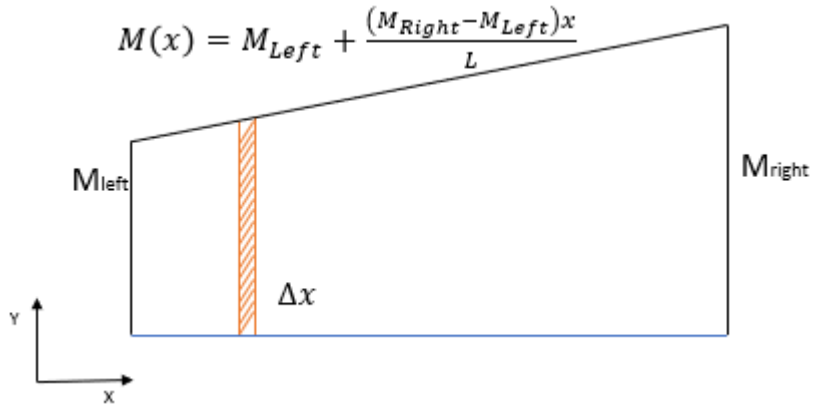

Fig. 53:Moment function along the element.

$$\int_0^L \left(M_L + \frac{M_R - M_L}{L} x \right)^2 dx = {M_L}^2 x + M_L \left(\frac{M_R - M_L}{L} \right) x^2 + \frac{1}{3} \left(\frac{M_R - M_L}{L} x \right)^2 x^3$$

$$= {M_L}^2 x + M_L \left(\frac{M_R - M_L}{L} \right) x^2 + \frac{1}{3} \left(\frac{M_R - M_L}{L} x \right)^2 x^3 \Bigg]_{x=0}^{x=L}$$

$$= {M_L}^2 L + \frac{M_R M_L}{L} L^2 - \frac{{M_L}^2}{L} L^2 + \frac{1}{3}\left(\frac{{M_R}^2 - 2M_R M_L + {M_L}^2}{L^2} L^3\right)^2$$

$$= \frac{{M_L}^2 + {M_R}^2 + M_L \cdot M_R}{3EI} \cdot L$$

So the total energy strain for each element is:

$$U_{strain} = \frac{1}{2}\sum_{i=1}^{N}\left[\frac{{P_i}^2 L_i}{E_i A} + \frac{1}{3}\cdot\frac{(M_i^{left})^2 + (M_i^{right})^2 + M_i^{left}\cdot M_i^{right}}{E_i I}\cdot L_i\right] \text{ (frame element)}$$

$$U_{strain} = \frac{1}{2}\sum_{i=1}^{N}\left[\frac{{P_i}^2 L_i}{E_i A}\right] \text{ (truss element)}$$

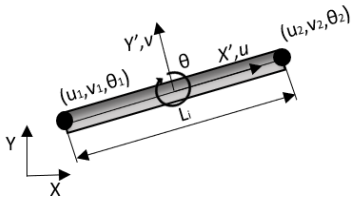

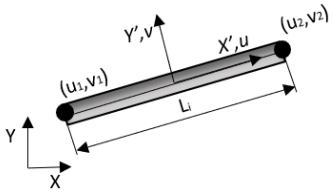

Fig. 54: Element formulation 2D, frame (left) and truss (right).

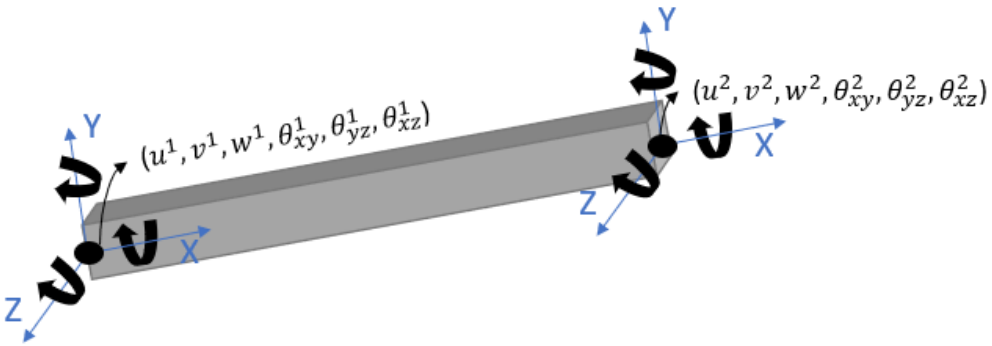

Fig. 55: Element formulation 3D

Finite element, direct formulation Beam elements.

For a beam element the stiffness matrix is:

$$[K]_{Local} = \begin{bmatrix} \frac{12EI}{L^3} & \frac{6EI}{L^2} & \frac{-12EI}{L^3} & \frac{6EI}{L^2} \\ \frac{6EI}{L^2} & \frac{4EI}{L} & \frac{-6EI}{L^2} & \frac{2EI}{L} \\ \frac{-12EI}{L^3} & \frac{-6EI}{L^2} & \frac{12EI}{L^3} & \frac{-6EI}{L^2} \\ \frac{6EI}{L^2} & \frac{2EI}{L} & \frac{-6EI}{L^2} & \frac{4EI}{L} \end{bmatrix}$$

This local system can be seen in global form using the rotation matrix as follows:

$[K]_{global}$= $[T]^t[K]_{local}[T]$

where

$$[T] = \begin{pmatrix} \cos(\theta) & \sin(\theta) \\ -\sin(\theta) & \cos(\theta) \end{pmatrix}$$

The global system of equations is given by:

$$[F] = [K]_{global}[u] \quad \text{Eq. 3}$$

Finite element, direct formulation truss elements.

For a truss element the stiffness matrix is:

$$[K]_{Local} = \begin{pmatrix} \frac{EA}{L} & \frac{-EA}{L} \\ \frac{-EA}{L} & \frac{EA}{L} \end{pmatrix}$$

Finite element, direct formulation Frame elements.

The stiffness matrix can be obtained by superposition of the truss and beam elements, resulting in the following:

$$[K]_{Local} = \begin{bmatrix} \frac{AE}{L} & 0 & 0 & \frac{-AE}{L} & 0 & 0 \\ 0 & \frac{12EI}{L^3} & \frac{6EI}{L^2} & 0 & \frac{-12EI}{L^3} & \frac{6EI}{L^2} \\ 0 & \frac{6EI}{L^2} & \frac{4EI}{L} & 0 & \frac{-6EI}{L^2} & \frac{2EI}{L} \\ \frac{-AE}{L} & 0 & 0 & \frac{AE}{L} & 0 & 0 \\ 0 & \frac{-12EI}{L^3} & \frac{-6EI}{L^2} & 0 & \frac{12EI}{L^3} & \frac{-6EI}{L^2} \\ 0 & \frac{6EI}{L^2} & \frac{2EI}{L} & 0 & \frac{-6EI}{L^2} & \frac{4EI}{L} \end{bmatrix}$$

For a formulation using local coordinates as seen in Fig. 54, the following transformation can be used:

$[K]_{global} = [T]^t[K]_{local}[T]$

Where

$$[T] = \begin{bmatrix} \cos(\theta) & \sin(\theta) & 0 & 0 & 0 & 0 \\ -\sin(\theta) & \cos(\theta) & 0 & 0 & 0 & 0 \\ 0 & 0 & 1 & 0 & 0 & 0 \\ 0 & 0 & 0 & \cos(\theta) & \sin(\theta) & 0 \\ 0 & 0 & 0 & -\sin(\theta) & \cos(\theta) & 0 \\ 0 & 0 & 0 & 0 & 0 & 1 \end{bmatrix}$$

Continuum Elements

An overview on how the finite element method (FEM) is used to solve the elasticity equations is shown in this section for the continuum elements, for triangular elements.

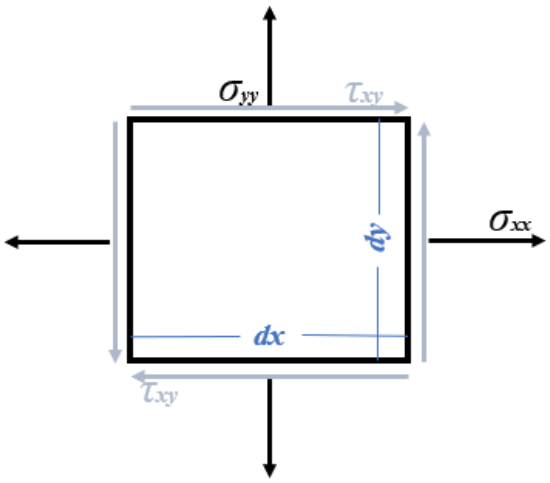

Fig. 56: Stress element.

Considering a differential stress element as seen in Fig. 56, the equilibrium equations are:

$$\sum F_x \rightarrow (\sigma_x)_{x+dx} t\, dy - (\sigma_x)_x t\, dy + (\tau_{xy})_{y+dy} t\, dx - (\tau_{xy})_y t\, dx + X t dx dy = 0$$

$$\sum F_y \rightarrow (\sigma_y)_{y+dy} t\, dx - (\sigma_y)_y t\, dx + (\tau_{xy})_{x+dx} t\, dy - (\tau_{xy})_x t\, dy + Y t dx dy = 0$$

Which yields the following differential equations:

$$\frac{\partial \sigma_x}{\partial x} + \frac{\partial \sigma_y}{\partial y} + X = 0$$

$$\frac{\partial \sigma_y}{\partial y} + \frac{\partial \tau_{xy}}{\partial y} + Y = 0$$

The information provided by the boundary conditions is included as the following equilibrium equations, according to Fig. 57:

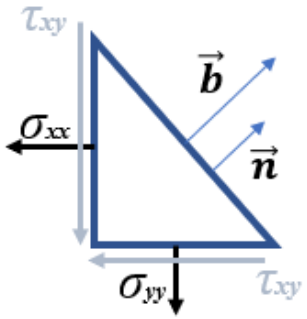

Fig. 57: Boundary element.

$$\sigma_x n_x + \tau_{xy} n_y - b_x = 0$$

$$\tau_{xy} n_x + \sigma_y n_y - b_y = 0$$

Plane strain

$$[D] = \frac{E}{(1-2\nu)(1+\nu)} \begin{bmatrix} 1-\nu & \nu & 0 \\ \nu & 1-\nu & 0 \\ 0 & 0 & \frac{1}{2}-\nu \end{bmatrix}$$

Plane stress

$$[D] = \frac{E}{(1-\nu^2)} \begin{bmatrix} 1 & \nu & 0 \\ \nu & 1 & 0 \\ 0 & 0 & \frac{1-\nu}{2} \end{bmatrix}$$

Postprocessing:

$$[\sigma] = [D]\,[\varepsilon]$$

$$[\sigma] = [D]\,L\,[U]$$

Where *L* is a differential operator:

Rearranging the following system of PDEs can be obtained.

$$D_{11}\frac{\partial^2 u}{\partial x^2} + D_{12}\frac{\partial^2 v}{\partial x \partial y} + D_{33}\frac{\partial^2 u}{\partial y^2} + D_{33}\frac{\partial^2 v}{\partial x \partial y} + \bar{x} = 0$$

$$D_{21}\frac{\partial^2 u}{\partial x \partial y} + D_{22}\frac{\partial^2 v}{\partial y^2} + D_{33}\frac{\partial^2 u}{\partial x \partial y} + D_{33}\frac{\partial^2 v}{\partial x^2} + \bar{y} = 0$$

The finite element formulation will start using the Galerkin method to obtain a weak form of this system of equations. This process will be shown for equation for the first equation of the two.

$$\int_{\Omega} W\left(D_{11}\frac{\partial^2 u}{\partial\, x^2}+D_{33}\frac{\partial^2 u}{\partial\, y^2}\right)d\Omega+\int_{\Omega} W\left(D_{12}\frac{\partial^2 u}{\partial\, x\partial y}+D_{33}\frac{\partial^2 u}{\partial\, x\partial y}\right)d\Omega+\int_{\Omega} W\bar{x}d\Omega=0$$

The weak form can be obtained by applying integration by parts (divergence theorem) as follows:

$$\int_{\Omega}\left(D_{11}\frac{\partial W}{\partial x}\frac{\partial \hat{u}}{\partial x}+D_{33}\frac{\partial W}{\partial y}\frac{\partial \hat{u}}{\partial y}\right)d\Omega+\int_{\Omega}\left(D_{12}\frac{\partial W}{\partial x}\frac{\partial \hat{v}}{\partial y}+D_{33}\frac{\partial W}{\partial y}\frac{\partial \hat{v}}{\partial x}\right)d\Omega$$

$$-\int_{\Gamma} W\left(D_{11}\frac{\partial \hat{u}}{\partial x}n_x+D_{33}\frac{\partial \hat{u}}{\partial y}n_y\right)d\Gamma-\int_{\Gamma} W\left(D_{12}\frac{\partial \hat{v}}{\partial y}n_x+D_{33}\frac{\partial \hat{v}}{\partial x}n_y\right)d\Gamma-\int_{\Omega} W\bar{x}d\Omega=0$$

Is noted that the boundary conditions are added after applying integration by parts. Also, is useful to note that these terms can be expressed as:

$$\int_{\Gamma} W\left(D_{11}\frac{\partial \hat{u}}{\partial x}n_x+D_{33}\frac{\partial \hat{u}}{\partial y}n_y\right)d\Gamma+\int_{\Gamma} W\left(D_{12}\frac{\partial \hat{v}}{\partial y}n_x+D_{33}\frac{\partial \hat{v}}{\partial x}n_y\right)d\Gamma$$

$$=\int_{\Gamma} W\left(\sigma_x n_x+\tau_{xy}n_y\right)d\Gamma=\int_{\Gamma} W f_x d\Gamma$$

Using this expression, the weak formulation yields:

$$\int_{\Omega}\left(D_{11}\frac{\partial W}{\partial x}\frac{\partial \hat{u}}{\partial x}+D_{12}\frac{\partial W}{\partial x}\frac{\partial \hat{v}}{\partial y}\right)d\Omega+\int_{\Omega}\left(D_{33}\frac{\partial W}{\partial y}\frac{\partial \hat{v}}{\partial y}+D_{33}\frac{\partial W}{\partial y}\frac{\partial \hat{v}}{\partial x}\right)d\Omega=\int_{\Omega} W\bar{x}d\Omega+\int_{\Gamma} W f_x d\Gamma$$

Analogously the weak form of equation 11 is:

$$\int_{\Omega}\left(D_{33}\frac{\partial W}{\partial x}\frac{\partial \hat{u}}{\partial x}+D_{33}\frac{\partial W}{\partial x}\frac{\partial \hat{v}}{\partial y}\right)d\Omega+\int_{\Omega}\left(D_{21}\frac{\partial W}{\partial y}\frac{\partial \hat{v}}{\partial y}+D_{22}\frac{\partial W}{\partial y}\frac{\partial \hat{v}}{\partial x}\right)d\Omega=\int_{\Omega} W\bar{y}d\Omega+\int_{\Gamma} W f_y d\Gamma$$

By using Voight notation this can be expressed as:

$$\int_{\Omega}(L(W)^T[D]L[U])d\Omega=\int_{\Omega} W\bar{X}d\Omega+\int_{\Gamma} WFd\Gamma$$

Where:

$$[W]=\begin{bmatrix}W & 0\\ 0 & W\end{bmatrix}\quad [U]=\begin{bmatrix}u\\ v\end{bmatrix}\quad [X]=\begin{bmatrix}x\\ y\end{bmatrix}\quad [F]=\begin{bmatrix}F_x\\ F_y\end{bmatrix}$$

$$\hat{u}^e(x)=\sum_{m=1}^{M} u_m N_m(x)$$

The next step is to discretize the domain so an approximation in an element will be:

$$t\int_{\Omega^e}(L(W)^T[D]L[U])d\Omega^e = \int_{\Omega^e} W\bar{X}d\Omega^e + \mathrm{t}\int_{\Gamma^e} WFd\Gamma^e \qquad \text{Eq. 30}$$

In this form we can appreciate the problem in a simplified way as:

$[K^e][U_m] = [F^e]$

Where each term corresponds to those in Eq. 30.

Given that the domain discretization gives place to irregular elements, a mapping of the domain is performed in each element that will facilitate numerical integration, in this case gaussian integration as seen Fig. 58.

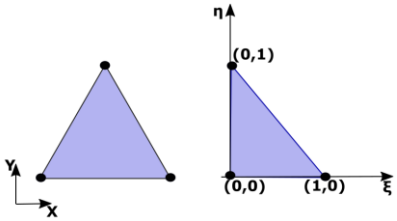

Fig. 58: Mapping to perform gaussian integration.

Using a local coordinate system (ξ,η) the elemental formulation yields:

$$L(\,) = \begin{bmatrix} \frac{\partial(\,)}{\partial x} & 0 \\ 0 & \frac{\partial(\,)}{\partial x} \\ \frac{\partial(\,)}{\partial x} & \frac{\partial(\,)}{\partial x} \end{bmatrix} = \frac{1}{|J|}\begin{bmatrix} \frac{\partial y}{\partial \eta}\frac{\partial(\,)}{\partial \xi} - \frac{\partial y}{\partial \xi}\frac{\partial(\,)}{\partial \eta} & 0 \\ 0 & \frac{\partial x}{\partial \xi}\frac{\partial(\,)}{\partial \eta} - \frac{\partial y}{\partial \eta}\frac{\partial(\,)}{\partial \xi} \\ \frac{\partial x}{\partial \xi}\frac{\partial(\,)}{\partial \eta} - \frac{\partial y}{\partial \eta}\frac{\partial(\,)}{\partial \xi} & \frac{\partial y}{\partial \eta}\frac{\partial(\,)}{\partial \xi} - \frac{\partial y}{\partial \xi}\frac{\partial(\,)}{\partial \eta} \end{bmatrix} = \frac{1}{|J|}L^*(\,)$$

And the shape functions for a triangular linear node are:

$$N_i = \xi, N_j = \eta,\ N_k = 1 - \xi - \eta$$

These shape functions will be used approximate the displacement at each node, and the stiffness term $[K_{lm}]$ will be:

$$[K_{lm}] = \frac{t}{|J|}(L^*[W])^T[D](\,L^*[N_m])\int_{\Omega} d\xi \mathrm{d}\,\eta$$

The load vector can finally be expressed as the sum of both body and surface forces as:

$[F_l] = \int_{\Omega^e} W\bar{X}d\Omega^e + \mathrm{t}\int_{\Gamma^e} WFd\Gamma^e$

Density equation

The energy density is:

$$W(\rho) = \frac{1}{2\rho}\lambda^n \varepsilon^T C_0 \varepsilon = \frac{\lambda^n}{\rho}\left[\frac{\varepsilon^T C_0 \varepsilon}{2}\right] = \frac{\lambda^n}{\rho} U$$

The evolution density equation as stated by (Nackenhorst 1997) is:

$$\frac{d\rho}{dt} = k\left[\frac{W_\rho}{W_{ref}} - 1\right]$$ **Error! Reference source not found.**

Because $\lambda = \frac{\rho}{\rho_0}$ we can rearrange Eq. 1into:

$$\frac{d\lambda}{dt} = K\rho_0\left[\frac{\rho_0}{\rho_0}\frac{\lambda^n U}{\rho W_{ref}} - 1\right] = K\rho_0\left[\left[\frac{\rho_0}{\rho}\right]\frac{\lambda^n U}{\rho_0 W_{ref}} - 1\right] = K\rho_0\left[\lambda^{n-1}\frac{U}{\rho_0 W_{ref}} - 1\right]$$

And making:

$k_1 = K\rho_0$ and $\rho_0 W_{ref} = U_{ref}$

The dimensionless form of the evolution density equation can be written as:

$$\frac{d\lambda}{dt} = k_1\left[\lambda^{n-1}\frac{U}{U_{ref}} - 1\right]$$

Additional benchmark test for the bone remodelling algorithm

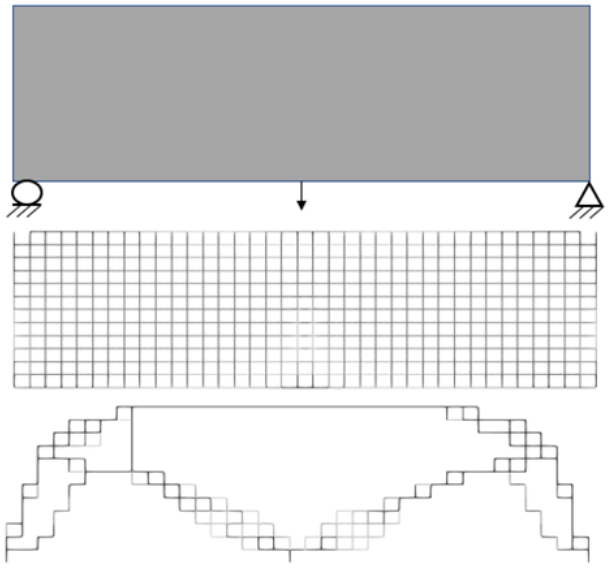

Fig. 59: Topology result in Messerschmitt-Bolkow-Blohm (Mbb) beam, after the bone remodelling algorithm.

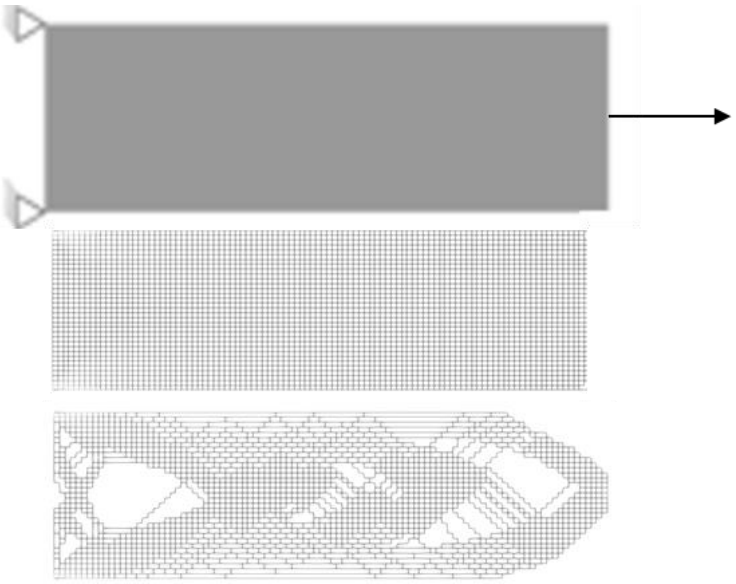

Fig. 60: Optimization for beam in tension

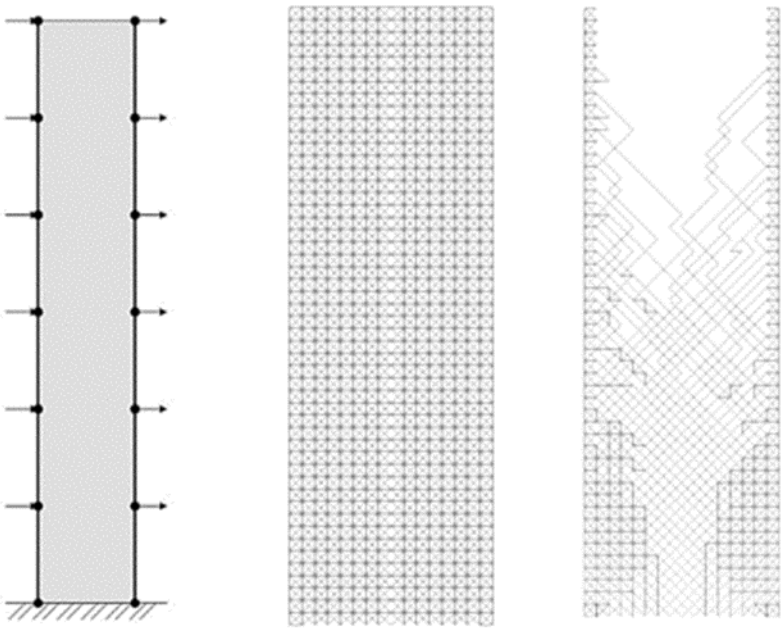

Fig. 61: Optimization for a vertical beam with distributed load.